TECHNISCHE UNIVERSITÄT WIEN

INSTITUT FÜR PHOTONIK
Photonics Institute

Dissertation

Generation and Amplification of Ultrashort-Pulse Bursts

zur Erlangung des akademischen Grades

Doktor der technischen Wissenschaften

eingereicht von

Vinzenz Stummer
Matrikelnummer 01125138

ausgeführt am Institut für Photonik
der Fakultät für Elektrotechnik und Informationstechnik der Technischen Universität Wien

Betreuer: Univ. Prof. PhD Andrius Baltuška

Wien, 11.10.2023

Abstract

Ultrashort laser pulses are characterized by their outstanding combination of properties, including extremely high intensity, femtosecond temporal resolutions, and wide bandwidths, often spanning more than an octave. Exploring the largest, up to terahertz, repetition rates between pulses requires innovation in shaping and control of pulse formats because of limitations in average power. Burst-mode laser systems have been developed as a promising way to enable increased repetition rates while maintaining high pulse energies within bursts of closely spaced equidistant pulses. This thesis is devoted to exploring the landscape of applications for which terahertz-repetition-rate bursts of ultrashort pulses can contribute in novel ways and develop further ultrashort-pulse burst technology in the prospect of these applications. Not only scientific areas, such as molecular orientation, terahertz radiation generation, or the modulation and amplification of electron bunches but also highly industrial subjects, such as micromachining and spectroscopy, are identified. In particular, Burst Stimulated Raman Spectroscopy is formulated as it was developed in our group recently, and the generation of terahertz generation with continuously tunable spectral linewidths from millijoule-amplified terahertz-repetition-rate near-infrared pulses is demonstrated experimentally.

Existing techniques for high repetition rate burst generation, including pulse splitting, recombination, spatial filtering, beam combining, or the use of birefringent crystals or Mach-Zehnder interferometers have limitations in terms of the number of pulses achievable due to energy throughput constraints. As a central focus of this thesis, new burst amplification methods combining temporal pulse shaping and nonlinear optical techniques based on the Vernier technique were developed. The Vernier concept relies on burst pulse buildup through a specific master-oscillator regenerative-amplifier combination, eliminating the need for pulse beam path splitting. In the course of the last 4 years of this doctoral work, the Vernier technique could be further developed regarding the amplification to high burst energies, and the phase stabilization and scalability of pulses. Depending on the number of pulses, two regimes can be identified: In a regime of low pulse number (low-N), it is possible by phase modulation before chirped pulse amplification to amplify terahertz-repetition-rate pulses to millijoule energies without the risk of amplifier damage. A regime of high pulse number (high-N) was discovered and examined in detail, both by a numerical model and experimentally by generation and characterization of bursts with up to 40 pulses. Nonlinear optical techniques, such as Sum Frequency Generation, Difference Frequency Generation and Self-Phase Modulation, are proven to be applicable in the terahertz-repetition-rate domain by buildup and burst-mode operation of a nonlinear parametric amplifier, where all pulses could be shown to be converted individually without interpulse cross-talk.

Reaching further, other technologies outside the burst domain are also considered: Burst-mode pulses are compared to frequency combs. Cavity-dumped sources are introduced, pushing further the limits of repetition rate that are given in the strongly related type of Q-switched sources, which are limited to several tens of kilohertz for pulse generation

with stable energies. The generation of pulse pairs is another interesting pulse format, with the time delay between the pulses being a specific attribute. A novel technique to set pre-determined time delays over an extraordinarily large dynamic range is concipated and experimentally demonstrated.

Kurzfassung

Ultrakurze Laserpulse zeichnen sich durch ihre herausragende Kombination von Eigenschaften aus, darunter extrem hohe Intensität, Femtosekunden-Zeitauflösung und hohe Bandbreiten, die oft mehr als eine Oktave umfassen. Die Erforschung der größten Wiederholungsraten zwischen den Pulsen, bis hin zu Terahertz, erfordert Innovationen bei der kontrollierten Erzeugung von Pulsformaten aufgrund von Einschränkungen bei der mittleren Leistung. Burst-Mode-Lasersysteme wurden als vielversprechender Ansatz entwickelt, um höhere Wiederholungsraten zu ermöglichen und gleichzeitig hohe Pulsenergien innerhalb von Bursts eng benachbarter, equidistanter Pulse aufrechtzuerhalten. Diese Dissertation widmet sich der Erkundung des Spektrums von Anwendungen, für welches Terahertz-Wiederholungsraten-Bursts von ultrakurzen Pulsen auf neuartige Weise beitragen können, und der Weiterentwicklung der Technologie von Bursts bestehend aus ultrakurzen Pulsen im Hinblick auf diese Anwendungen. Nicht nur wissenschaftliche Bereiche wie die kontrollierte Orientierung von Molekülen, Terahertz-Strahlungserzeugung oder Modulation und Verstärkung von Elektronenpaketen, sondern auch hochindustrielle Themen wie Materialbearbeitung und Spektroskopie werden identifiziert. Insbesondere wird die Burst-Stimulierte-Raman-Spektroskopie formuliert, so wie diese kürzlich in unserer Gruppe entwickelt wurde, und die Erzeugung von Terahertz-Strahlung mit kontinuierlich einstellbaren spektralen Linienbreiten erzeugt aus millijoule-verstärkten Bursts mit Nahinfrarotpulsen und Terahertz-Wiederholungsraten wird experimentell demonstriert.

Bestehende Techniken zur Erzeugung von Burst mit hoher Wiederholungsrate, einschließlich Pulsteilung und -rekombination, räumlicher Filterung, Strahlkombination sowie die Nutzung von doppelbrechenden Kristallen oder Mach-Zehnder-Interferometern, haben Einschränkungen hinsichtlich der erzielbaren Pulsanzahl aufgrund von Beschränkungen in der zu erreichenden Energie. Als zentraler Schwerpunkt dieser Arbeit wurden neue Burst-Verstärkungsmethoden entwickelt, die zeitliche Methoden zur Pulsformung und nichtlineare optische Techniken auf der Grundlage der Vernier-Technik kombinieren. Das Vernier-Konzept beruht auf dem Aufbau von Burst-Pulsen durch eine Kombination eines Master-Oszillators und eines regenerativen Verstärker, wodurch die Notwendigkeit der Pulsstrahlwegteilung entfällt. Im Verlauf der letzten 4 Jahre dieser Promotionsarbeit konnte die Vernier-Technik in Bezug auf die Verstärkung zu hohen Burst-Energien sowie auf die Phasenstabilisierung und Skalierbarkeit der Pulszahl weiterentwickelt werden. In diesem Zusammenhang lassen sich zwei Regime identifizieren: In einem Regime mit geringer Pulsanzahl (low-N) ist es durch Phasenmodulation vor der gechirpten Pulsverstärkung möglich, Bursts mit Terahertz-Wiederholungsraten auf Millijoule-Energien zu verstärken. Ein Regime mit hoher Pulsanzahl (high-N) wurde entdeckt und eingehend untersucht, sowohl durch ein numerisches Modell als auch experimentell durch Erzeugung und Charakterisierung von Bursts mit bis zu 40 Pulsen. Nichtlineare optische Techniken wie Summenfrequenzerzeugung, Differenzfrequenzerzeugung und Selbstphasenmodulation haben sich durch den Aufbau und den Burst-Modus-Betrieb eines nichtlinearen parametrischen Verstärkers als anwendbar im Terahertz-Wiederholungsraten-Bereich erwiesen. Dabei konnte gezeigt

werden, dass alle Pulse einzeln ohne Übersprechen zwischen den Pulsen umgewandelt werden.

Überdies werden andere Technologien außerhalb des Burst-Bereichs ebenfalls betrachtet: Im Burst-Modus erzeugte Pulse werden mit Frequenzkämmen verglichen. Kavitätsausgekoppelte (cavity-dumped) Quellen werden vorgestellt, die die Grenzen in Bezug auf die Wiederholungsrate weiter vorantreiben, die bei der stark verwandten Art von gütegeschalteten Quellen gegeben sind. Letztere sind auf mehrere zehntausend Hertz für die Pulsenerzeugung mit stabilen Energien begrenzt. Die Erzeugung von Pulspaaren ist ein weiteres interessantes Pulsformat, wobei die Zeitverzögerung zwischen den Pulsen ein spezifisches Merkmal darstellt. Eine neue Technik zur Einstellung vordefinierter Zeitverzögerungen über einen außerordentlich großen dynamischen Bereich hinweg wird folgend entwickelt und experimentell demonstriert.

Acknowledgments

A common theme is, that a PhD enables you to profoundly work on your own on a rich subject. While this is indeed correct, the most valuable wisdom I could take with me from this journey is that paradoxically, working independently does not mean the same as the habitual notion of simply doing things alone. The best way is seldom to accomplish your goals on your own but to understand how your evolving resilience and increasing competence play together with solid teamwork and mutual trust. Thus, with the right team at work and the best support in my private life, this thesis could be successfully carried out. Take that stupid pandemic!

This is why at this point, I would like to thank first and most importantly those people who stayed closest by my side: My family who was always there such that I could share my experiences, both good and bad ones. Second, my friends who always gifted me with the best times that here and there happened when I was outside of the lab.

Next, I would like to express my deepest gratitude to Prof. Andrius Baltuška for giving me the opportunity to carry out this thesis under his supervision. I never thought I would ever be able to contribute to such a diverse set of tasks and problems within these few years, not to mention the amount of knowledge and skills that come with it. I also would like to thank Dr. Tobias Flöry for introducing me to the lab work at the start of the doctoral program and for sharing parts of his broad knowledge of photonics and electronics with me. A lot of results in this work benefitted a lot from us playing well together as colleagues. Further, I would like to thank Dr. Audrius Pugžlys for teaching me so much about parametric amplification and Dr. Edgar Kaksis for showing me a lot of important life hacks in the lab. Not to forget Melanie and Christina for their work in the Secretary's office who helped me with various bureaucratic issues. I feel lucky that I could be a doctoral student in this group, where a cooperative and lively culture is the norm and not an exception. Therefore, I would like to express my sincere appreciation to all of its members, including former colleagues, long-term professionals, and newcomer students.

Contents

Chapter 1

Analytic Description of Pulse Bursts

This chapter gives an analytic description of ultrashort-pulse bursts. It starts with the, generally well-known, formalism for describing chirped pulses (Chapter 1.1). A formulation for a burst of ultrashort pulses is given in Chapter 1.2, including formulas for basic relevant burst parameters. Giving a full picture, Chapter 1.3 formulates equations for a whole train of pulse bursts, as it is generated in experiments at kHz repetition rates. For clearance, spatial effects are completely neglected (i.e. the fields only depend on time or frequency) and only Gaussian pulses with linear chirps are assumed since this approximation already allows for explaining all physical phenomena that are relevant to this work. The author notes that parts of this chapter were already published in a similar form in the author's work [1, 2].

1.1 Single pulse

The formulation for a single pulse starts in the frequency domain. This is motivated by the fact, that ultrashort pulses are stretched in time by prism or grating arrangements where a frequency-dependent delay of its spectral components is imposed. Pulses that are stretched in this way are also called "chirped" pulses, because of the time-dependence of their instantaneous frequency. This corresponds to a frequency-dependent phase, characterized by a single chirp parameter C in the case of a linear chirp. Followingly, a linearly chirped Gaussian pulse can be described in the frequency domain as [3]

$$\tilde{E}_P(\omega+\omega_0) = \tilde{E}_{\omega,0}\exp\left(-(1+jC)(\frac{\omega}{\omega_G})^2\right) \tag{1.1a}$$

$$\omega_{FWHM} = \sqrt{2\ln(2)}\omega_G \tag{1.1b}$$

with complex amplitude $\tilde{E}_{\omega,0}$, central frequency ω_0 and Full-Width-at-Half-Maximum (FWHM) bandwidth ω_{FWHM}. Please note that the frequency variable ω is taken here relative to the central frequency ω_0, as it is commonly done when applying the Slowly Varying Envelope Approximation (SVAE), i.e. the separation of the field into a slowly varying envelope and the fast-oscillating carrier wave, which is applied in all numerical applications in this work. The complex amplitude $\tilde{E}_{\omega,0}$ can be separated into its absolute value $|\tilde{E}_{\omega,0}|$ and its, with the given assumptions constant, phase

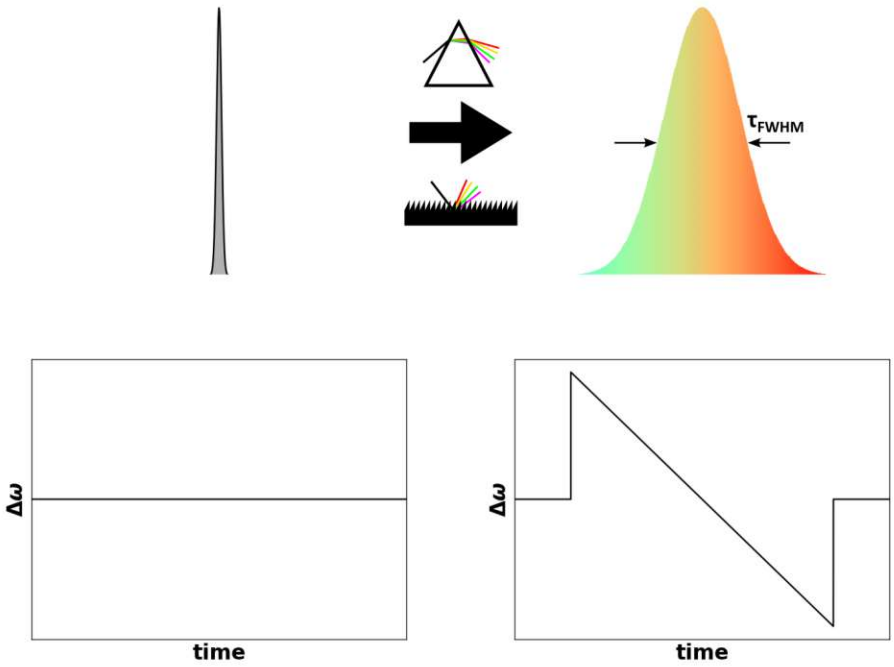

Figure 1.1: Concept of stretching a pulse by a prism or grating arrangement to induce a frequency-dependent delay. In the case of a compressed pulse, the instantaneous frequency deviation $\Delta\omega$ is constant (left plot). For a linear chirp, the instantaneous frequency deviation $\Delta\omega$ changes linearly in time (right plot).

$$\tilde{E}_{\omega,0} = |\tilde{E}_{\omega,0}| \exp(j\phi_P). \tag{1.2}$$

In this description, the time-domain description for the electric field of a pulse can be acquired by Fourier transformation to be

$$E_P(t) = E_{t,0} \exp\left[-i\omega_0 t - (1+iC)\left(\frac{t}{\tau_G}\right)^2\right] \tag{1.3a}$$

$$= \frac{\tilde{E}_{\omega,0}\sqrt{\pi}\omega_G}{\sqrt[4]{1+C^2}} \exp\left(i(-\omega_0 t + \Phi(t)) - \frac{\omega_G^2 t^2}{4(1+C^2)}\right) \tag{1.3b}$$

$$\Phi(t) = -\frac{1}{2}\arctan(C) + \frac{C\omega_G^2}{4(1+C^2)}t^2 \tag{1.3c}$$

Eq. (1.3c) shows the linear nature of the chirp, given a square-dependence on time of the time-dependent phase $\Phi(t)$. This gives for the time-dependent frequency

$$\omega(t) = \omega_0 + \Delta\omega(t) \tag{1.4a}$$
$$= \omega_0 + \frac{d\Phi(t)}{dt} \tag{1.4b}$$
$$= \omega_0 + \frac{C\omega_G^2}{4(1+C^2)}t, \tag{1.4c}$$

showing a linear increase.

With Eqs. (1.3a,1.3b), we get a formula for the chirp-dependent pulse duration τ_G

$$\tau_G = \frac{2\sqrt{1+C^2}}{\omega_G}. \tag{1.5a}$$
$$\tau_{FWHM} = \sqrt{2\ln(2)}\tau_G \tag{1.5b}$$

1.2 Ultrashort-Pulse Burst

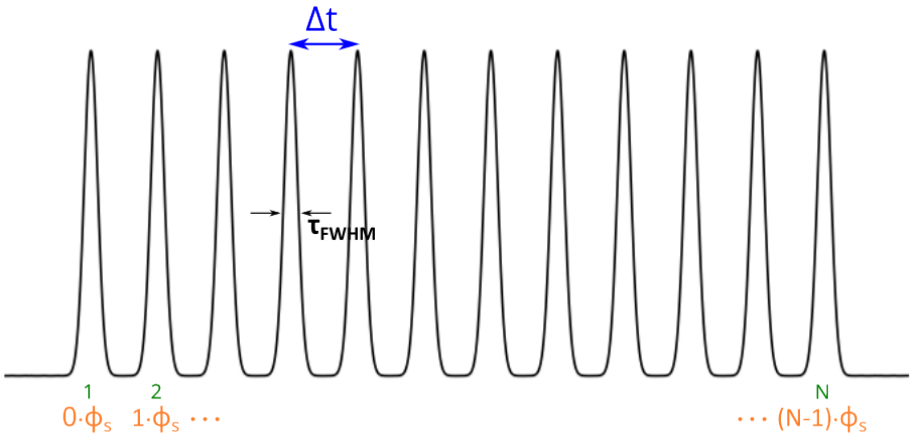

Figure 1.2: Depiction of a burst of N ultrashort pulses with an intraburst repetition rate of $f_{burst} = 1/\Delta t$, a τ_{FWHM} pulse duration and a constant pulse-to-pulse phase slip ϕ_s.

In the following, an ultrashort-pulse burst is defined as a finite train of ultrashort pulses that have a short temporal spacing Δt to each other, with the spacing being comparable to their ultrashort duration τ_{FWHM}. For describing ultrashort-pulse bursts analytically, it is assumed that all pulses are the same, only differing from each other by a constant pulse-to-pulse phase slip ϕ_s. This is motivated by the fact, that by the formation of an ultrashort-pulse burst with the Vernier method (see Chapter 2.3), the same phase relationship is imposed on the burst pulses. The analytical formulation of a burst consisting of N pulses with a Δt spacing is then given in the time domain by summation over the individual pulse fields $E_n(t)$ as following

$$E_B(t) = \sum_{n=0}^{N-1} E_n(t) \tag{1.6}$$

$$= \sum_{n=0}^{N-1} E_P(t - n\Delta t)\exp(in\phi_s), \tag{1.7}$$

with $E_P(t)$ as in Eq. (1.3).

The corresponding description in the frequency domain is given by

$$\tilde{E_B}(\omega+\omega_0) = \tilde{E}_P(\omega+\omega_0)\sum_{n=0}^{N-1}\exp\left(-in(\Delta t(\omega+\omega_0)-\phi_s)\right) \tag{1.8}$$

$$= \tilde{E}_P(\omega+\omega_0)\cdot\frac{1-\exp\left(-iN(\Delta t(\omega+\omega_0)-\phi_s)\right)}{1-\exp\left(-i(\Delta t(\omega+\omega_0)-\phi_s)\right)}, \tag{1.9}$$

which gives after some calculation

$$\tilde{E_B}(\omega+\omega_0) = \tilde{E}_P(\omega+\omega_0)\cdot\tilde{f}(\omega+\omega_0;\Delta t,N,\phi_s) \tag{1.10}$$

$$\tilde{f}(\omega+\omega_0;\Delta t,N,\phi_s) = \frac{\sin\left(\frac{N(\Delta t(\omega+\omega_0)-\phi_s)}{2}\right)}{\sin\left(\frac{\Delta t(\omega+\omega_0)-\phi_s}{2}\right)}\exp\left(-i\frac{N-1}{2}(\Delta t(\omega+\omega_0)-\phi_s)\right). \tag{1.11}$$

Hence, the spectral intensity of a burst is given by

$$I_B(\omega+\omega_0) = I_P(\omega+\omega_0)\cdot|\tilde{f}(\omega+\omega_0;\Delta t,N,\phi_s)|^2, \tag{1.12}$$

which is the product of the spectral intensity of a single pulse $I_P(\omega+\omega_0)$ and of the absolute-squared spectral interference factor $|\tilde{f}(\omega+\omega_0;\Delta t,N,\phi_s)|^2$, which describes intraburst spectral interference between burst pulses. For formulating the experimental key parameters, we will now switch to a formulation that includes the frequency f, instead of the angular frequency $\omega = 2\pi f$. This is done because it makes sense for a better relation to the experimental values. The most important result of the above analytical description for this thesis is the formation of equally-spaced spectral peaks at frequencies f_m according to

$$f_m = f_{offset} + m\cdot f_{burst}, \tag{1.13a}$$

$$f_{offset} = \frac{\phi_s}{2\pi\Delta t} \tag{1.13b}$$

$$f_{burst} = \frac{1}{\Delta t} \tag{1.13c}$$

where $f_{s,offset}$ is the phase-slip offset frequency and f_{burst} is the intraburst repetition rate. The maximum absolute value of the interference factor is N, in case the position of

a spectral peak coincides with the envelope maximum. The spectral peaks are equally spaced by the intraburst repetition rate f_{burst} and the width of spectral peaks Δf scales as

$$\Delta f = \frac{1}{N\Delta t}. \tag{1.14}$$

For long bursts, $N\Delta t$ is approximately the burst duration, which is $(N-1)\Delta t$ to be more precise.

The parameters of pulse spacing Δt, pulse number N and pulse-to-pulse phase slip ϕ_s are experimentally well-accessible quantities, which allow for rich shaping capabilities of ultrashort-pulse bursts by giving control over the spectral peak offset f_{offset}, the intraburst repetition rate f_{burst} and the spectral mode width Δf.

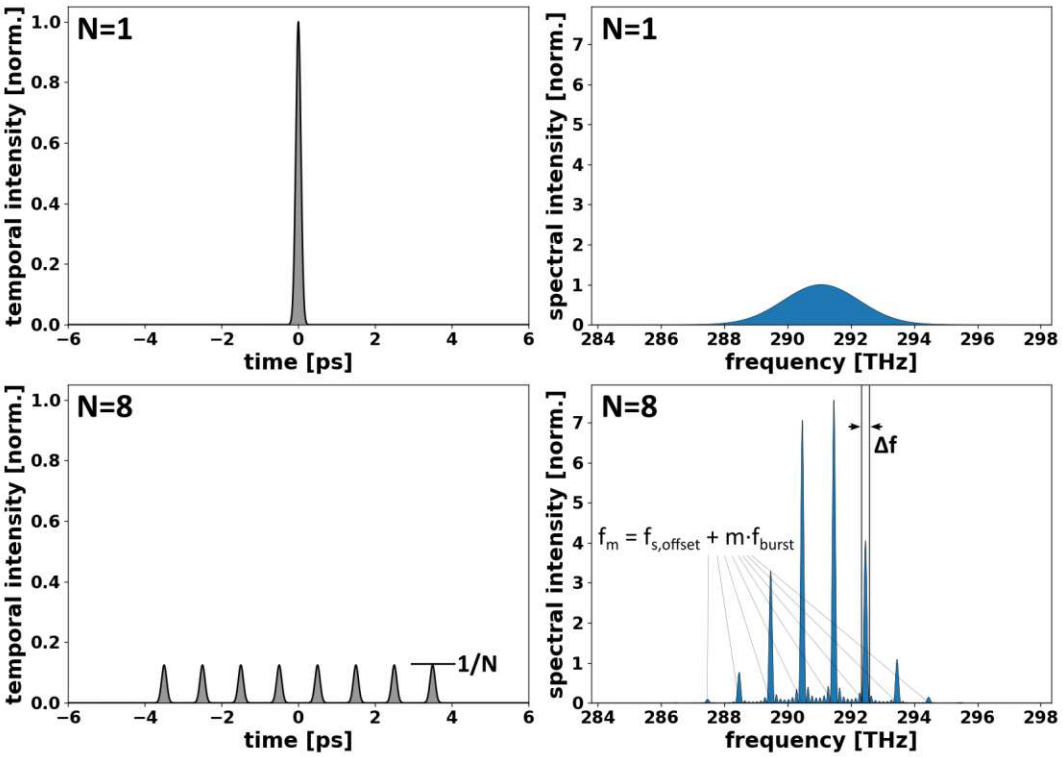

Figure 1.3: Temporal intensity profile and spectrum calculated for a single pulse (N=1, upper plots) and for a burst of 8 pulses (N=8, lower plots). The total energy is kept constant, which leads to an N-proportional decrease in temporal peak intensity for the burst, whereas the spectral peak intensity shows an N-proportional increase. In the lower right plot, the spectral peaks at positions f_m with spectral mode width Δf can be seen.

1.2.1 The Wigner Distribution

The Wigner distribution will play an important role in Chapter 7, since it gives useful insights with a time-frequency picture of a complex-valued signal. For the burst field it is [3]

$$\mathcal{W}_B(t,\omega) := \int_{-\infty}^{\infty} E_B(t+s/2)E_B^*(t-s/2)\exp(-i\omega s)ds. \tag{1.15}$$

For the N-pulse field (Eq. 1.6), the Wigner distribution consists of N signal terms $\mathcal{W}_{B,n}^{(S)}(t,\omega)$ and $N(N-1)/2$ inter-pulse interference terms $\mathcal{W}_{B,nm}^{(I)}(t,\omega)$ [4]

$$\mathcal{W}_B(t,\omega) = \sum_n \mathcal{W}_{B,n}^{(S)}(t,\omega) + \sum_{\substack{n \\ m>n}} \sum_m \mathcal{W}_{B,nm}^{(I)}(t,\omega) \tag{1.16}$$

Of further interest are the Wigner marginal integrals, i.e. the integration over the time axis which gives the spectrum $S(\omega)$ and the integration over the frequency axis, which gives the intensity in time $I(t)$:

$$S(\omega) = \frac{1}{2\sqrt{(\mu_0/\epsilon)}} \int_{-\infty}^{\infty} \mathcal{W}_B(t,\omega)dt \tag{1.17a}$$

$$I(t) = \frac{1}{2\sqrt{(\mu_0/\epsilon)}} \int_{-\infty}^{\infty} \mathcal{W}_B(t,\omega)d\omega \tag{1.17b}$$

In Eq. (1.17), μ_0 is the vacuum permeability and ϵ is the electric susceptibility. It is noted at this point that the Wigner distribution, as given in Eq. (1.15), is always a real-valued distribution with no imaginary part.

1.3 A Train of Ultrashort Pulse Bursts

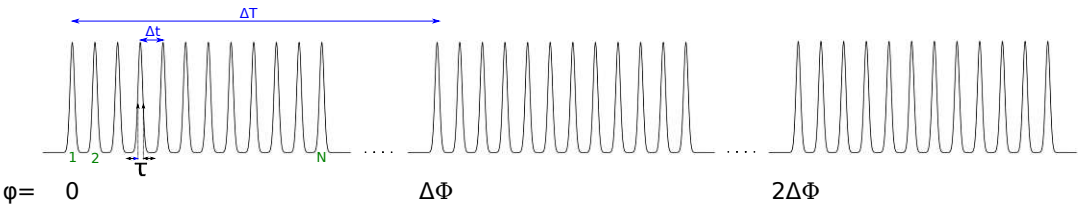

Figure 1.4: Bursts with pulse spacing Δt, burst spacing ΔT, pulse length τ and a burst-to-burst phase slip $\Delta\Phi$.

The spectral structure of a train of bursts is more complex than that of a single burst. It will be derived and evaluated in the following section what aspects may influence experimental results with pulse bursts. A finite train consisting of a certain number of M bursts, generated with a given interburst repetition rate f_{kHz}, is considered. The interburst repetition rate is denoted as f_{kHz}, since in practical cases of amplification, bursts are generated at kHz repetition rates when reaching sub-mJ, or higher, burst energies. Each of the M bursts consists of N pulses. As in Chapter 1.2, we assume that the intraburst phase slip ϕ_s is constant over the burst duration and is further set to zero for simplicity (or, equivalently, to some integer multiple of 2π). However, there can be a burst-to-burst phase slip $\Delta\Phi$, which is a phase slip between the first pulses of two subsequent bursts and which, for clarity, is also assumed to be constant.

With these assumptions mentioned, the temporal field of a train of bursts can be formulated as

$$E(t) = \sum_{m=0}^{M-1} E_B(t - m\Delta T) \exp(im\Delta\Phi), \tag{1.18}$$

with $E_B(t)$ given as in Eq. (1.7). The Fourier transform of Eq. (1.18) is

$$\tilde{E}(\omega+\omega_0) = \sum_{m=0}^{M-1} \tilde{E}_B(\omega+\omega_0) \exp(-im\Delta T(\omega+\omega_0)) \exp(im\Delta\Phi) \tag{1.19}$$

$$= \tilde{E}_B(\omega+\omega_0) \sum_{m=0}^{M-1} \exp(-im(\Delta T(\omega+\omega_0) - \Delta\Phi)) \tag{1.20}$$

$$= \tilde{E}_B(\omega+\omega_0) \cdot \frac{1-\exp(-iM(\Delta T(\omega+\omega_0)-\Delta\Phi))}{1-\exp(-i(\Delta T(\omega+\omega_0)-\Delta\Phi))} \tag{1.21}$$

which results after some calculation in

$$\tilde{E}(\omega+\omega_0) = \tilde{E}_P(\omega+\omega_0) \cdot f(\omega+\omega_0;\Delta t,N) \cdot g(\omega+\omega_0;\Delta T,M,\Delta\Phi) \tag{1.22a}$$

$$f(\omega+\omega_0;\Delta t,N) = \frac{\sin(\frac{N\Delta t(\omega+\omega_0)}{2})}{\sin(\frac{\Delta t(\omega+\omega_0)}{2})} \exp(-i\frac{N-1}{2}\Delta t(\omega+\omega_0)) \tag{1.22b}$$

$$g(\omega+\omega_0;\Delta T,M,\Delta\Phi) = \frac{\sin\left(\frac{M(\Delta T(\omega+\omega_0)-\Delta\Phi)}{2}\right)}{\sin\left(\frac{\Delta T(\omega+\omega_0)-\Delta\Phi}{2}\right)} \exp(-j\frac{M-1}{2}(\Delta T(\omega+\omega_0)-\Delta\Phi)), \tag{1.22c}$$

and thus, we get the spectral intensity of a train of bursts

$$I(\omega+\omega_0) = I_P(\omega+\omega_0) \cdot |f(\omega+\omega_0;\Delta t,N)|^2 \cdot |g(\omega+\omega_0;\Delta T,M,\Delta\Phi)|^2. \tag{1.23}$$

The first two factors in Eq. (1.23) are the spectral intensity of a single burst $I_P(\omega+\omega_0) \cdot |f(\omega+\omega_0;\Delta t,N)|^2$, with $\phi_s = 0$, which is the envelope of the burst train spectrum. Similarly to the single-burst case, there is a spectral interference factor $g(\omega+\omega_0;\Delta T,M,\Delta\Phi)$. It represents the formation of interburst spectral modes with kHz spacing, that result from spectral interference of individual bursts. However, for a train of bursts, as it is generated in practice, an infinite number of bursts $M \to \infty$ can be assumed in good approximation, which leads to a comb structure below the envelope (Fig. 1.5). The peak positions f_m, the intraburst repetition rate f_{burst}, and the peak width Δf are still related to the intraburst phase slip ϕ_s, the pulse number N and the pulse spacing Δt according to Eqs. (1.13a,1.13c,1.14), respectively. It can be seen, that the burst-to-burst phase shift $\Delta\Phi$ has no impact on the envelope $I_P(\omega+\omega_0) \cdot |f(\omega+\omega_0;\Delta t,N)|^2$, but only

on the frequency-offset of the comb. The comb lines are separated by the kHz interburst repetition rate

$$f_{kHz} = \frac{1}{\Delta T}, \tag{1.24}$$

which is directly proportional to the inverse burst spacing $1/\Delta T$.

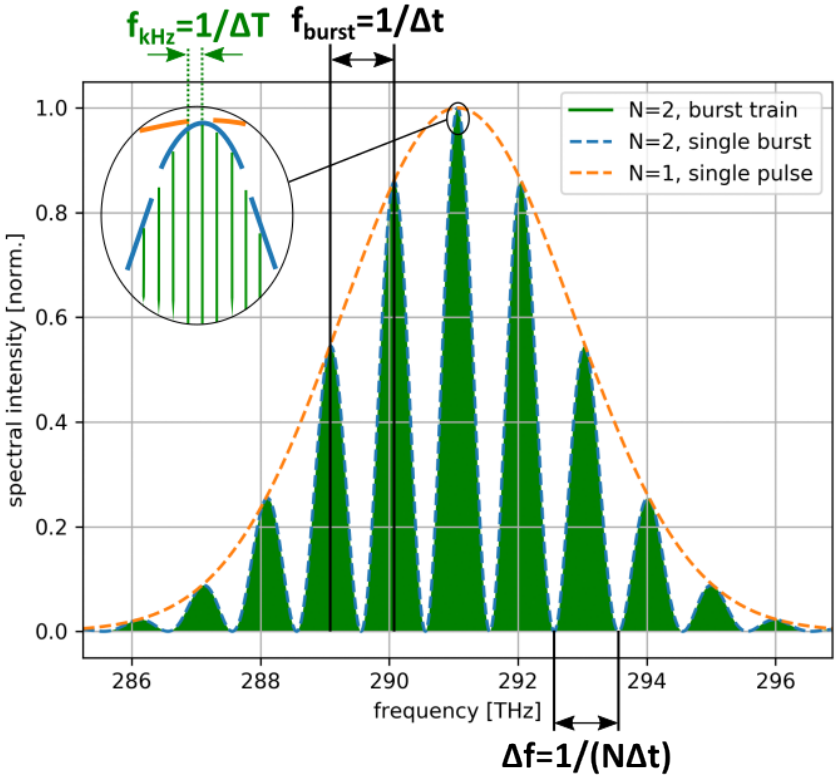

Figure 1.5: Calculated spectral intensity of a burst train with $N = 2$ pulses per burst. The spectra for a single pulse and a single burst are according to Eqs. (1.22a)-(1.22c). The comb structure is a depiction and not based on a calculation, since the kHz-spaced comb teeth are far too close together to be reasonably resolved in a plot.

Chapter 2

Ultashort-Pulse Burst Generation

In this chapter, several methods to generate pulse bursts are discussed. First, a general introduction is given which explains the usefulness of the burst format and its feasibility in various regimes (Chapter 2.1). For completeness, also some other types of pulse formats are introduced, that are frequency combs offering GHz repetition rates (Chapter 2.2.1) and nanosecond pulses generated from a cavity-dumped oscillator at MHz repetition rates (Chapter 2.2.2). The generation of pulse bursts with the Vernier effect is described in Chapter 2.3 which allows for burst formation with THz intraburst repetition rates. Finally, the stabilization of the intraburst phase slip of Vernier bursts is given in Chapter 2.4. The author notes that parts of this chapter were already published in a similar form in the author's work [5].

2.1 Introduction

Ultrashort laser pulses have a useful combination of properties, which are extraordinarily high intensity ($> 10^{15} W/cm^2$), femtosecond temporal resolutions and broad bandwidths that can reach even above an octave. For pulsed laser systems, the average output power P_{out} is given by the product of pulse repetition rate f_{rep} and pulse energy ϵ_P

$$P_{out} = f_{rep} \cdot \epsilon_P. \tag{2.1}$$

As a consequence, while achieving sufficiently high pulse energies at a certain average output power achievable by a laser system, one is limited in the repetition rate of pulses. Practically, depending on the application, repetition rates vary from less than 1 Hz (as for inertial fusion systems [6]), to several hundred megahertz for e.g. certain photochemistry applications [7], to sub-100 GHz repetition rates as achieved with frequency combs generated in high-Q silicon-nitride spiral resonators [8], or even 450 GHz as reported by Dutt et al. [9] with the use of comb-generating high-Q microring resonators.
Alternatively, for repetition rates larger than a GHz, the trade-off between repetition rate and pulse energy, as imposed by Eq. (2.1), can be resolved by the transition to another pulse format. Instead of generating a single pulse at a given repetition rate f_{rep}, one can generate a burst of pulses, that is a packet of closely spaced equidistant pulses. This way, the repetition rate can be dramatically increased within the burst, while keeping a high pulse energy without the need to increase average power. It also solves the limit in energy

scaling of several applications that arise because of the onset of ionization when amplifying a single ultrashort pulse. Instead, the whole burst energy can be distributed among several ultrashort pulses in burst mode. The repetition rate within the burst is commonly called the intraburst repetition rate, while the burst repetition rate is denominated as the interburst repetition rate. In the GHz regime, a burst can be generated by the application of a GHz mode-locked oscillator followed by a repetition rate multiplier (RRM) [10–17] and subsequently picking a whole pulse packet with an AOM [18] prior amplification at a certain interburst repetition rate (See Fig. 2.1).

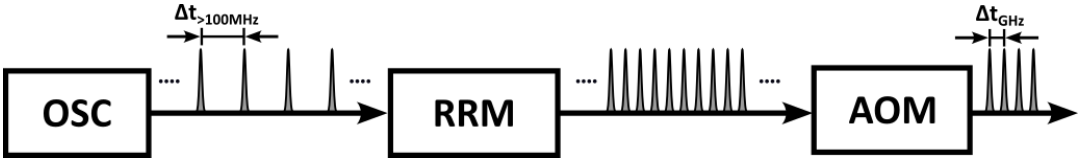

Figure 2.1: A typical method to generate ultrashort pulse bursts with GHz intraburst rates.

Various applications, however, benefit from bursts with intraburst repetition rates with hundreds of GHz or higher, up to the THz range. Yet, existing burst-mode systems working at THz intraburst repetition rates can only work at pulse numbers of about 10 pulses, and rarely up to 100 pulses (See Fig. 2.2). In this regime, common burst generation techniques rely on single-pulse splitting, recombination of multiple pulses, or a combination of both. Pulse shapers [19–22] disperse a beam spatially and apply a spatial filter in the Fourier plane to either filter dedicated frequencies or apply suitable spectral phase filters, such that a single pulse is transformed into a burst. Coherent beam combining by using beam splitters [23] can be used to combine multiple pulses into a train of pulses by fine-tuned alignment to achieve a common beam profile for all pulses. In birefringent crystals, ordinary and extraordinary pulse components experience different group velocities, this effect can be used to generate a burst of 2^n pulses with n-cascaded birefringent crystals [24–26]. Nested Mach-Zehnder interferometers divide a single pulse into several copies and recombines them at the output, which requires interferometric stabilization of the interferometer arms [27]. Independent of the approach, the practical limit in pulse number is ten to about hundred pulses due to the $1/N$ energy throughput of pulse division techniques [27].

One of the central efforts of this thesis is to further develop the Vernier technique for burst generation, which relies on burst pulse buildup with a MO-RA combination without splitting pulse beam paths, and whose pulse scalability is only limited by the RA round-trip time (See Chapter 2). This corresponds to an uncompetitive pulse number scalability of $\gg 100$ pulses at THz intraburst rates and opens up the possibility of using this method for a multitude of applications.

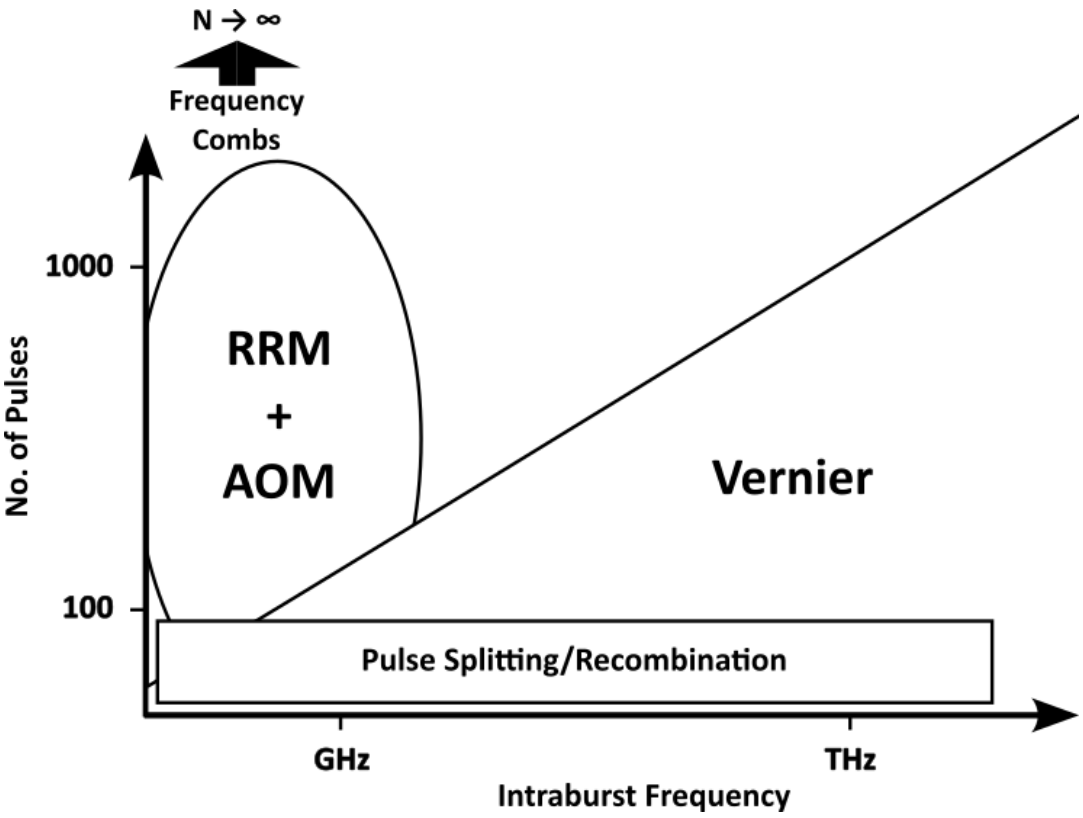

Figure 2.2: Several methods of pulse burst generation.

2.2 Comparison with Other Pulse Formats

2.2.1 Frequency Combs

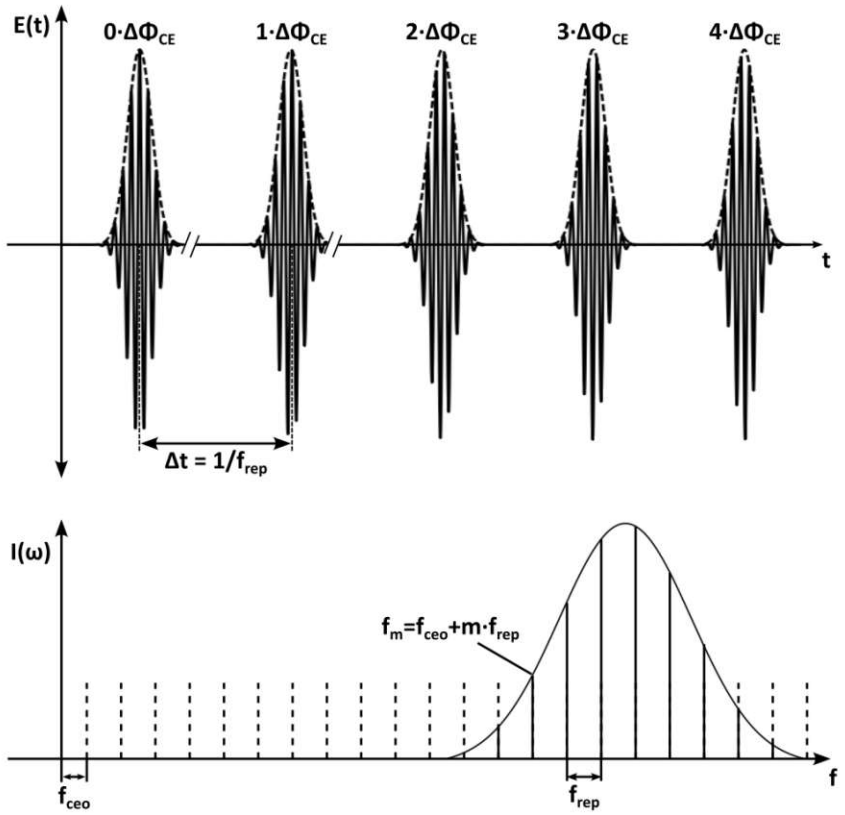

Figure 2.3: Depiction of the time- and frequency-domain characteristics of a frequency comb with a pulse-to-pulse carrier-envelope phase shift. Figure adapted from [28].

The research field of frequency combs has grown tremendously in the previous decades, benefitting a multitude of applications, such as high-precision spectroscopy, optical metrology, and many more [29]. A laser source, which is denoted as a frequency comb, has a broad spectrum that is composed of narrow lines with equidistant spacing [28]. Equivalently, a frequency comb consists of an infinite train of coherent phase-locked pulses coming from a mode-locked oscillator. There may, however, be a constant phase shift $\Delta\Phi_{CE}$ in the carrier-envelope phase (CEP), which can be understood as the phase of the carrier wave relative to the pulse envelope [30]. An infinite number of pulse copies, which only differ in their CEP by such a constant phase shift, leads to narrow comb lines in the spectral domain at positions (see Fig 2.3)

$$f_m = f_{ceo} + m \cdot f_{rep}, \tag{2.2}$$

with f_{rep} being the pulse train repetition rate, and f_{ceo} being the carrier-envelope offset (CEO) frequency given by

$$f_{ceo} = \Delta\phi_{CE}/(2\pi\Delta t). \tag{2.3}$$

The mathematical relation between the CEO frequency f_{cep} of a comb and its pulse-to-pulse CEP shift $\Delta\phi_{CE}$ (Eq. (2.3)) is equal to the mathematical relation between the phase-slip offset frequency f_{offset} and the intraburst phase slip ϕ_s of a burst of pulses (Eq. (1.13b)). Further than that, the spacing of the comb modes is given by the repetition rate f_{rep} of the comb train, in equivalence to the spacing of spectral burst peaks, which are given by the intraburst repetition rate f_{burst}.

Therefore, ultrashort-pulse bursts, being finite trains of ultrashort pulses, share a lot of properties with frequency combs, being infinite trains of ultrashort pulses. Their differences, however, have many consequences on their application:

- In contrast to frequency combs, pulse bursts have spectral peaks/lines with a much larger width, given by the inverse burst duration (Eq. (1.14)), which makes them more attractive for applications that require higher spectral intensity with low spectral resolution when only stabilizing the intraburst phase slip. This approach could be successfully developed into a mature state in the course of this thesis (Chapter 2.4).
- Pulse bursts show two types of repetition rates, their intraburst repetition rate (in the $>$ GHz range) and their interburst repetition rate, which is magnitudes lower than the former (in the kHz range). This has consequences on its full spectral characteristic properties (see Chapter 1.3), where the spectral peak structure is an envelope with equidistant comb modes beneath. Stabilization of the full burst-comb spectral structure can be achieved by using a CEP-stable oscillator for seed pulse generation together with a stabilization of the phase slip. This holds promise for future high-precision spectroscopic applications.

2.2.2 Pulses from Cavity-Dumped Nanosecond Sources

Cavity dumping [31] is a technique that is strongly related, but not equal, to Q-switching. Both techniques are based on control over the Q-factor of a cavity. However, cavity dumping has the advantage of generating high energy, nanosecond pulses at higher (up to MHz) repetition rates as compared to Q-switching, where an increase in repetition rate is related to several issues, such as an increase in pulse duration [31, 32]. In the following, a short introduction to cavity dumping as a technique is given. Further, experimental efforts are described to provide insights into novel methods for energy-stable cavity-dumped systems at MHz repetition rates.

The Q-factor of a cavity is in general defined as the ratio of the energy stored inside a cavity over the power dissipated per round-trip, i.e. it is the capability of a cavity to maintain its energy [33]. Power dissipation includes all kinds of losses, such as leakage through mirrors, scattering or diffraction losses, and is thus strongly related to the photon lifetime of a cavity. It is common in laser engineering to dynamically control the Q-factor with an optical switch such as a Pockels Cell in combination with a waveplate and a polarizer (see Chapter 2.3). Cavity dumping utilizes control over the Q-factor to generate

high-energy pulses from an oscillator.

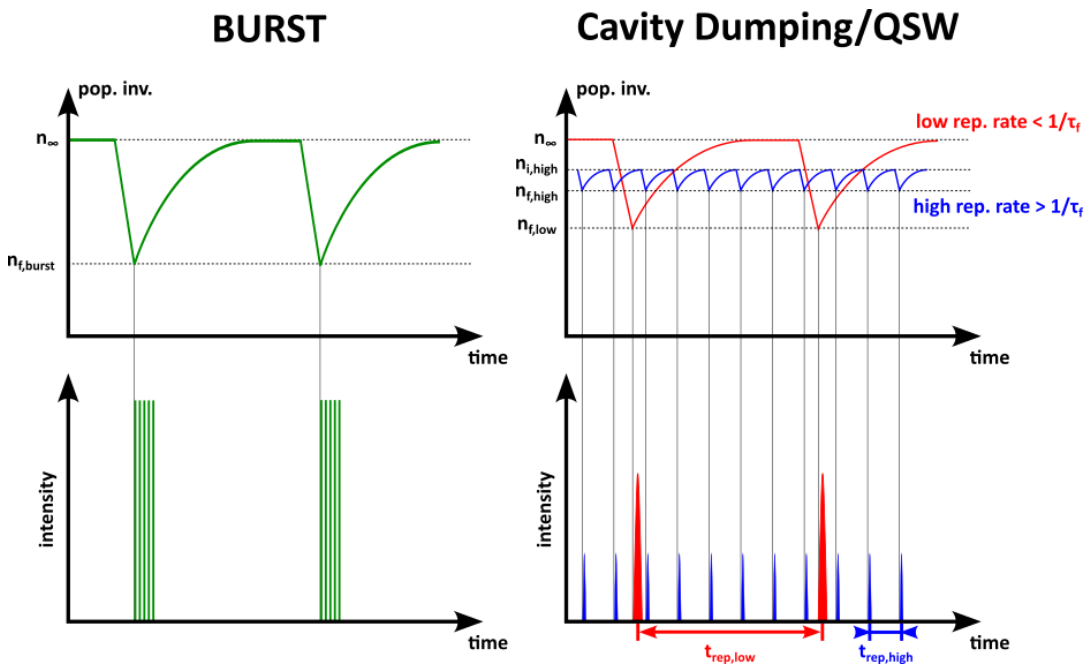

Figure 2.4: Conceptual comparison of pulse bursts with Cavity-Dumped/Q-switched pulses. The shown characteristical features (inversion variation and output intensity) are qualitatively equal for cavity-dumped and Q-switched systems. Top: Population inversion over time. Bottom: Temporal Intensities. The Cavity-Dumped/Q-Switched pulses are depicted for two cases: First, with a repetition rate being lower than the inverse fluorescence time (rep. rate $< 1/\tau_f$) of the laser crystal. Second, with a repetition rate being higher than the inverse fluorescence time (rep. rate $> 1/\tau_f$) of the laser crystal. The upper right diagram was adapted from [34].

In cavity dumping, there exist two kinds of cavity modes: the low-Q state in which the optical switch is set such that the round-trip losses are much higher than the round-trip gain, preventing the onset of lasing. When a laser cavity is continuously pumped, the population inversion in the crystal increases, until it reaches saturation at a level n_∞ where the pumping rate to the upper laser level is equal to the transition rate to the lower laser level due to fluorescence (plus eventual other non-radiative types of transition). Typically, this happens within timescales of the fluorescence time τ_f of the crystal. At this point, the oscillator can be switched into the high-Q mode, in which the optical switch is set such that round-trip losses are minimized. The round-trip losses are then much lower than the round-trip gain, with the round-trip gain having experienced a strong increase during the low-Q state because of the strong buildup of population inversion in the lasing level. As a consequence, amplification of coherent intracavity radiation starts. The optical seed for the amplified radiation is for cavity dumping the residual intracavity radiation from the previous cavity-dumped cycle that is maintained throughout the low-Q mode. After sufficient amplification, the pulse can be emitted out of the laser cavity when switching the system back into the low-Q mode within one round-trip time. This is in contrast to Q-Switching where onset of lasing starts from spontaneous emission and almost all of the

accumulated intracavity optical energy is directed into the output pulse, limited by the finite contrast ratio of the optical switch.
Cavity dumping is essentially suitable at high MHz repetition rates as opposed to Q-switching. In cavity dumping, the pulse is released within one round-trip time by a fast optical switch, whereas in Q-switching, the pulse outcouples through an outcoupling mirror over many round-trip times. This has consequences on [32]

- **Pulse duration:** When the variation in population inversion (and thus in the energy stored in the crystal) decreases at high repetition rates (see Fig. 2.4) the pulse duration increases for Q-switched systems. This effect does not take place in cavity-dumped systems, where the pulse duration only depends on the cavity round-trip time.

- **Timing jitter:** The moment of pulse emission is clearly defined by the timing jitter of the fast optical switch. For commercial nanosecond rise-time electro-optic modulators, jitters of electrical output pulses are in the order of < 100 ps. An example is the PCD-UHR series from EKSPLA providing a timing jitter of < 50 ps.

- **Pulse energy stability:** The whole optical energy couples out of the cavity in Q-switched systems, while in cavity dumping one can decide how much optical radiation is left inside the cavity. By leaving a certain amount of optical radiation inside the cavity, one can use this radiation as a defined seed for the next cycle. This allows the generation of pulses at MHz repetition rates with their energy growing from a defined and energetic optical seed instead of stochastic spontaneous emission on a microscopic energy level and further decreases buildup time. The only trade-off in this case is efficiency, the higher the residual intracavity radiation, the lower the efficiency of the system.

In our group, we work on a project in cooperation with the Automation and Control Institute (ACIN) from TU Wien and the Lithuanian laser company EKSPLA, to find novel techniques with which we can optimize the repetition rates of cavity-dumped self-seeding laser oscillators, with pulse energies that are more stable than sources as currently available on the market. Spectra Physics offers a high-power hybrid fiber laser system providing repetition rates up to 3.5 MHz with pulse-to-pulse stability of fewer than 5% [35]. To develop a system that can outperform these characteristics, we combine state-of-the-art methods of laser engineering with control engineering based on a numerical model of a laser. The latter is needed, because pulse energy stability strongly depends on population inversion dynamics at MHz repetition rates. In course over the previous years, Dr. Andreas Deutschmann and Lukas Tarra from ACIN were able to develop efficient control models that could already be validated with one of your Yb:CaF_2 systems as can be seen in Fig. 2.5. Details of the numerical model can be found in [36, 37].

The time until the population inversion of the lasing level achieves its steady state n_∞, i.e. where it is in equilibrium with fluorescence, is given by the fluorescence time

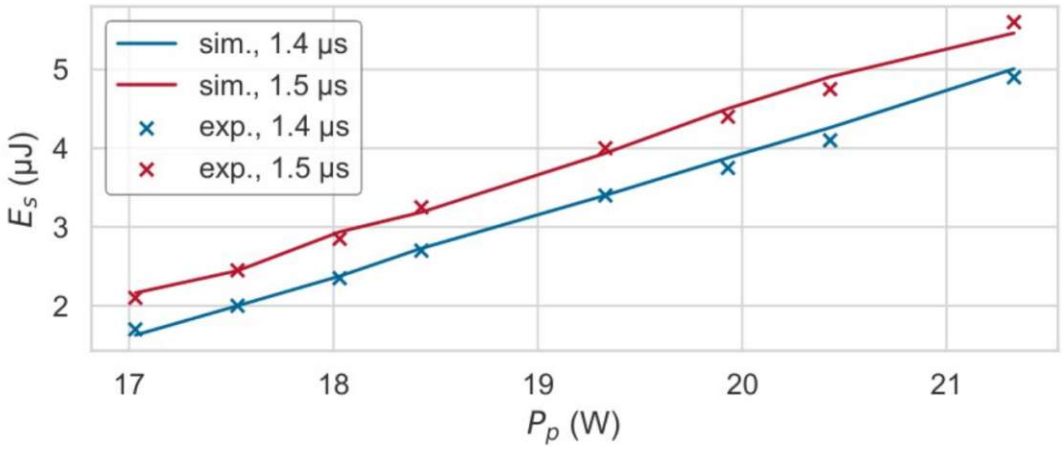

Figure 2.5: Output energies of an Yb:CaF_2 system operating at 200 kHz as simulated by L. Tarra in comparison with experimentally measured data. Plot from L. Tarra and published in [36].

Crystal	Lifetime [µs]
Nd:YAG	230
Nd:Glass	290...340
Nd:YLF	480
Nd:YVO4	100
Er:Phosphate	8,000
Ti:Al2O3	3.2
Cr:LiSAF	67
Tm:YAG	10,000
Yb:YAG	951

Table 2.1: Fluorescence lifetimes for several laser crystals as given by [34].

τ_f of the crystal [34]. At low repetition rates (rep. rate $< 1/\tau_f$), the fluorescent limit n_∞ serves as an anchor for the inversion dynamics. Stable pulse energies are achieved because the stored energy, as population inversion inside the crystal, is always the same prior transition from the low-Q to the high-Q state. Typical fluorescence times are given on microsecond to millisecond time scales (see Tab. 2.1). For repetition rates much higher than this, population inversion does not reach the fluorescent limit n_∞ and the difference between initial and final inversion decreases (See Fig. 2.4, right side). Because the upper inversion level is not bound to a determined value, the generation of stable pulse energies requires information about the population inversion.

The repetition rate increase of energy-stable pulsed laser sources is of high industrial interest since laser pulses with nanosecond pulse durations and sub-millijoule energies are used for a variety of applications. Examples are deep space optical communication [38] and micromachining, where it can be applied for e.g. marking [39], advanced packaging [40], solar [41], automotive [42] or to treat retinal disorders [43]. However, to achieve better pulse-to-pulse energy stability at MHz repetition rates, studies and techniques to access inversion dynamics are highly necessary. The results of such studies make it possible to compensate for dynamical inversion effects by controlling the cavity parameters. Motivated

by this, an experiment was performed in the course of this thesis to actively probe the inversion of a Nd:YAG oscillator (10 W output power, 5 ns pulse duration) Q-Switched at a repetition rate of 1 MHz. In Fig. 2.6, the experimental setup can be seen. The linear cavity consists of a Nd:YAG crystal, which is continuously pumped by a 22 W fiber-coupled diode laser (FCDL, Jenoptik JOLD-30-FC-12), a Pockels Cell (PC), a quarter waveplate (QWP), two end mirrors and two thin-film polarizers (TFP1, TFP4). The two intracavity TFPs are used to set a defined s-polarization at the output, which is at TFP1 next to the PC-QWP pair. The combination of PC, QWP and output TFP1 serves as an electronically controllable output coupler. The cavity output is attenuated by a combination of half waveplate (HWP1) and TFP2 because the pulse energy is much larger than required for the sensitive photodiodes (Thorlabs PDA10A2, 150 MHz) used. Further, a Glan-Taylor polarizer is implemented because of slight depolarization of the output pulses coming from thermal depolarization in the crystal. A HWP-TFP pair (HWP2, TFP3) is used to separate the attenuated output into a reference pulse and a probe pulse. All pulse energies are measured on a shot-to-shot basis with a high GSPS oscilloscope (LeCroy WaveSurfer 42MXs-B, 400 MHz, 5 GSPS) which can resolve the individual pulses. The probe pulse couples back into the cavity over TFP4. HWP3 and a Faraday Rotator (FR) flip the polarization of the probe pulse upon propagation back and forth, such that it can be detected upon back-reflection on TFP3 by a photodiode (PD_probe). To determine the inversion dynamics, two measurements were performed: first, a reference measurement was done by placing a mirror M_{ref} in between FR and TFP4 such that the probe pulse did not enter the cavity and experience absorption/gain from the crystal. Next, the mirror was removed and the probe pulses passed the crystal twice while overlapping with the cavity mode. The absorption/gain of the probe pulse through the crystal is then a measure for the final inversion inside the crystal that is left after the buildup of the pulse.

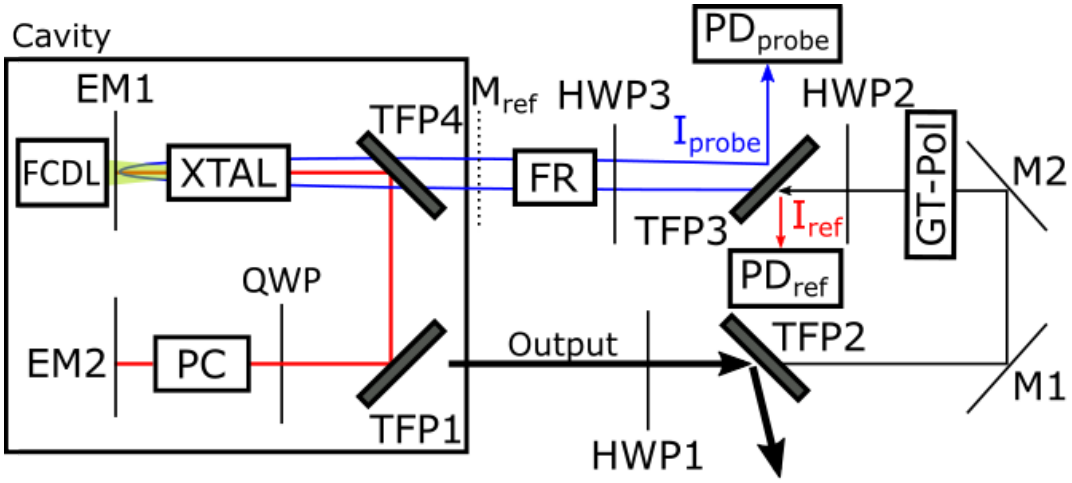

Figure 2.6: Experimental setup for actively probing inversion dynamics in a MHz cavity-dumped oscillator.

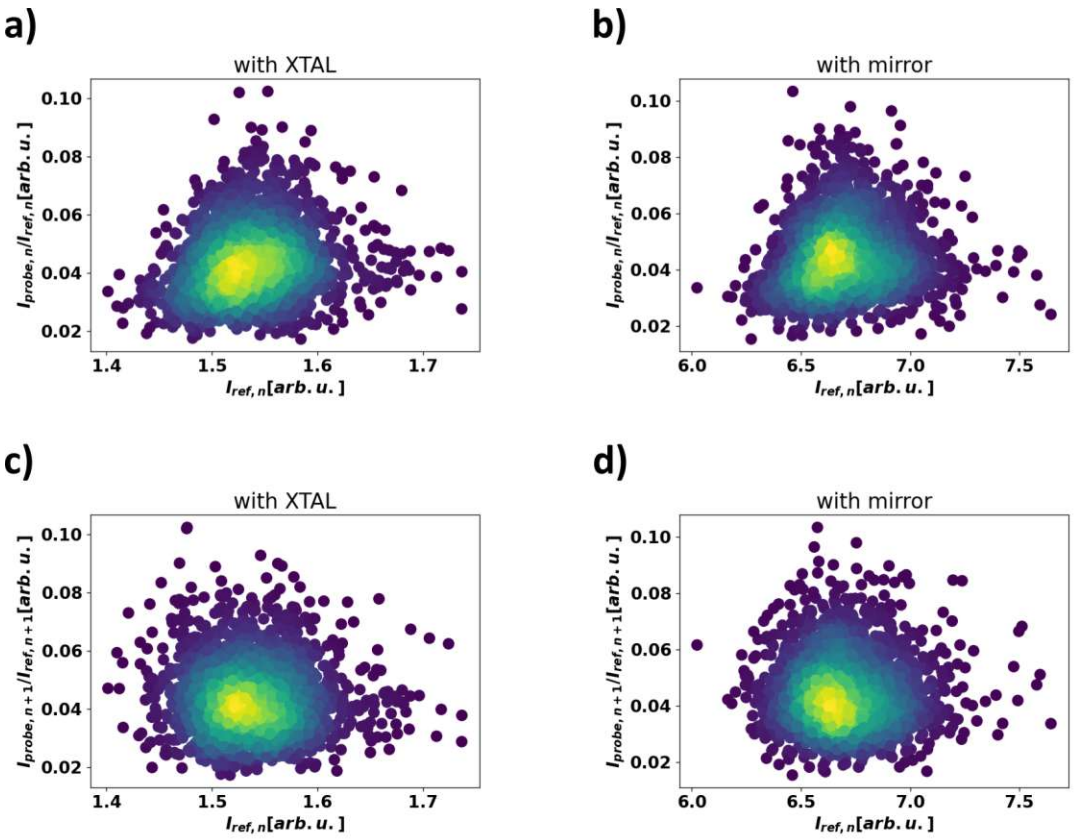

Figure 2.7: Inversion measurement scatterplots of a Nd:YAG oscillator Q-Switched at 1 MHz. The back-reflected probe relative intensity (vertical axis) is always taken relative to the reference intensity of the same cycle. On the horizontal axis, the reference intensity is given. a-b) Back-reflected probe relative intensity coming from the same cycle n as the probe intensity, a) with crystal, b) with mirror M_{ref}. c-d) Back-reflected probe relative intensity coming from the cycle $n+1$ subsequent to the cycle n of the reference intensity on the horizontal axis, c) with crystal, d) with mirror M_{ref}.

The results of the measurement are plotted in Fig. 2.7. The data is represented as scatterplots to investigate the correlation distribution of each measurement set. The probe intensity is shown relative to the reference intensity on the vertical axis. The horizontal axis is used for the reference intensity. The results are plotted in two ways: once the relative probe intensity of cycle n is shown depending on the reference pulse intensity of the same cycle n. Next, the relative probe intensity of cycle $n+1$ is shown depending on the reference pulse intensity of its preceding cycle n. When comparing relative probe pulse intensities with that of the reference pulse from the same cycle, a slightly higher positive correlation between reference intensity and probe intensity can be seen, showing that absorption, and thus remaining inversion, was lower when the output pulse energy was higher. When comparing subsequent cycles (n and $n+1$), the intensities were uncorrelated when comparing intensities. This can be explained, by a stochastic seed which initially sets the foundation of the intracavity signal [36]. Thus, no intracavity radiation was left inside the cavity after emitting the pulse. The stochastic seed consists of a set of coherent photons that happen to exist by chance at the same time with comparable frequency and momentum inside the crystal, overlapping with the cavity mode. The number of seed

photons can vary strongly, leading to a decoupling of pulse energies and inversion from cycle to cycle. In general, the results confirm well the need for cavity-dumped operation, showing that the dominating source of pulse energy noise is the stochastic seed. It further shows the viability of active inversion-probing techniques that can be combined with a model approach to achieve stable, high-repetition-rate cavity-dumped oscillators.

2.3 Generation of Ultrashort-Pulse Vernier Bursts

The Master Oscillator - Power Amplifier (MOPA) scheme [44] is widely used to decouple the challenges of pulse generation, which adheres to the oscillator, and of pulse amplification, which is performed by one or several amplification stages. In between the oscillator and the amplifier, a pulse picker can be used to select a pulse for amplification. If ultrashort pulses are generated, Chirped Pulse Amplification (CPA) [45] needs to be applied, which means application of a stretcher between the oscillator and the pulse picker, such that pulse intensities are lowered in the amplifier to avoid optical damages, and a compressor after amplification to recompress pulses, at best near to their bandwidth-limit.
Regenerative amplifiers (RA), which include a laser cavity with an optical switch (often an electro-optic switch, such as a Pockels Cell, in combination with a waveplate and a polarizer), allow amplification to high, millijoule energies with small system size and are thus an efficient solution [46]. By including an optical switch, the RA can be in one of two states: open or closed. When a seed pulse approaches the RA cavity, the cavity is kept open. After the pulse has entered the cavity, the RA is switched within the RA round-trip time into its closed mode, such that the seed pulse is preserved inside the RA cavity. By that, the seed pulse fulfills multiple round-trips while experiencing a gain in every turn. This is done until the pulse has achieved enough energy for its application and the RA cavity is switched back into its open state. If a Pockels Cell (PC) is used as an electro-optic switch, the process of switching between open and closed cavity mode happens by setting the PC voltage either to zero or full level.

As already shown in [2], it is possible to generate bursts of ultrashort pulses with an enormously high repetition rate with such a MO-RA combination (See Fig. 2.8) if

- The round-trip lengths of MO and RA are detuned from each other, giving a difference of ΔL. The absolute value of the round-trip time difference gives the intraburst pulse spacing
$$\Delta t = \frac{|\Delta L|}{c_0} \tag{2.4}$$
- The optical switch can be run in three modes: open cavity, pulse accumulating cavity or closed cavity.
- For each round-trip, the pulse losses are equal to the pulse gain when being in pulse accumulation mode.

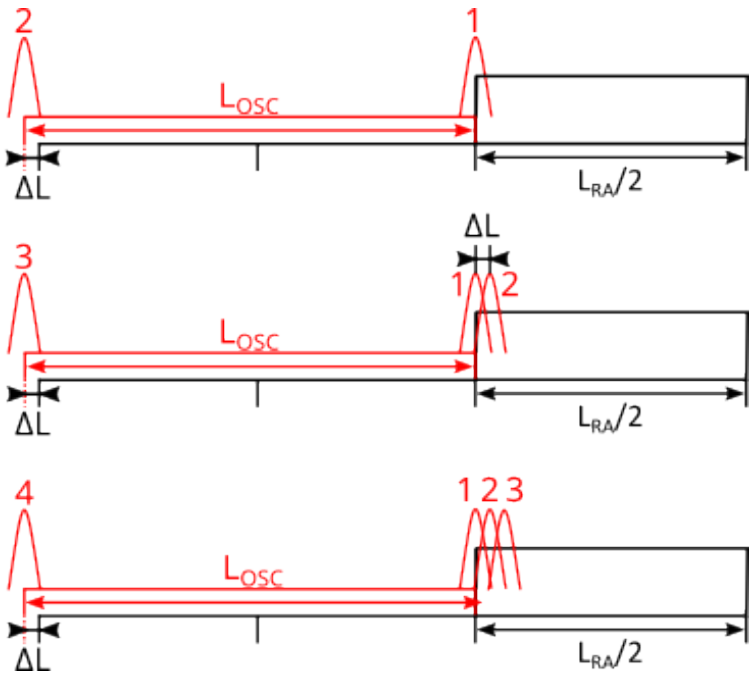

Figure 2.8: Concept of the Vernier technique for ultrashort-pulse burst generation using a MO-RA combination. Incoming pulses are separated by the oscillator round-trip length L_{OSC}. When the PC voltage is set, such that round-trip losses equal the round-trip gain in the RA cavity, burst pulses are accumulated in the RA cavity with the spacing of the round-trip detuning length $\Delta L = |L_{RA} - L_{OSC}|$.

When these conditions are fulfilled, the pulse accumulation mode leads to a buildup of pulses inside the RA cavity with a temporal pulse spacing of Δt. Further than that, in contrast to pulse splitting and recombination techniques, all burst pulses couple into a closed cavity mode of the RA, resulting in one clean beam rather than multiple combined beams.
Another result is the generation of an intraburst phase slip ϕ_s, that is given by

$$\phi_s(\omega) = k(\omega_0)\Delta L, \tag{2.5}$$

with ω_0 being the central frequency of the pulses and the approximation that the phase slip is constant over the full pulse bandwidth. An analog description can be given based on the round-trip times of oscillator τ_{OSC} and RA τ_{RA}:

$$\phi_s = \omega_0(\tau_{RA} - \tau_{OSC}) = \omega_0\Delta\tau, \tag{2.6}$$

where $\Delta\tau$ is the round-trip time detuning between RA and oscillator, whose absolute value is equal to the interpulse spacing Δt.

2.4 Stabilization of the Intraburst Phase Slip

Thermal drift and mechanical vibrations lead to variations in the cavity round-trip times, thus affecting the intraburst phase slip and the burst spectrum. This leads to unstable phase offsets preventing a useful application of ultrashort-pulse bursts at THz intraburst repetition rates since their reproducibility is not given. Therefore, in order to maintain a stable burst spectrum, the cavity detuning ΔL, and by that the intraburst phase slip ϕ_s, needs to be stabilized to a constant value [2]. This problem is similar to commonly known effects in CEP drift with a multitude of techniques already developed [47–49] that, to date, have been applied to continuous pulse trains of mode-locked oscillators.
The spectral peak structure of a burst was already discussed in Chapter 1, which is a result of interpulse spectral interference. In the following, it will be shown, how the spectral interference can be utilized to stabilize the intraburst phase slip. First, a method applying a separate reference pulse train is demonstrated (Chapter 2.4.1). Then, another method is demonstrated which works without any external reference by only measuring the intracavity signal of the amplifier. In this case, the large THz spacing of burst spectral peaks is taken advantage of, since it is large enough to be resolved on commonly available commercial spectrometers (Chapter 2.4.2). While the former stabilization method has the advantage, that the reference train allows to stabilize burst pulse spacings on arbitrary time scales, the latter is much simpler to apply without the need for any additional resources for existing MO-RA systems.

2.4.1 Intraburst Phase Slip Stabilization with a Reference Pulse Train

A reference pulse train can be used to probe the cavity length detuning for implementing an active feedback control of the intraburst phase slip (Fig. 2.9). The reference pulse train can be derived from the oscillator, that provides the seed pulses for amplification. In the given case, this is achieved by using the non-diffracted pulse train from an acoustic-optical modulation (AOM) pulse picker (see Fig. 2.9). The differential cavity length drift is stabilized by monitoring the spectral interference of consecutive pulses in the non-diffracted beam at the MO repetition rate f_{MO}. One of the interfering reference pulses is reflected off a beamsplitter and the other one undergoes one complete RA roundtrip (see inlay of Fig. 2.9). The spectral interference can be measured with a spectrometer, with the spectral period given by the temporal spacing of the two reference pulses on the spectrometer. Subsequently, the intraburst phase slip, as seen by the reference pulse train, can be determined from the Fourier transform of the interference spectrum. Any deviation of the intraburst phase slip from its predetermined value can be compensated by adjusting the round-trip length of the RA by driving a piezo-electric transducer (PZT) that is attached to a mirror in the cavity. It is recommended that the PZT-driven mirror is a flat mirror and that it is also one of the end mirrors with a collimated cavity mode at its place (such that the change in mirror position has negligible impact on the cavity mode parameters). The advantage of this approach is that one can stabilize intraburst phase slips of bursts with various pulse spacings. This is because the delay between the BS-reflected reference

pulse and the pulse fulfilling the RA round-trip is set by the BS position. Thus, one can adjust the BS position in such a way, that the spectral interference can be resolved by the spectrometer over a large range of burst spacings.
Stabilization results can be seen in Fig. 2.10. The phase drift could be compensated for the reference while the stabilization was turned on. For the phase of the amplified burst, a slight phase drift of 0.16 rad/min remained, corresponding to a round-trip length detuning drift of 26.5 nm/min.

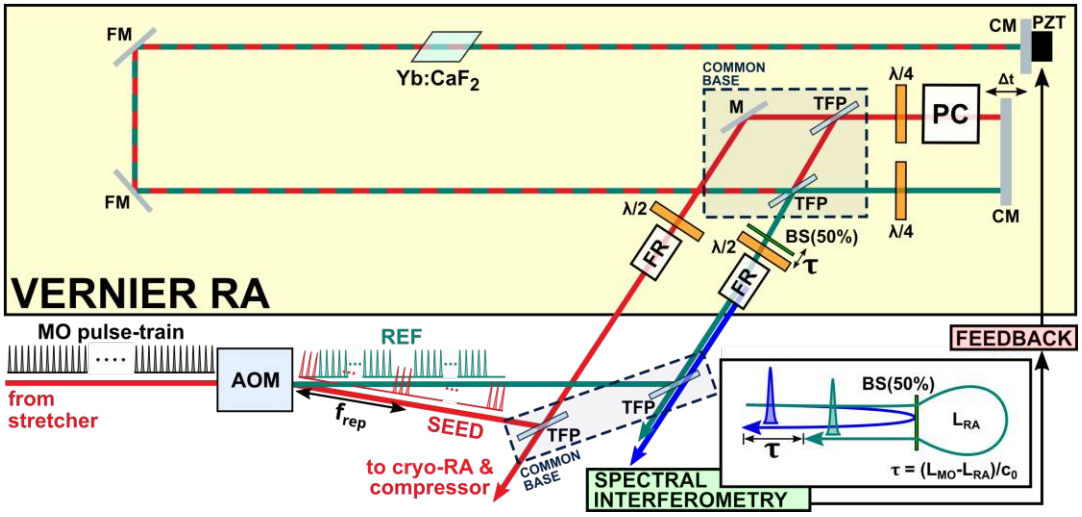

Figure 2.9: Detailled scheme of the Vernier RA with burst formation and phase slip stabilization. Pulses with a sufficiently long temporal spacing are diffracted from the MO pulse train (black) with an AOM, which enables individual amplitude and phase modulation. The diffracted pulses (red) are used as the burst seed, and the non-diffracted pulses (turquoise) are used as a high-repetition-rate reference for measuring the phase slip drift. The seed pulses are accumulated and amplified in the RA cavity. Inlay: Concept of the interferometric phase slip drift measurement. The reference pulses are split into two pulses. One (blue) is reflected from a beamsplitter (BS), and another (turquoise) fulfills a roundtrip in the RA cavity. The timing is set such that the transmitted part of a pulse spectrally interferes with the reflection of the next pulse.

2.4.2 Reference-Free Intraburst Phase Slip Stabilization

While the intraburst phase stabilization as described in Chapter 2.4.1 drastically reduces the drift of the intraburst phase slip, it still has major drawbacks:

- The reference and burst seed pulse train need to share as many optical components as possible, to provide for high stability regarding mechanical vibrations. This imposes strong limitations on the experimental setup design.
- The necessity to additionally couple the reference pulse train into the RA cavity sets strong restrictions on the RA cavity design.
- The common alignment of reference and burst seed is very tedious and the optimal alignment configuration of all optical components is very limited.

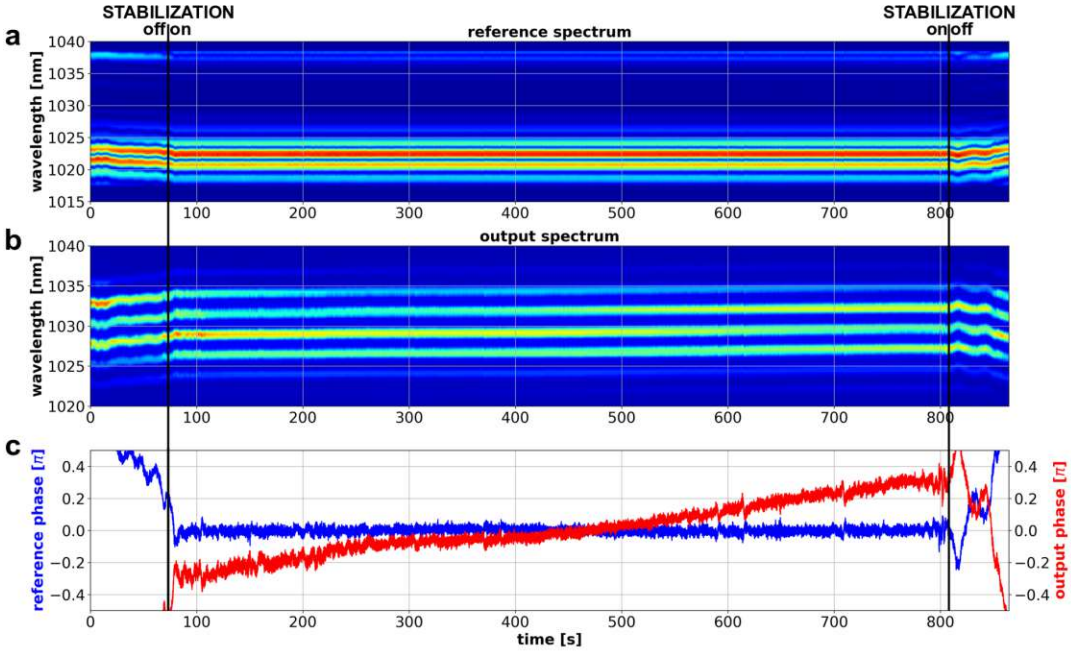

Figure 2.10: Intraburst phase slip stabilization results with a reference pulse. Spectrum over time of a) an interferometric reference (in-loop) b) the output burst ($N = 4$, Δt =3 ps, out-of-loop). c) Phase of the interferometric reference (blue) and the intraburst phase slip (red) over time. The intraburst phase slip stabilization is realized by controlling the cavity length difference with an active feedback loop by applying an interferometric in-loop reference. The reference interference spectrum shows a mitigated bandwidth, because of spectral shaping of the seed pulses for precompensation of gain-narrowing. The stabilization reduces strongly the phase slip drift and thus leads to a stable burst spectrum over an extended time-period.

- During stabilization, the reference signal is stabilized and not directly the burst signal itself (open-loop control). This leads to a residual drift in the intraburst phase slip (See Fig. 2.10).

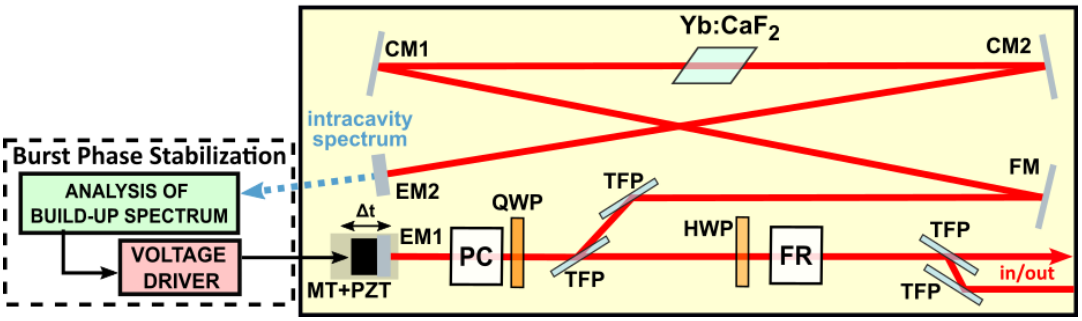

Figure 2.11: Scheme of the reference-free intraburst phase slip stabilization, where by analyzation of the intracavity spectrum (blue), a measure for the intraburst phase slip drift is acquired. **EMx:** End Mirror X. **FM:** Folding mirror. **CMx:** Curved Mirror X. **TFP:** Thin-Film Polarizer. **MT:** Manual Translation Stage. **PZT:** Piezo-electric Translation Stage. **PC:** Pockels Cell. **QWP:** Quarter Waveplate. **HWP:** Half Waveplate.

A drift-free and simpler approach for stabilizing the intraburst phase slip is to avoid the use of a reference pulse train at all and, instead, to rely on the intracavity spectrum of the Vernier RA cavity (Fig. 2.11), which also carries the information of the round-trip detuning between the oscillator and the RA cavity. Fig. 2.11 shows the adapted depiction of a cavity utilizing this approach. For measurement of the intracavity spectrum, the finite transmission of one of the mirrors (e.g. EM2) can be used. The Fourier-transform of the intracavity spectrum shows a maximum at a position that refers to the fundamental intraburst rate, corresponding to the round-trip time detuning (Fig. 2.12). The fundamental maximum arises from spectral interference of the burst pulses in the cavity. Drifts of the phase at this reference point are equal to drifts in the intraburst phase slip [2]. To compensate for any phase variations, the round-trip detuning can be controlled accordingly, with e.g. a piezoelectric transducer (closed-loop control) that sets the position of one of the intracavity mirrors. This method requires no additional reference pulse train, as the one described in Chapter 2.4.1, and thus strongly reduces the constraints set on the RA design. It is applied in the experimental efforts described in chapter 7.

Fig. 2.13 shows the temporal evolution of the spectrum of a burst, showing instability of the interference fringes while runniny freely, caused by the intraburst phase slip drifts. Stable spectra are achieved while the stabilization is turned on. This applies to both, the intracavity spectrum which is taken as a reference, as well as the spectrum of the amplified burst. The intracavity spectrum was measured with a high-resolution spectrometer (OceanOptics HR4000) to optimize the stabilization performance. The resulting pulse-to-pulse phase stabilization is within a mean deviation of 0.0137π from its target value.

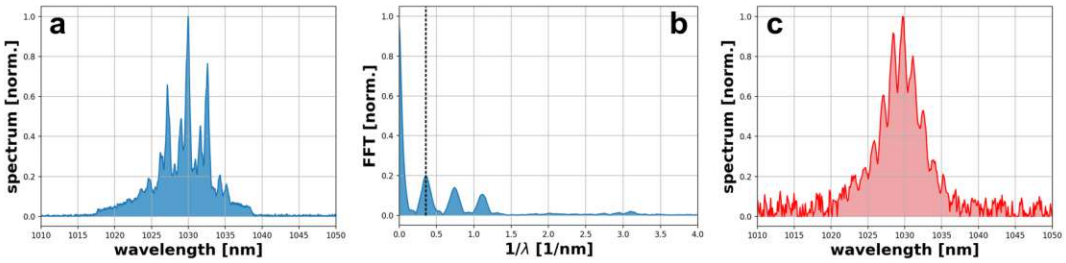

Figure 2.12: Intraburst phase slip stabilization results with the intracavity spectrum as reference. The spectrum a) of the reference buildup signal from the RA cavity. b) of the Fast Fourier Transform (FFT) of the buildup spectrum. c) of the amplified burst. The dashed line marks the position, which corresponds to the fundamental intraburst pulse spacing.

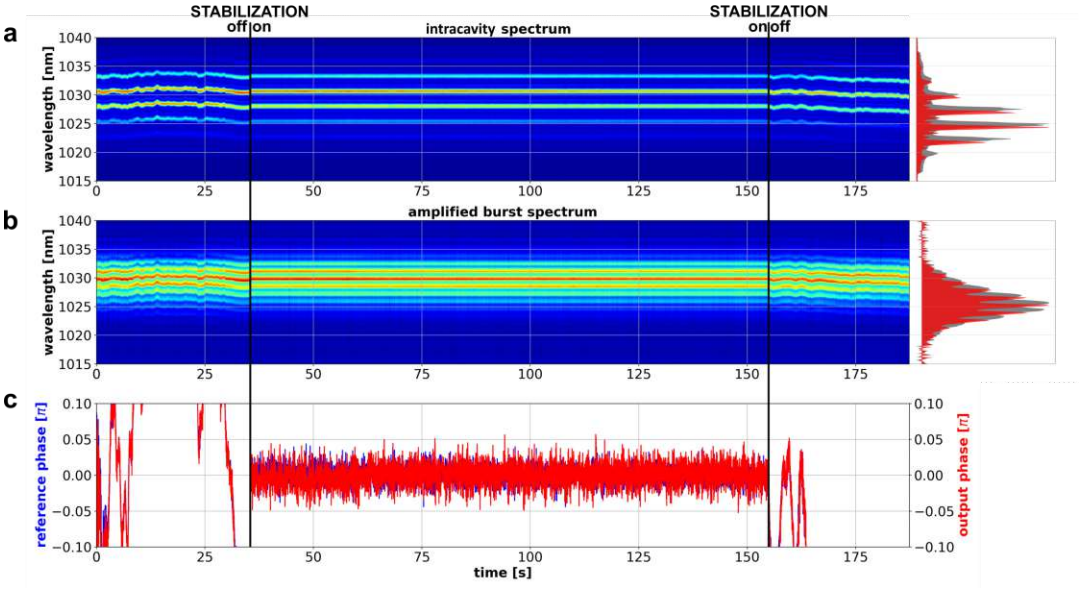

Figure 2.13: Amplified spectrum over time of a) reference buildup b) amplified burst. The on-set/off-set of stabilization is depicted by black lines. The inlay shows a spectrum integrated over 30 seconds, both non-stabilized (grey) and stabilized (red). A high-resolution spectrometer (OceanOptics HR4000) was used for the reference, while for the amplified signal the SHG spectrum was measured with less resolution (OceanOptics USB2000). c) The phase extracted from the reference point, equal to the intraburst phase slip, over time.

Chapter 3

Applications

In this chapter, several applications that are relevant to ultrashort-pulse bursts with intraburst repetition rates larger than a GHz are outlined. An overview of some applications is given in Chapter 3.1. Chapter 3.2 covers a particular application called Burst Stimulated Raman Spectroscopy, which was proposed and investigated theoretically in our group. The generation of intense spectrally-tunable THz radiation by Optical Rectification in a $LiNbO_3$ crystal is demonstrated experimentally (Chapter 3.3) and an outlook of its application is given (Chapter 3.4).

3.1 Overview

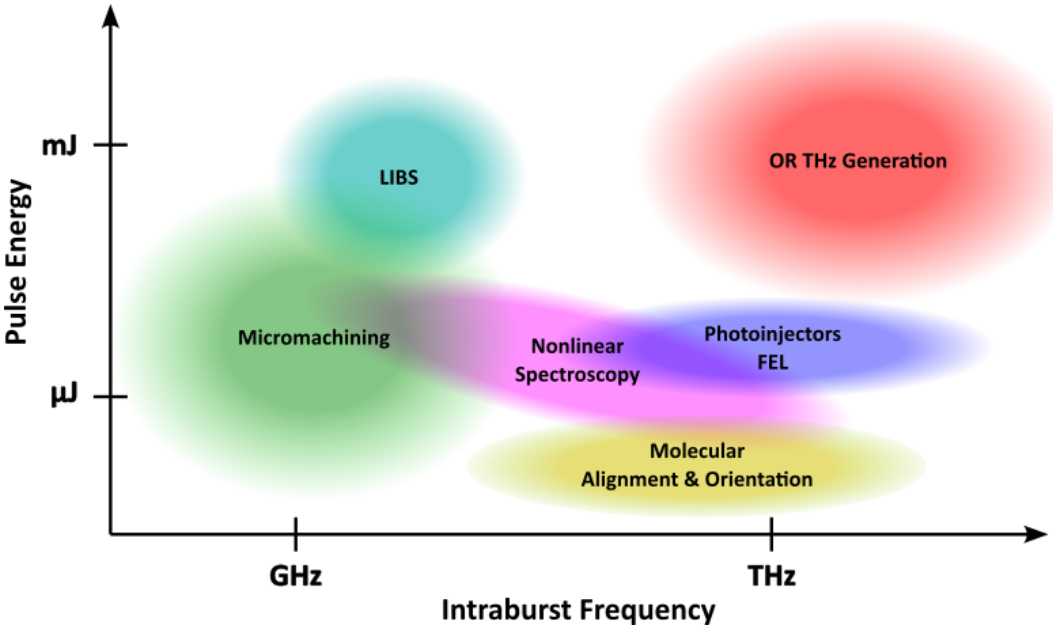

Figure 3.1: Applications for bursts of laser pulses.

Among the applications of ultrashort laser pulses, **micromachining** has the highest projected growth rate of 17.5% [50] and thus takes an increasingly important role in the growing ultrafast laser market, whose size is estimated to be 7.37 billion $ in 2023 and expected to reach 20.04 billion $ in 2030 [51]. One relevant process in the application of ultrashort pulses in micromachining is ablation, which means the direct transition from

a solid material into its gaseous phase. Practically, it describes the material removal without the generation of thermal energy, i.e. heat. This allows precise processing of targets by ultrashort pulses in comparison to nanosecond, or longer, pulses [52–54]. As was demonstrated by Kerse et al. [55], bursts with above-GHz intraburst repetition rates give access to the ablation-cooled regime, where an increased ablated volume per pulse energy and reduced heat-affected zones are observed. For diagnostic purposes in micromachining, Laser-Induced Breakdown Spectroscopy (LIBS) can be used to determine chemical compositions and to monitor the machining process [56]. Multiple pulses with sub-ns spacing have been demonstrated to increase the LIBS signal intensity in comparison to a single pulse [57]. Further, a decrease in ablation threshold and control over material morphologies is achieved when applying the burst format in Pulsed Laser Deposition (PLD) [58].

Molecular dipoles can be induced by strong laser fields, which is done in the **alignment and orientation of molecules** [59]. Hereby, molecular alignment refers to the angle Θ between the molecular axis and a given laboratory axis (e.g. the polarization direction of the driving laser field), and is quantified by $\langle cos(\Theta)\rangle^2$. Molecular orientation includes, for heteronuclear molecules, also the molecular direction and is, followingly, quantified by $\langle cos(\Theta)\rangle$. The interaction potential is

$$U(\Theta, t) = -\frac{1}{4}\Delta\alpha E^2(t) cos^2\Theta, \tag{3.1}$$

with $\Delta\alpha$ being the molecular polarizability anisotropy and $E(t)$ the electric field envelope. For ultrashort pulses, $E(t)$ acts as a δ-kick and induces Raman transitions between molecular rotational states [60]. The kick-like interaction can be characterized by a so-called kick strength

$$P = \Delta\alpha/(4\hbar) \int E^2(t)dt, \tag{3.2}$$

with $\hbar$ being the reduced Planck's constant. By the impulsive excitation of molecules by the kick of a single ultrashort pulse, coherent superpositions of a multitude of molecular rotational states can be excited. However, the kick strength is proportional to the peak intensity of a given single-pulse shape. Thus, it is limited by the onset of ionization at high intensities. This problem can be circumvented by application of a series of N pulses, improving the coherent control over the population of molecular rotational states [61–64], including molecular alignment techniques [60, 65–68]. Further than that, 3D control of alignment could be demonstrated by means of pulse bursts [69, 70].

Generation of THz radiation with tunable intense spectral brightness is provided by large free-electron laser (FEL) facilities. With electric field strengths above 100 kV/cm, facilities provide tunable THz radiation up to 30 THz, such as FLARE at Radboud University, CLIO at University of Paris, TELBE at Helmholtz-Zentrum Dresden, or FLASH in Hamburg [71–75]. Further development of table-top sources are motivated by reduction of costs and highlight the potential of a greater accessibility to a vast majority of research

groups for such kinds of THz sources. A promising table-top alternative is bursts of ultrashort pulses serving as a driver for THz generation, supporting μJ-level THz pulses by Optical Rectification (OR) in either a LiNb crystal within a Tilted-Pulse-Front-Pumping (TPFP) setup, as is demonstrated in Chapter 3.3, or in organic crystals, such as DAST [76]. Further, THz intraburst repetition rates in the NIR allow also for **THz modulation of electron bunches** that are accelerated to relativistic energies, as they are used in FEL facilities for coherent THz radiation generation. Control of the longitudinal modulation of an electron beam can not only suppress coherent radiation, as it may be wanted for the provision of high-quality electron beams. It also enables the bunching of electrons to timescales shorter than a picosecond, which enhances the coherent radiation with a square dependence on the number of electrons in the beam [77].
Overall, burst technologies providing THz intraburst repetition rates not only open up completely new ways to generate THz radiation in table-top systems but are also capable of improving already existing THz generation techniques applied at FELs.

Laser-driven electron accelerators struggle with the problem of mismatch between the velocity of the electron bunch and the laser group velocity [78]. This problem can be met by accelerating an electron bunch coupled to a THz field within a dispersion-matched dielectric waveguide [79]. In a recent publication, cascaded THz-driven acceleration with an increased energy gain of 204 keV has been shown, being one order of magnitude larger as compared to previous results [80]. However, the mentioned approach relies on THz pulse splitting with a setup complexity that does not scale well with an increasing number of stages. The mentioned difficulties limit the interaction length for acceleration to a few millimeters. This has negative effects on the scalability of this type of accelerator without dropping its greatest benefit, which is the potential to downscale accelerator size and costs with much higher possible field gradients compared to existing RF-based accelerators. The mentioned problem is claimed to be solvable by producing long driver pulses that exceed 100 ps [81], but it only provides an efficiency of up to 0.12%. A much higher terahertz generation efficiency of 4.7% is achieved by optical rectification (OR) of sub-ps pulses [82]. With burst-mode sub-ps pulses, the cascaded amplification could be realized without relying on complex pulse splitting and recombination setups. Acceleration with burst-mode sub-ps pulses could thus allow techniques that provide efficiency, as given by ultrashort pulses, together with the highest energy gains, as provided by long pulses, while staying below optical damage thresholds. As will be shown in the course of this thesis (Chapter 3.3), μJ phase-locked bursts of THz radiation can be generated, fulfilling the criteria of laser-driven electron acceleration.

With the advent of ultrashort laser pulses came the rise of **nonlinear spectroscopy** [83] that enabled the direct research of atomic and molecular properties [84], and several phenomena in solids [85]. For most of these applications, a single pulse, or two pulses in the case of time-resolved spectroscopies, provides a short signal of broadband frequencies for which efficient amplification schemes, such as regenerative amplification, are available.

Various phenomena require a high spectral resolution, such as gas detection or the detailed study of rotational-vibrational molecular spectra. However, a high spectral resolution commonly contradicts high temporal intensity. The application of nanosecond OPAs suffers from low nonlinear conversion efficiencies, given their low peak intensities. Alternatively, filtering only a narrow, tunable bandwidth out of a single, broadband pulse would require an enormous energetic loss, especially at high pulse energies. Another approach is the application of a highly stable, infinite train of pulses, also known as frequency comb [29, 86, 87], as outlined in Chapter 2.2.1. For these, various shaping techniques are available, such as fiber-based nonlinear filters [88]. While frequency combs thus combine spectral selectivity with some degree of high intensity provided by their short individual pulse durations, efficient amplification capabilities to high, millijoule pulse energies are limited by their continuous character. This limits the energy reservoir with which one can apply frequency conversion techniques after efficient amplification in the near-infrared (NIR), restricting the spectroscopic application domain. An application that combines a high temporal intensity and narrowband, tunable spectral brightness is spectral focusing, which is based on equalizing the chirps of stretched pulse replicas for difference-frequency generation (DFG) [89–92] or exactly reversing the chirps of input pulses for the generation of a narrowband sum frequency (SFG) [93–95].

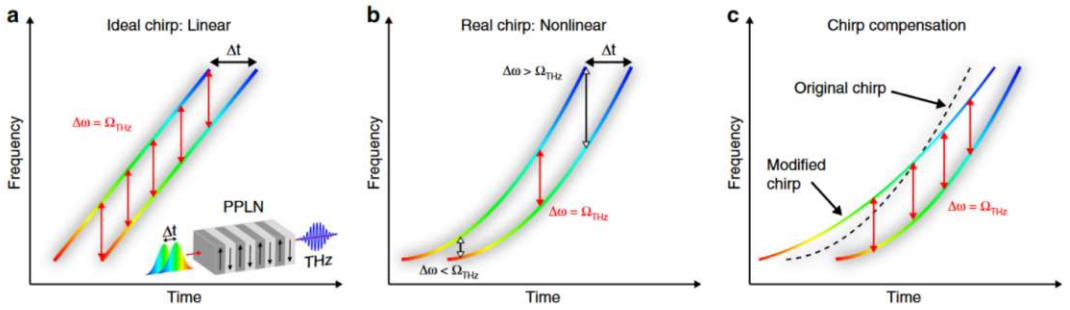

Figure 3.2: Concept of Spectral Focusing utilizing DFG in a PPLN crystal to generate narrowband THz radiation. a) Ideal case where both delayed pulses have exactly the same instantaneous frequencies $\Delta\omega(t)$. b) The real case in which the instantaneous frequency of both pulses can differ. c) Compensation technique to maximize THz generation efficiency. Figure from [92], published by Nature Communications under a CC BY 4.0 license.

In both DFG and SFG cases, the narrowband spectral tuning is achieved by scanning the optical delay [91, 96] between the chirped input pulses. However, it requires the use of slow mechanical delay scanning, preventing the technique's usefulness in high-speed nonlinear imaging applications [97, 98]. The application of chirped pulses also gives certain drawbacks: it requires sophisticated chirp control over a wide bandwidth in order to provide broadband support (See Fig. 3.2) and it is detrimental for several use cases, such as non-dispersive absorption measurements, time-resolved pump-probe, Stimulated Raman Scattering (SRS) [99], Resonantly-Enhanced Multi-Photon Ionization (REMPI) [100] and Infrared Resonant Multi-Photon Dissociation (IRMPD) [101–103].
In contrast to the mentioned techniques, a burst of ultrashort pulses provides a narrow spectral peak structure. Control over the peak structure by tuning the temporal spacing

and/or the intraburst phase slip allows for novel spectroscopic techniques. This approach would be comparable to nanosecond pulses with a tunable wavelength. However, peak intensities are much larger in the case of a fs burst, which leads to much higher conversion efficiencies for nonlinear frequency conversion techniques.

3.2 Burst Stimulated Raman Spectroscopy

Many physical interactions can be summarized as a class of excitations that consist of a certain driving force that is impacting a physical quantity of a system, such as a mechanical force that is imposing the deflection of a spring or an electric field that leads to an electric polarization of a dielectric material. In this sense, an input-to-output relationship is given and a general formulation can be done by the system's response function $g(t)$, which reflects common system properties, such as causality, dynamics and stability [104]. For any system that is sensitive to optical excitation, the response function for linear interactions is represented by the electric susceptibility $\chi(t)$ which mediates the relation between the driving electric field $E(t)$ and the polarization density $P(t)$ [105]

$$P(t) = \epsilon_0 \int_{-\infty}^{+\infty} \chi(t-t')E(t')dt'. \tag{3.3}$$

While there are many ways to model a system by its dielectric susceptibility [106], all physical systems share the property, that their support of the susceptibility in the time domain is limited. For example, a simple model system, the Debye Model, is given by an exponentially decaying function for the electric susceptibility $\chi(t)$ with a $1/e$-time constant τ_e

$$\chi(t) = \begin{cases} \chi_0 \exp\left(-\frac{t}{\tau_e}\right), & \text{if } t \geq 0 \\ 0, & \text{otherwise.} \end{cases} \tag{3.4}$$

In the interaction of a burst with Δt-spaced pulses with matter, the time-constant τ_e of a system thus plays a prominent role. This leads to interesting effects in the case of nonlinear optics, in which multiple photons at various times participate in a fundamental quantum interaction (e.g. two-photon absorption). For burst interactions with time constants much smaller than the pulse spacing, the probability that all photons come from an individual pulse is much higher. Thus, every burst pulse interacts as a single, individual pulse without coupling to neighboring pulses and any resulting field coming from an interaction is again a burst field. This is the case for fast electronic processes such as SFG and DFG. In general, when working with ultrashort-pulse bursts this principle allows for a high degree of versatility that comes with the standard techniques of nonlinear optics, as they are used with a single pulse format (see Chapter 6). For time constants much larger than the pulse spacing, burst pulses become in that way interesting for nonlinear optics, because two-photon (or higher order) interactions can couple multiple pulses by consuming photons from different pulses. This becomes more probable the larger the time constant of the system and can lead to useful new kinds of methods. One method that

can benefit from such an effect is Raman spectroscopy since rovibrational time scales lie in the picosecond range.
In Raman Spectroscopy [107, 108], a driving field ω_p excites a molecule with vibrational mode ω_v which leads to the emission of a signal field ω_s with the relationship

$$\omega_p = \omega_s + \omega_v \tag{3.5a}$$

$$\vec{k_p} = \vec{k}_s + \vec{k}_v. \tag{3.5b}$$

One can drive this process coherently, such that a multitude of emitters generate waves that have a well-defined phase relationship, which is called Stimulated Raman Scattering (SRS) and can provide up to 8 orders of magnitude stronger signals [109–111]. For this, it is needed to provide both the signal and the driving field coherently by the use of pulsed laser sources. The Raman vibration frequency ω_v needs to be scanned to acquire a Raman spectrum, which can be done in several ways [112]. One can do this by using two ps narrowband pulses and tuning at least one of them in its central frequency, also commonly denominated as sequential wavelength tuning. This approach allows for a high spectral resolution down to 5 cm^{-1} [113], but is comparably low in the data acquisition rate because of its scanning nature [114]. A faster technique is to acquire the spectral components in parallel by using a ps pump pulse in combination with a broadband fs signal pulse. However, this leads to a non-ideal overlap in time because both pulses have orders of magnitude different durations [115, 116]. Spectral focusing (Fig. 3.2) is also a useful technique in SRS because one can scan the difference frequency of the two chirped pulses across the vibrational Raman frequency of interest. Still, the problems of dispersion management need to be addressed, which are present when applying a technique based on the application of chirped pulses.

A new proposed approach initiated by our group is Burst-driven Stimulated Raman Scattering (BSRS) [117]. It builds on the application of a signal-idler pair of pulse bursts, where each burst shows a pronounced peak structure (See. Fig. 3.3). If a white-light seeded OPA is driven by a pump burst to generate the burst pair, the signal and the idler burst will have, due to phase conjugation, opposite shifts in their phase-slip offset frequencies [118]. Thus, the frequency difference of every peak pair is given by

$$f_R = \frac{\Delta\phi_s}{\pi\Delta t} + (m-n)f_{burst}, \tag{3.6}$$

where the peak m belongs to the signal pulse, and peak n belongs to the idler pulse. All peak pairs with equal index difference $m-n$ drive in parallel the same Raman frequency. The frequency difference can be scanned across a Raman mode by scanning the intraburst phase slip ϕ_s, which can be done by a fast AOM without any moving parts as will be shown in the next section. The ϕ_s-scan is periodic (See Fig. 3.4) and limited by the Free Spectral Range (FSR) that is given by the intraburst rate f_{burst}, or in wavenumbers as $33.3\ cm^{-1}/\Delta t\ [ps]$. A broader spectral coverage can be attained by tuning the burst pair generating OPA. The spectral resolution is improved by increasing the burst duration

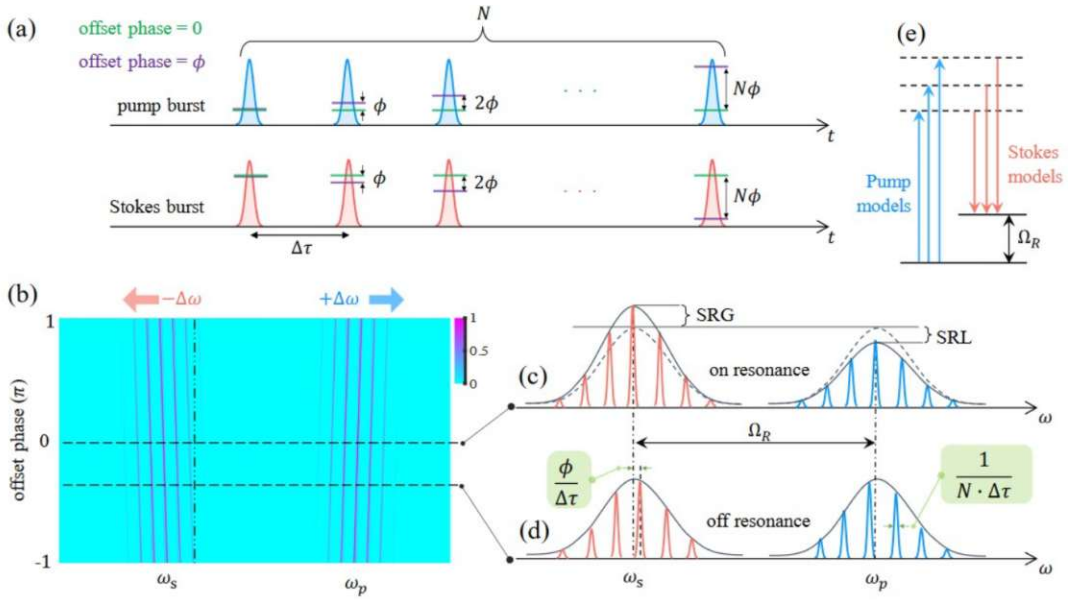

Figure 3.3: Concept of burst-driven Stimulated Raman Scattering (SRS). Figure by Hongtao Hu [117].

$(N-1)\Delta t$, as given in Eq. 1.14, therefore, by increasing either the pulse number N, the pulse spacing Δt, or both. Depending on the case, either the total burst energy can be kept constant (Fig. 3.5a), or the pulse intensity can be kept constant (Fig. 3.5b). The former leads to an increase in resolution with increasing burst duration, but to a decreasing Raman signal because of lower pulse intensities. The latter results in a stronger than linear increase in the SRS signal with increasing pulse number. This indicates the need for a burst system that can scale the burst energy with its pulse number without an increase in temporal intensity (See chapter 7).

3.3 Generation of Terahertz Burst Radiation by Optical Rectification

As mentioned in Chapter 3.1, the generation of THz radiation with tunable intense spectral brightness with table-top systems is a promising application to provide techniques with which novel types of intense THz radiation would be available to larger number of research groups. We performed a proof-of-concept experiment in cooperation with Dr. Jozsef Fülöp's group (ELI Alps) where the feasibility of this application is demonstrated by optical rectification of mJ-amplified pulse bursts generated from an Yb-system in a $LiNbO_3$ crystal. The author notes that parts of this subchapter were already published in a similar form in the author's work [5].

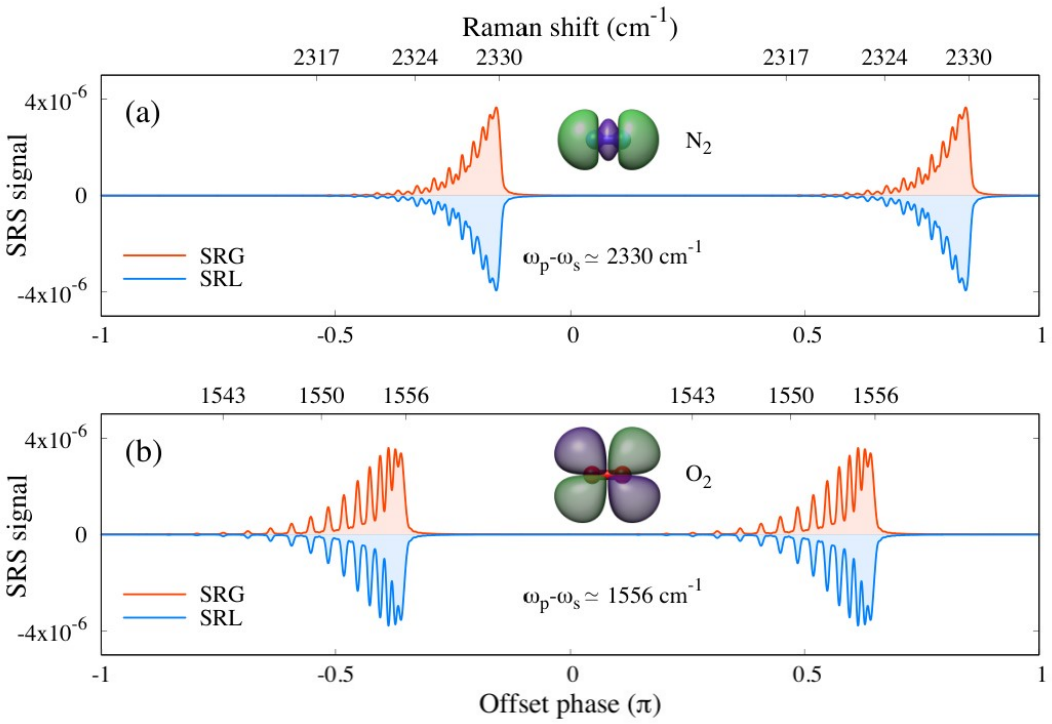

Figure 3.4: Simulated phase-slip scan revealing the SRG and SRL Raman Spectra in burst-driven Stimulated Raman Scattering (SRS) for nitrogen (N_2) at 2330 cm^{-1} (a), and for oxygen (O_2) at 1556 cm^{-1} (b). $N = 100$, $\Delta t = 1$ ps, $I_s/I_p = 0.8$. Calculation and figure by Hongtao Hu [117].

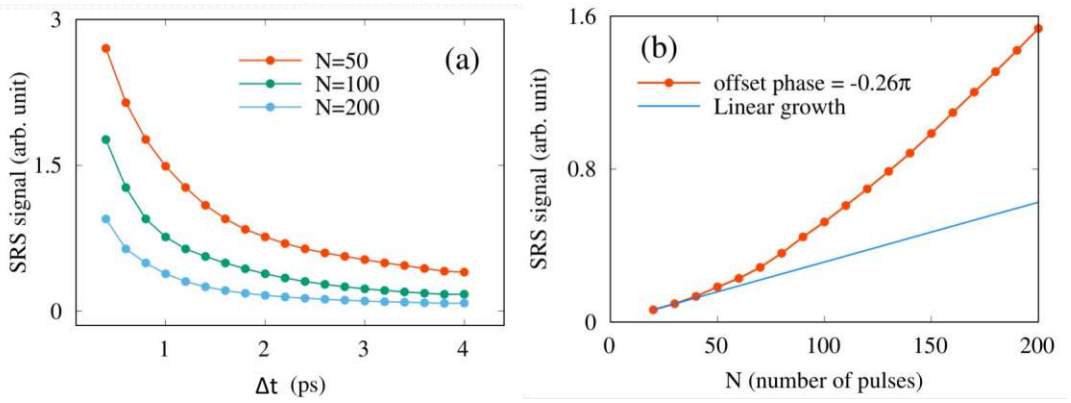

Figure 3.5: Scaling behaviour of the Raman signal in BSRS regarding pulse number N and pulse spacing Δt while keeping a) burst energy constant and b) burst intensity constant. Calculations and figure by Hongtao Hu [117].

3.3.1 Optical Rectification Setup

The tilted-pulse-front-pumping (TPFP) setup (See Fig 3.6) consisted of a grating (1400 lines/mm) for tilting the pulse front and a near-infrared achromatic lens of 250 mm focal length for imaging the grating surface into the prism-shaped $LiNbO_3$ THz generation crystal. The grating-lens distance was 65.6 cm and the lens-crystal distance was 41.5 cm. At the grating, the angle of incidence was 35° and the first-order diffraction angle was 55°. The measured input beam diameter was 3.5 mm at 1/e intensity level. A Michelson interferometer was used to measure the THz pulse spectrum based on the method of Fourier transform spectroscopy. A 4-mm thick Si plate was used as the beam splitter and a pyroelectric detector measured the interferogram signal.

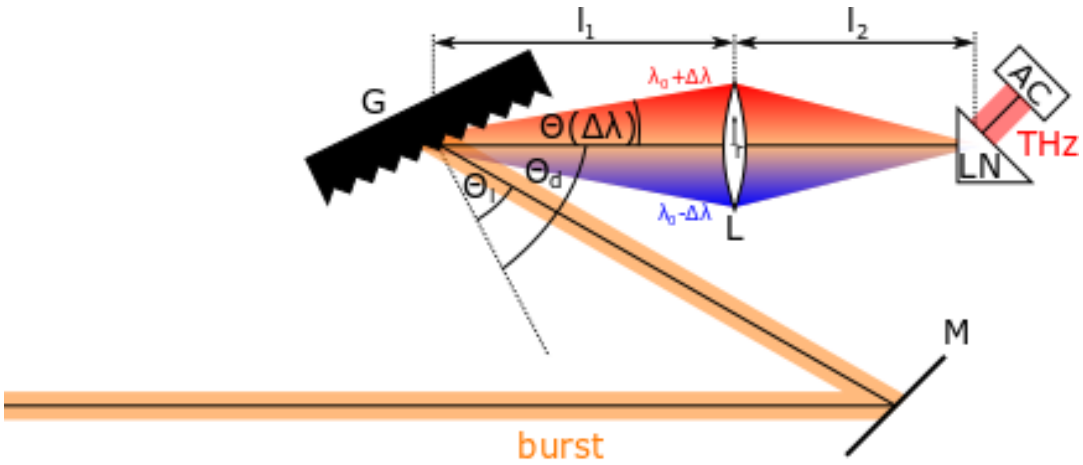

Figure 3.6: Experimental tilted-pulse-front-pumping (TPFP) setup for optical rectification (OR) of mJ NIR bursts in a $LiNbO_3$ crystal. This figure was also used in the author's master thesis [2], however, it is also shown here due to the clarity of the experimental design for the reader.

3.3.2 Results

With NIR bursts of 2.5 mJ, THz burst energies of up to 4 μJ were achieved, thus attaining a conversion efficiency of around 0.16% (see Fig. 3.8). SHG autocorrelations of the NIR burst driver and recorded linear autocorrelations of generated THz transients using a Michelson interferometer together with spectra retrieved by Fourier transformation can be seen in Fig. 3.7. The measurements were performed for variable pulse spacing with fixed pulse number (Fig. 3.7a, $N = 6$) and for variable pulse number with fixed pulse spacing (Fig. 3.7b, $\Delta t = 3$ ps). As expected, the continuously-tunable intraburst repetition rate is determined by the inverse pulse spacing $1/\Delta t$, translating into the lowest-order THz frequency, whereas the bandwidth Δf of the generated THz peak scales inversely to the product of pulse number and spacing $1/(N \cdot \Delta t)$, with values $\Delta f_{N=2} = 138$ GHz, $\Delta f_{N=4} = 58$ GHz, $\Delta f_{N=6} = 50$ GHz. The spectra exhibit a high spectral contrast that progressively improves with N. Higher harmonics of the THz-signal are observed as well, following the Fourier transformation of a windowed pulse train. The THz pulse source

demonstrated here offers a unique combination of versatile pulse shaping capability and scalability to high energies, thereby surpassing many other methods.

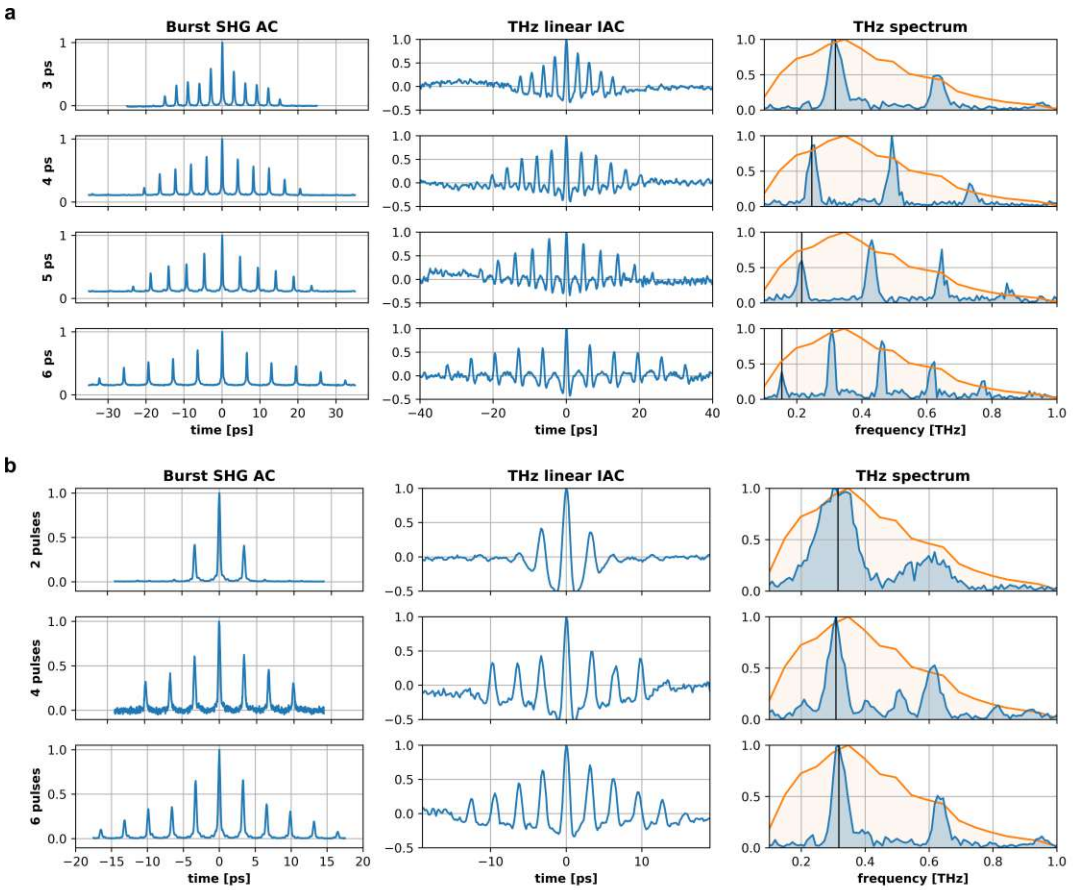

Figure 3.7: Demonstration of control over THz intraburst repetition rates by the generation of continuously-tunable narrowband THz-pulse bursts. Bursts of THz pulses are generated by driving a LiNb03 crystal with the NIR bursts. Second-harmonic autocorrelations of the NIR bursts (left) and linear interferometric autocorrelations from the THz-pulse bursts (middle) were measured. Harmonic THz spectra (right) were retrieved from the latter by Fourier transformation which are shown (blue) in comparison to the spectrum of a single THz pulse (orange). a) Continuously tunable THz frequencies can be seen when varying the intraburst pulse spacing with a constant number of N=6 pulses. b) Controllable bandwidths of the THz peaks can be seen when varying the number of pulses with a constant intraburst pulse spacing Δt of 3 ps. Black vertical lines in the THz spectra indicate the intraburst repetition rates.

The measured THz-pulse burst energies and corresponding conversion efficiencies are shown in Fig. 3.8 for bursts with N = 2, 4, and 6 pulses, in comparison to the single-pulse case. For a given full burst pump energy, the peak intensity for one pulse decreases with increasing N, the number of intraburst pulses. In consequence, because of the nonlinearity of the THz generation process, the energy and the conversion efficiency of the THz pulses decrease with the increasing N. For N = 2, 4, and 6 the efficiency of optical rectification reduces to about 73%, 60%, and 54% of the single-pulse case.

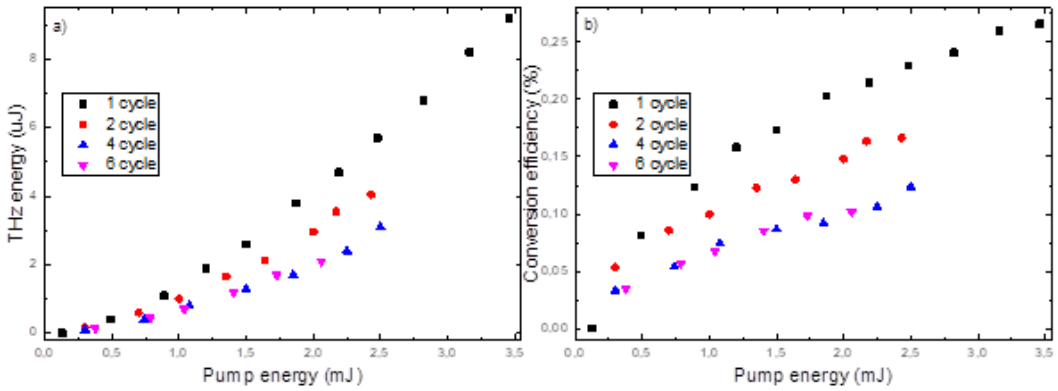

Figure 3.8: a) Measured THz energy (a) and conversion efficiency (b) vs NIR pump energy for various intraburst pulse numbers (cycles) achieved in the TPFP-OR THz generation experiment.

3.4 Outlook on High-Intensity THz Applications

3.4.1 Signal Enhancement in Linear Absorption Spectroscopy

Linear absorption spectroscopy [119] is a widely applicable technique, whose limitation is given when molecular cross-sections may either be low or the abundance of the sample is not given, such as in medical diagnosis. For this reason, signal enhancement techniques have been developed. One example is the application of resonant cavities in which the signal enhancement is based on the Purcell effect, in order to overcome this limitation [120]. The Purcell effect [121] explains the enhancement of spontaneous emission via the photonic mode density which is in resonance with the transition. In a cavity, this enhancement is described by

$$F_P = \frac{3}{4\pi^2}(\frac{\lambda_{free}}{n})^3(\frac{Q}{V}) \tag{3.7}$$

where λ_{free} is the wavelength of the free radiation, Q is the Q-factor of the cavity and V is the cavity volume. In linear absorption spectroscopy, this effect is utilized in cavity-enhanced experiments [122]: Since single photon absorption is the time-reversed version of spontaneous emission, the Purcell effect also acts on absorption cross-sections. Compared to a free sample, a sample in a resonant high-Q cavity experiences an increased absorption cross-section, enabling measurements with drastically increased sensitivity.
In a resonant cavity, a pulse circulates in such a way that it interacts with the sample at a repetition rate which corresponds to a relevant transition. The enhancement can be quantified with the Q-factor which can be described as the cavity mode width relative to the mode frequency (See Fig. 3.9). The application of burst pulses could be equivalent to the cavity enhancement effect. When applying a resonant pulse burst, the pulse spacing is set such that the intraburst repetition rate resonates with the energy of a relevant transition. The equivalence of the proposed burst-enhancement technique to cavity-enhancement can be underlined by considering Fig. 3.9, in which the transmission function of a Fabry-Perot interferometer with various values of mirror reflectivity R (and thus, Q-factor) can be seen. The burst spectral peaks, which are based on spectral interference of the burst pulses, can be perceived as equivalent to cavity modes, which are based on spectral interference of intracavity partial waves formed by reflection at the cavity end mirrors.

3.4.2 Multi-Photon Effects in Cavities

A THz source as realized above, combines high energy with high spectral brightness without giving up on high temporal intensity. This gives the potential to exploit the nonlinear regime, which is where modifications of a sample under investigation may be given by the driving pulses, and high-field effects can be investigated. Of particular interest could be multi-photon effects in cavities which can be induced by the novel THz sources. As mentioned before, the photonic mode density of a cavity can affect a sample, such as on absorption cross-sections. However, in a regime where matter is still only weakly coupled to the cavity, absorption lines only change slightly in frequency besides their

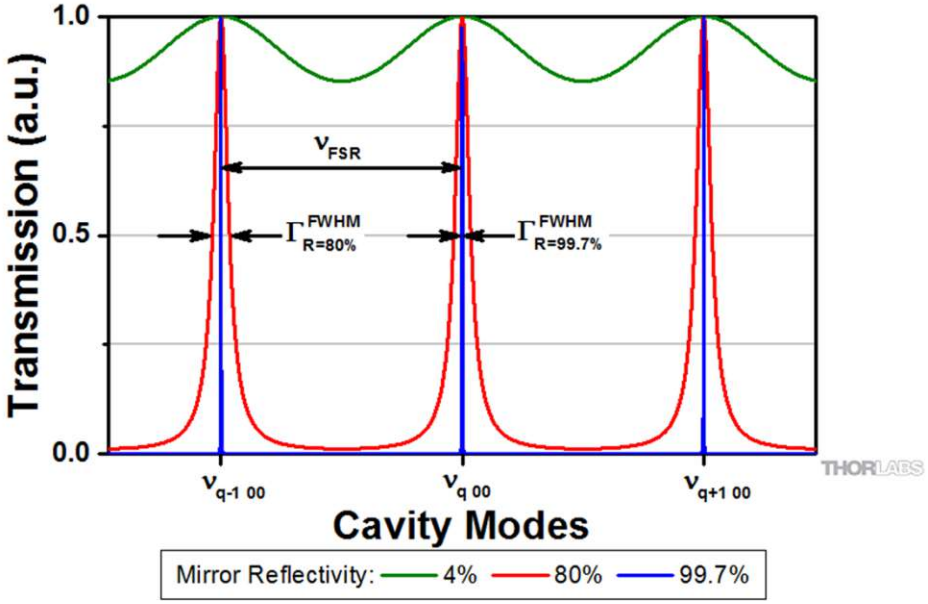

Figure 3.9: Transmission function of a Fabry-Perot interferometer with various values of mirror reflectivity. Figure from [123].

change in signal intensity by enhancement effects. The situation is different when the matter excitation is strongly coupled to a resonant photonic mode. Quantitatively, the strength of the interaction is given by the Rabi frequency

$$\Omega_R = d \cdot E \tag{3.8}$$

with d being the dipole moment of the transition and E the electric field, given by

$$E = E_{vac} \cdot \sqrt{n_{ph} + 1} \tag{3.9a}$$

$$= \sqrt{\frac{\hbar\omega}{2\epsilon_0 V}} \cdot \sqrt{n_{ph} + 1} \tag{3.9b}$$

with E_{vac} being the vacuum field and n_{ph} the photon number. For a number of N particles coupling to the field, the Rabi frequency is given by

$$\Omega_R = d\sqrt{N}E. \tag{3.10}$$

Regarding the absorption spectrum of the combined sample-cavity system, the resonant line is split into two lines, which in the case $n_{ph} = 0$ is known as vacuum Rabi splitting [120]. The separation of those two lines is given by the Rabi frequency, which can be controlled by

- the cavity volume V, i.e. the separation of cavity mirrors
- the number of photons n_{ph}, i.e. the intensity of pump radiation
- the number of particles N

The effect of particle number can be compared when looking at Refs. [124] and [125], in which both the absorption spectrum of α-Lactose is measured in a cavity. In [124], a nanometer-thin layer with a very small number of molecules is investigated, leading to a coupling between matter and cavity in the weak coupling regime. The absorption signal is strongly enhanced by the cavity, and also slightly shifted with the change of optical path length by the sample layer, however, the signal still consists of a signal peak. However in [125], compressed pellets of α-Lactose with an estimated concentration of $2.6 \cdot 10^{21}$ cm^{-3} are used as a sample, which leads to strong coupling because of the high molecular density. In particular, since OR THz burst sources allow for extremely high energy and spectral brightness, investigation of the transition of the weak-coupling regime to the strong-coupling regime by resonantly exciting a strongly-coupled sample-cavity system would be possible. Further, it is expected that such sources are capable of entering the strong coupling regime at much lower particle concentrations compared to the application of single pulses. This would allow the control of molecular transitions not only in highly dense samples.

Polaritons, which are given by a mixed wavefunction of light and matter, formed in the strong coupling regime in microcavities, can be investigated by multi-photon effects. In [126], second harmonic generation (SHG) and two-photon absorption (TPA) are proposed together with a detailed model and calculations (See Fig. 3.10). In this case, the cavity would have a fundamental mode ω_1 and its harmonic mode ω_2. A matter excitation, such as an exciton, may have a resonance frequency that is at or near the harmonic frequency. To excite polaritonic states via nonlinear processes, two photons at frequency ω_1 can be converted either into a harmonic photon in the cavity and vice versa (SHG), whereas for TPA two photons can be converted to a matter excitation at the harmonic frequency. The numerical calculations in [126] give the internal intensity parameter Ω and the second harmonic intensity I_{SH} depending on the frequency of a CW pump, which is detuned by a frequency $\delta\omega$ from the fundamental mode. It is shown that there is a clear intensity dependence of the spectra. Generally, OR THz burst sources allow for experimental investigation of nonlinear optical effects in microcavities. For this, the transmitted terahertz signal for energetic, spectrally intense terahertz pumps can be measured. Additionally, the response of such a system to a weak probe pulse, which optionally can also be chirped, is also of high interest. Such a probe pulse can determine the polaritonic absorption near ω_2. At high pump intensities, it is pointed out in [126], that hyper-Raman scattering could be performed in such a system, leading to a parametric gain of the probe signal.

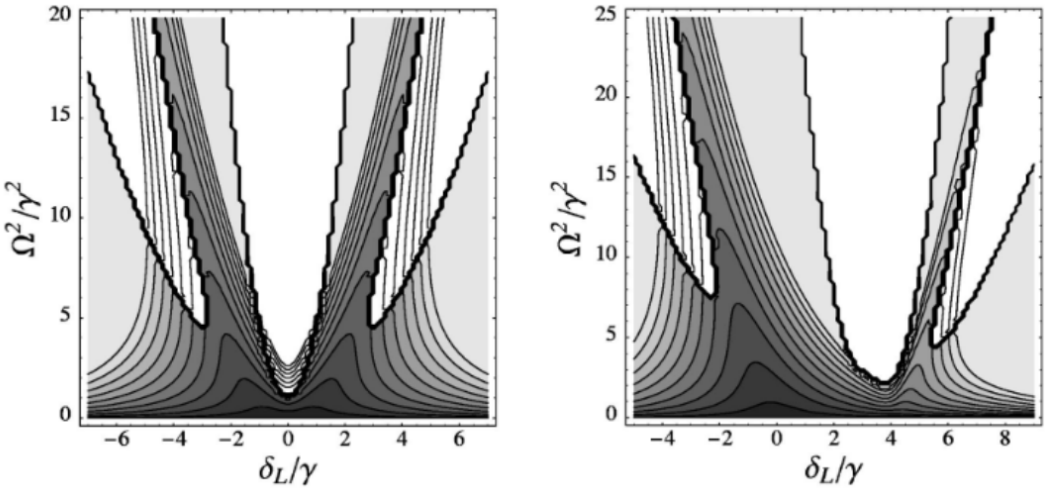

Figure 3.10: (left) Internal intensity parameter (proportional to the internal as well as to the transmitted intensity) (right) Second harmonic intensity spectra, both for different values of (constant) incident intensity as a function of the detuning of the incident field frequency relative to ω_1. The grey scale corresponds to the incident intensity: lighter shadowing means higher intensity; white regions correspond to unstable behavior. Figure taken with permission from [126]

Chapter 4

Buildup of an Improved Vernier System

Originally, a system was used in our lab, which was built on the phase-slip stabilization approach with a separate reference pulse train derived from the master oscillator (Chapter 2.4). This system was used for the measurements whose results are presented in Chapters 3.3 and 5. It is described in further detail in [2]. However, this system had several drawbacks in its operation:

- Its setup size is comparably large (60x120 cm) which leads to thermo-mechanic instability and inefficient use of the setup table space, leaving less space for experimental setups. It also makes a cover of the whole setup unnecessarily expensive, which would have been needed to perform further experiments without noise induced by air turbulences in the lab.
- The pump yield is low, using only one diode bar with a pump diode that contains two diode bars, with only single-pass pumping of the crystal.
- Limited temporal burst characterization: SHG autocorrelation measurements suffer from several ambiguities that inhibit the derivation from the actual temporal intensity of the field under study. One of these ambiguities is time delay inversion symmetry. Thus, such a type of measurement does not give direct access to individual burst pulse energies.

These aspects led to the decision, that further development of the Vernier-type burst technology requires the buildup of an improved system. In the following, it is explained, how this buildup was planned and implemented. An overview of the system is given in Chapter 4.1. The setup of the AOM, including its electronic driver, is described in Chapter 4.2. Finally, the buildup of the Twin RA, including two cavities for regenerative amplification, is covered in Chapter 4.3. The new system was used for the measurements reported in Chapters 6 and 7. The author notes that parts of this chapter were already published in a similar form in the author's work [1, 127].

4.1 System Overview

An overview of the improved Vernier system can be seen in Fig. 4.1. A MHz-repetition-rate mode-locked oscillator (**OSC**, Light-Conversion FLINT, 1030 nm Yb:KGW, 76 MHz repetition rate, 80 fs pulse duration) generates nanojoule pulses. The oscillator pulses are stretched to around 300 ps by a double-pass grating stretcher (**STR**). An acoustic-optical modulator (**AOM**) (TeO_2, 370 MHz, 10 ns rise/fall time, diffraction efficiency $\approx$ 80%) works as a pulse picker by diffracting seed pulses that can be individually modulated in amplitude and phase. Amplification takes place at a repetition rate of 1 kHz in a CW-pumped twin regenerative amplifier (**Twin RA**, Yb:CaF_2) with two cavities. Building a twin RA with two cavities has several advantages for the intended use cases: It allows that in one cavity the AOM-diffracted pulses are accumulated to an ultrashort-pulse burst and amplified consequently. In the other cavity, a single non-diffracted pulse is amplified as a reference for cross-correlation measurements, to perform direct time-domain characterization of the burst pulses. For future purposes, the second cavity could also be used to generate a second burst in parallel and to experiment with the system as a dual burst source. Burst generation requires that the round-trip time of the burst cavity is comparable to the oscillator round-trip time, such that their absolute difference gives the intraburst pulse spacing (Vernier effect). Both cavities are seeded by the same oscillator, thus, the burst and the reference pulse are synchronized to each other. The Twin RA design is such, that it could provide in theory up to 1.5 mJ of pulse or burst energy. However, operating the system in test runs with pulse energies much larger than 100 μJ, led to optical damages in the AOM due to back reflections, because of the limited contrast of the applied optical isolation. Therefore, Twin RA maximum energy is kept at 100 μJ to guarantee the safe operation of the system. If further amplification is required, the system includes a dual-pumped cryogenically-cooled **booster RA** (Yb:CaF_2), which is specified for up to 10 mJ of pulse or burst energy. The **Compressor**, containing a single large 130x20 mm^2 transmission diffraction grating (Gitterwerk), compresses both cavity channels to 250 fs with beams being spatially separated inside the compressor.
The oscillator, booster RA and stretcher were taken without changes from the old system, while the AOM setup, the Twin RA and the compressor needed to be built up completely new.

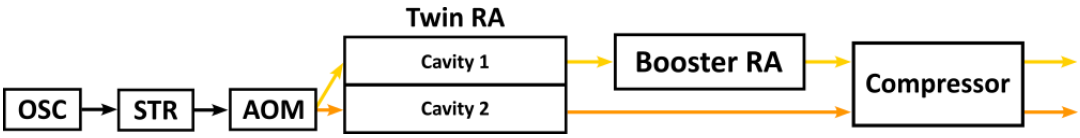

Figure 4.1: Overview of the new Vernier Burst System.

For the implementation of the system, the size constraints of the laser table also needed to be considered. The laser table provides an area of 360x120 cm, for which as few as possible needs to be used for the Vernier burst system, such that enough space is left for experiments. In Fig. 4.2, a schematic shows how the placement was designed such that the table space is utilized efficiently, including the area consumption for each part of

the system. In between each sub-system, there is always some space left for mirrors, and diagnostic devices (spectrometer, powermeter,...), such that the system can be maintained properly without the need to make any unnecessary changes. It was possible to build up the full system while leaving an experimental area of 230x120 cm. Finally, the whole system was covered by a thin steel plate to avoid air turbulences and for optimal heat performance (Fig. 4.3).

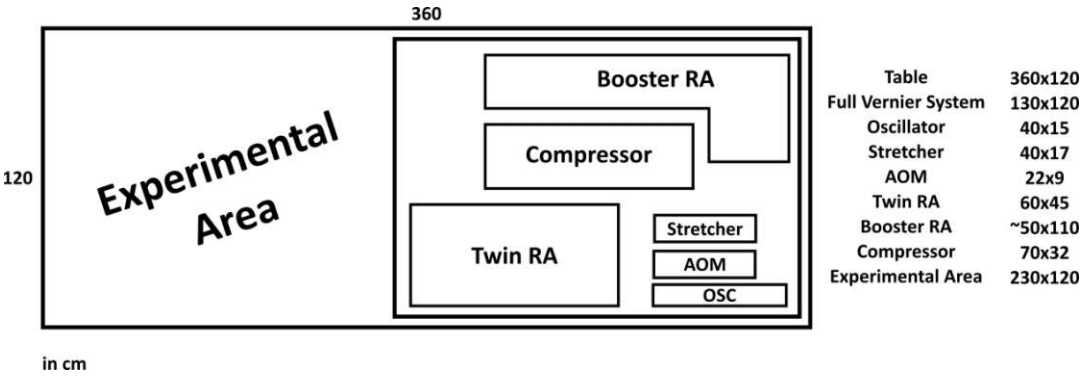

Figure 4.2: Design of the placement on the laser table.

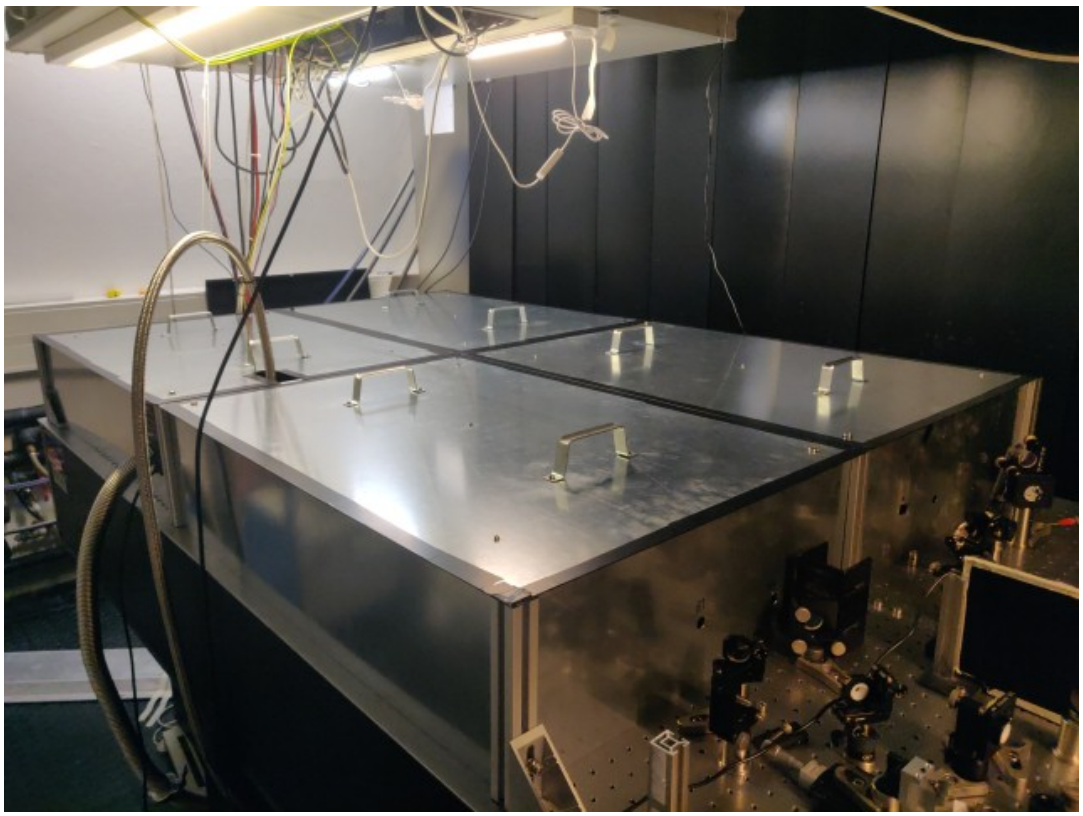

Figure 4.3: The realized Dual Vernier Burst system with a thin steel plate cover.

4.2 AOM Setup

The schematic of the AOM driver setup is shown in Fig. 4.4. Its main part is a Direct-Digital Synthesis (DDS) card, which translates binary-encoded amplitudes and phases from registers into analog RF signals. The maximum output power of the DDS card is too low (660 mVpp, 0 dBm) for the AOM, which requires 30-36 dBm to diffract efficiently. For this, an RF amplifier operating at 370 MHz (which has been determined to be the optimum frequency) with a sufficient gain is needed. The Minicircuits ZHL-5W-202-S+ was chosen for this task, which offers a sufficient gain (+ 50 dB), a wide bandwidth (up to 2 GHz) and is self-protected from excessive drive, heat and reverse polarity, and withstands short and open circuit at the output, as can happen by unintentional misuse in a day-to-day laboratory setup. Since the RF gain is too high for the AOM, the DDS signal is attenuated by 12 dB prior to amplification. Also, a 400 MHz low-pass filter is applied to the DDS output to reduce spurious signals with frequencies above 400 MHz. The registers are programmed with a personal computer which is connected via USB to the DDS card. The DDS card is synchronized to the laser amplification cycle by a kHz trigger, provided by a timing card which also controls the Pockels Cell on/off timings. Both, the timing card and the DDS card contain Phase-Locked Loops (PLL) fed by the 76 MHz trigger coming from the oscillator.

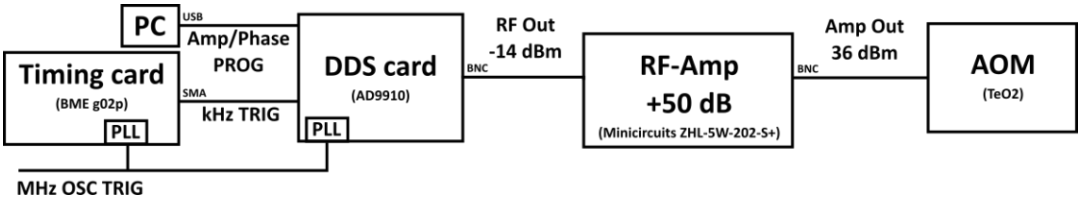

Figure 4.4: Schematic of the AOM electronic driver.

Since the AOM is polarization sensitive, a half waveplate is placed before the AOM at the setup on the optical table (Fig. 4.5). The oscillator beam is focused in the AOM to a diameter of about 100 μm for optimal efficiency by a +35 mm lens. The diffracted and non-diffracted beams are then recollimated by another +35 mm lens and directed towards the RA setup. With the given parameters, a diffraction efficiency of about 80% can be achieved.

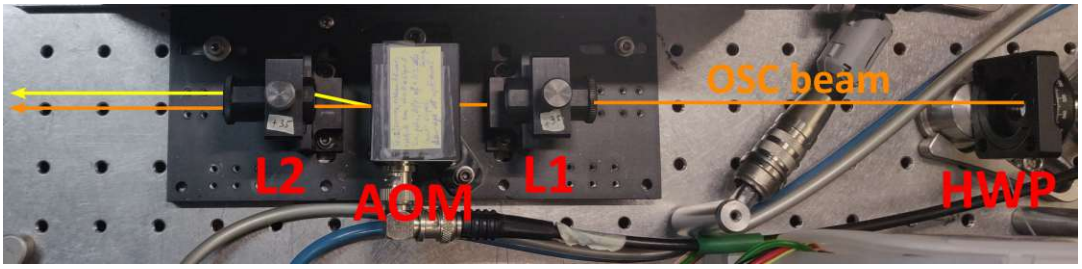

Figure 4.5: The AOM setup on the optical table. **HWP:** Half Waveplate. **L1/L2:** +35 mm lenses.

4.3 Twin RA setup

4.3.1 Cavity Design

A depiction of the cavity design can be seen in Fig. 2.11 and the realization of the amplifier in Fig 4.6. Again, Yb:CaF_2 was used as a crystal since it has a long luminescent lifetime ($\approx$ 2.5 ms) which makes it highly useful for strong amplification at kHz repetition rates [128]. Further, with its negative thermo-optic coefficient (-12 ppm/K at 273 K) that is counteracted by thermal expansion and bulging of the crystal's facets, thermal lensing effects are negligible in the cavity design at the relevant pumping rates used [129]. Since the amplifier is used for Vernier burst generation, the round-trip time needs to be near 13.2 ns set by the 76 MHz oscillator repetition rate. The corresponding round-trip length is 3.96 m. To accommodate such a comparably long cavity on a minimal table size, the cavity is concipated with an x-shaped design. It includes a manual translation stage to set the coarse round-trip time and a guided piezo-electric translation stage (Piezojena PU-40) to set the fine round-trip time electronically. Both end mirrors are flat, allowing the use of one translation stage on each end mirror. However, the final realization ended up applying both translation stages to the EM1 side, because the backside of EM2 was the most useful position to measure the intracavity spectrum.
The RA is optically isolated from the MO by a combination of polarizers, waveplate and Faraday rotator for suppression of amplified pulses coupling back into the MO. Seed pulses couple in and out at a thin-film polarizer (TFP) which is next to the optical switch (combination of Pockels Cell and Quarter Waveplate). Calculations of the laser mode inside the cavity have been performed with the software reZonator (See Fig. 4.7). It was made sure, that the cavity mode is collimated at the end mirror positions, such that a translation of the end mirrors had no measurable impact on the mode parameters at the crystal (beam radius at the crystal $\approx$ 120 μm). As for the old cavity, two TFPs are used to set the polarization and, further, by using a Brewster-cut crystal for further suppression of depolarization in the cavity. The crystal is dual-pumped increasing the pump yield compared to the older system.

4.3.2 Pumping and thermal considerations

The pumping setup can be seen in Fig. 4.8. A 976 nm two-bar CW pump diode (nLight Pearl) is used. Directly at its output, a pump-protection filter is mounted to prevent scattered laser light at 1030 nm reaching back into the diode, while transmitting the pump light at 976 nm. A combination of cylindrical lenses (-50 mm, +150 mm) separates sufficiently the light from the two diode bars in the vertical direction, such that one bar can be used for each cavity. For each cavity, the pump light is guided by a pair of high-reflecting prism-shaped mirrors. The pump light is focused into the crystal by a +60 mm lens with a 2 mm hole in the center for transmission of the cavity mode. Two passes are applied in the crystal in a retroreflecting configuration, where the back-reflected light is separated by a vertical angle from the incoming beam. The transmitted light after the second pass is absorbed in a water-cooled beam dump under reflection on a thin-film

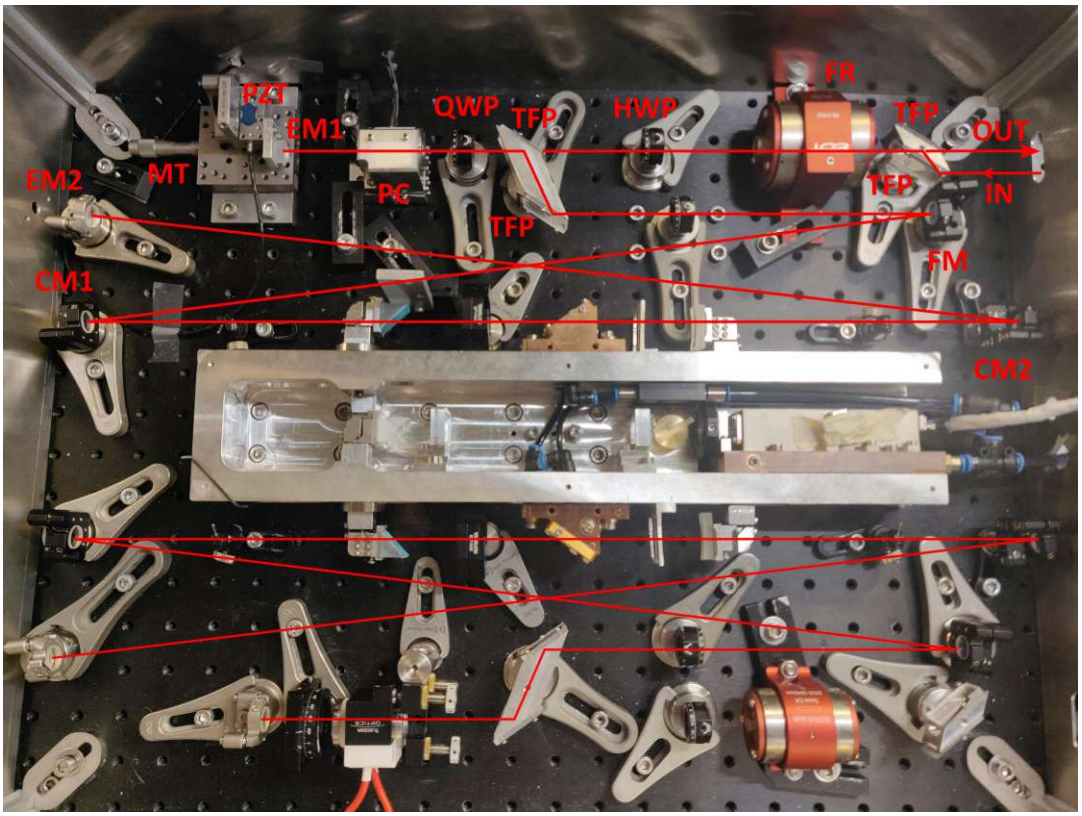

Figure 4.6: Photo of the Twin RA setup. **EMx:** End Mirror X. **FM:** Folding mirror. **CMx:** Curved Mirror X. **TFP:** Thin-Film Polarizer. **MT:** Manual Translation Stage. **PZT:** Piezo-electric Translation Stage. **PC:** Pockels Cell. **QWP:** Quarter Waveplate

	Typ	Label	Parameters	Title
1		EM1		
2		d1	L = 535 mm	
3		M2	R = 500 mm, α = 10°	
4		d2	L = 255 mm	
5		XTAL	L = 5 mm, n0 = 1.43, n_{2T} = 0 m^{-2}, n_{2S} = 0 m^{-2}	
6		d3	L = 274 mm	
7		M3	R = 500 mm, α = 10°	
8		d4	L = 791 mm	
9		BBO	L = 20 mm, n = 1.6155	
10		d5	L = 65 mm	
11		EM2		

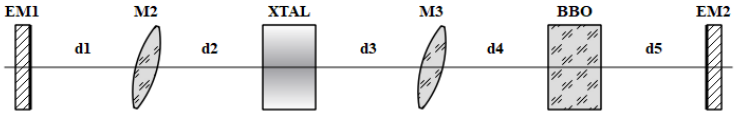

(a) A depiction of the cavity as given by the software reZonator, including the cavity parameters that are taken for the calculations.

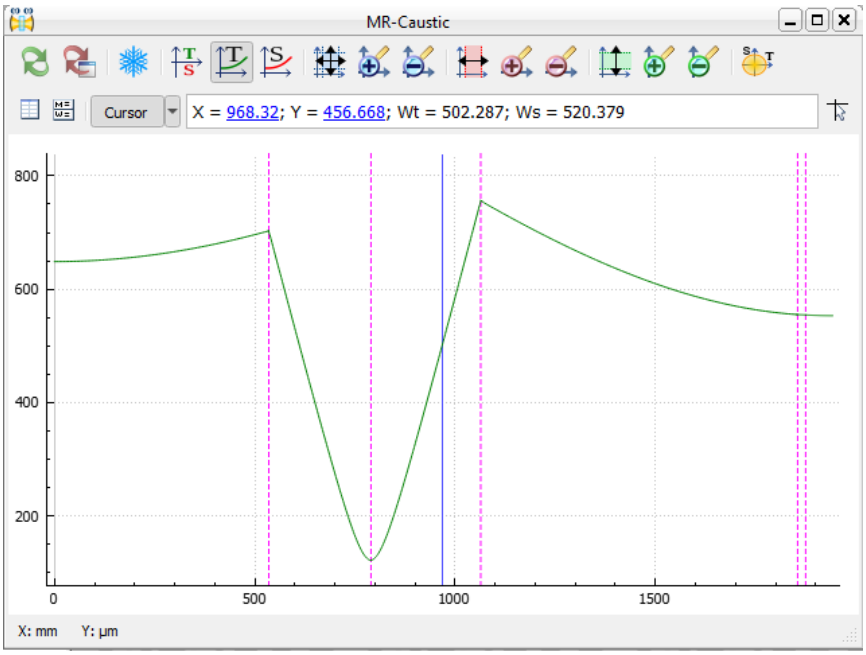

(b) Beam Radius (vertical axis) depending on the cavity position (horizontal axis) as evaluated by the program.

Figure 4.7: Cavity design using the software reZonator.

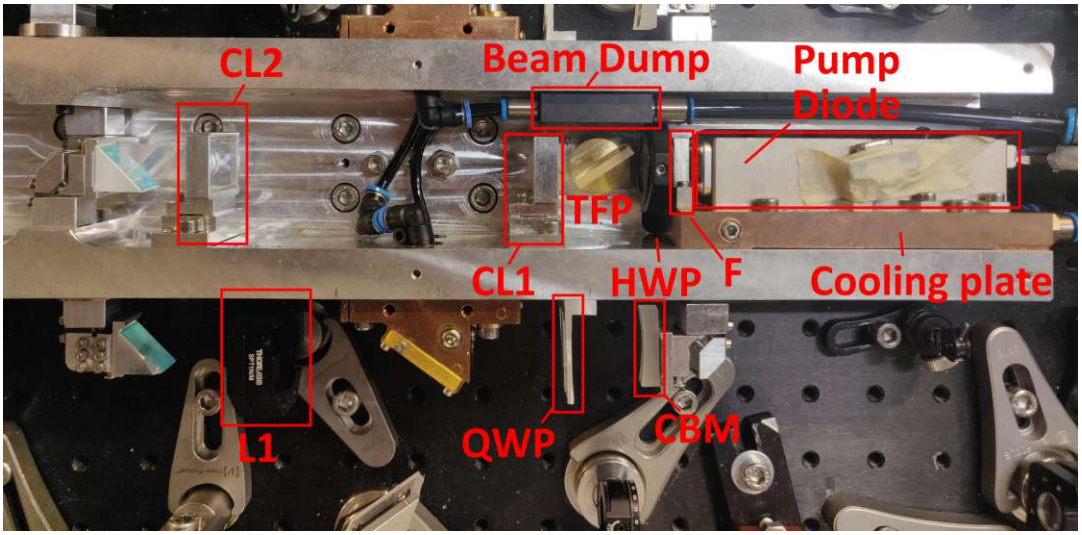

Figure 4.8: Photo of the pump setup. **TFP:** Thin-Film Polarizer. **QWP:** Quarter Waveplate. **CL1:** -50 mm cylindrical lens. **CL2:** +150 mm cylindrical lens. **F:** Pump-protection Filter (HR 1030 nm, AR 976 nm). **L1:** +60 mm lens with 2 mm hole. **CBM:** Curved back-reflecting mirror.

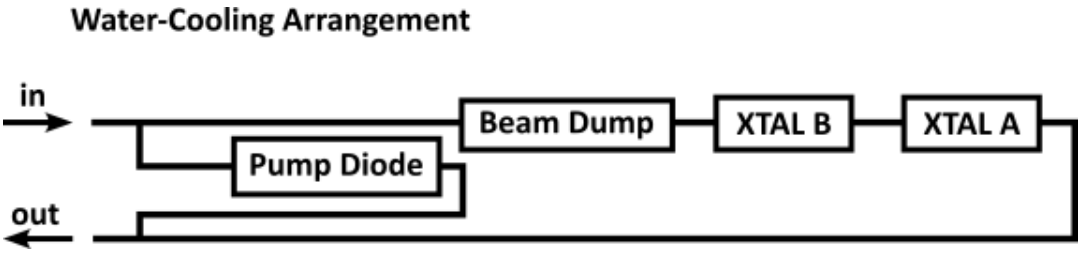

Figure 4.9: Water-cooling arrangement of the Twin RA.

polarizer. Regarding the water-cooling arrangement (Fig. 4.9), the pump diode and the beam dump require the most removal of heat, thus they are connected in parallel to the chiller. The crystal holders are connected in series to the beam dump.

4.3.3 CW characterization

After the buildup of the twin RA, its continuous-wave (CW) operation was characterized to verify its proper operation and efficiency. The CW output power $P_{cw,out}$ was measured depending on the total pump power $P_{abs,tot}$ that was absorbed in the crystal, with the results shown in Fig. 4.10a. Another relevant quantity is the relative absorbed pump power in the first pass $P^{(1)}_{abs,rel}$, defined by

$$P^{(1)}_{abs,rel} = \frac{P^{(1)}_{abs}}{P^{(0)}_{pump}} = \frac{P^{(1)}_{pump} - P^{(0)}_{pump}}{P^{(0)}_{pump}}, \tag{4.1}$$

with $P^{(1)}_{abs}$ being the total pump power absorbed in the first pass, which was derived by measuring the difference between the pump power after the crystal $P^{(1)}_{pump}$ and the incoming pump power $P^{(0)}_{pump}$. The results regarding the relative absorbed pump power are shown in Fig. 4.10b. Because of tight spatial constraints, the pump beam was directed outward by a mirror such that it could be measured by a power meter head. Since the second pass is retroreflecting and neglecting changes in inversion, the same relative absorption was assumed for the second pass to estimate the absorbed pump power of both passes.
The relative absorption was seen to be higher at lower pump rates, while it was lower at higher pump rates. It was also higher for the crystal in cavity A as compared to the one in cavity B (Fig. 4.10b). In Fig. 4.10a, both cavities can be seen to be similar in their CW output at their threshold below $\approx$ 15 W of absorbed pump power. Differences between the two crystals can be explained by several reasons, such as doping variations and cooling conditions (e.g. thermal contact to the crystal holder and the crystals are cooled in series). Above the threshold region up until $\approx$ 30 W, both cavities show an approximate linear behavior, with cavity B showing a higher slope efficiency (53.7 %) than cavity A (35.6 %). At high absorbed pump powers ($>$ 30 W), it can be seen that the relative absorbed pump power saturates, indicating photobleaching, i.e. saturation of the crystal inversion.

4.4 Spatially-Multiplexing Grating Compressor

To accommodate the compression of both channels within the limited setup space, a spatially multiplexed grating compressor was built up. It is based on the principle of the Treacy compressor [130], whose design is shown in Fig. 4.11. A Treacy compressor is based on a pair of two parallel gratings that are spatially separated by a distance b with their grating surfaces directed towards each other. A pulse impinging on the first grating surface by an angle α is diffracted with a diffraction angle β depending on the wavelength. In combination with the second grating, all spectral components travel collinearly after experiencing a wavelength-depending group delay. The collinear

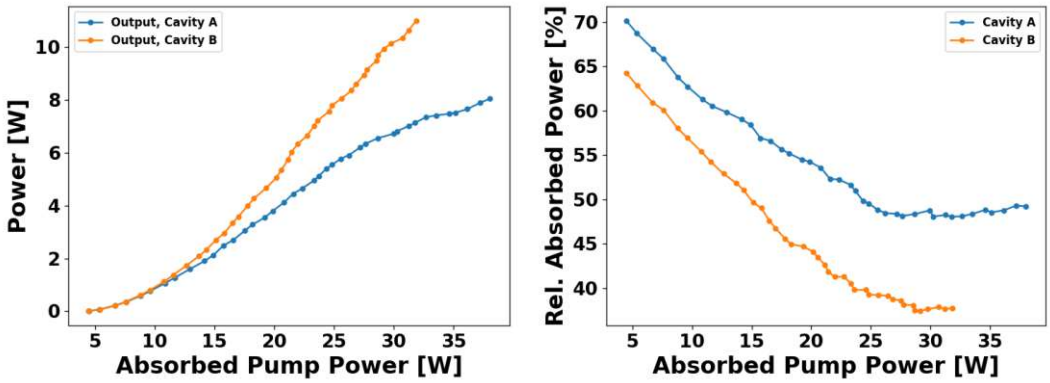

(a) CW output characteristics of the Twin RA. (b) First-pass relative absorbed pump power.

Figure 4.10: CW characterization of the Twin RA.

components can be redirected through the compressor-pair path by a retroreflecting mirror (M), to be recombined into a single pulse. The compressed pulse can be separated from the input by suitable means (e.g. by polarization methods or spatial separation). The total group delay τ_G between two wavelengths λ and $\lambda + \delta\lambda$ can be calculated as [130]

$$\frac{\partial \tau_G}{\partial \lambda}\delta\lambda = \frac{b\lambda}{c_0 d^2(1-(\frac{\lambda}{d}-\sin\gamma)^2)}\delta\lambda \tag{4.2}$$

with c_0 being the speed of light and d the grating constant.

It is possible to develop further the basic Treacy concept by using a transmission grating with two retroreflecting mirrors. This way, it is possible to use only a single grating. By the use of a sufficiently large grating, a spatially multiplexing dual compressor can be realized (Fig. 4.12). For each arm, the setup consists of three main parts: a horizontal retroreflector (HRR) mounted on a manual translation stage (TS), a vertical retroreflector that offsets the beam vertically to separate the input path from the output path and a transmission diffraction grating (G) with size 130x20 mm^2 (Gitterwerk), which is shared by the two channels. The combination of HRR and manual TS sets the distance b (Equ. 4.2) for each channel. One needs to be careful to align the VRR correctly such that the back-reflection is properly reflected by 180°with a pure vertical offset. Otherwise, a horizontal spatial chirp is imposed on the pulse, which can be noticed when sending the pulse beam into a spectrometer and slightly tuning its input angle with the input mirror setting.

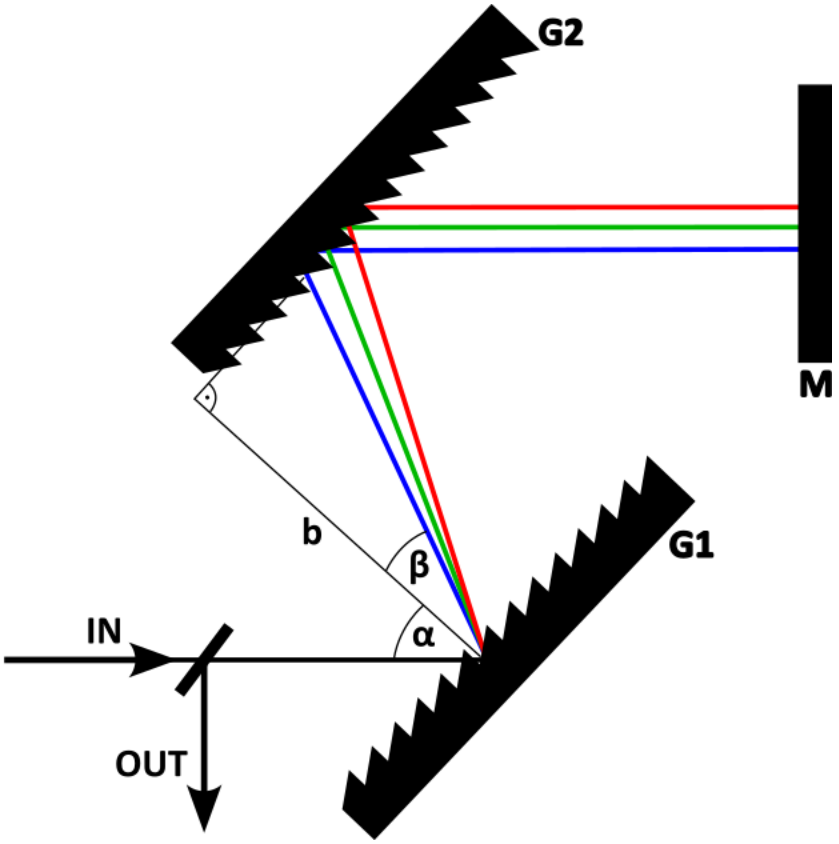

Figure 4.11: The Treacy compressor as described in [130].

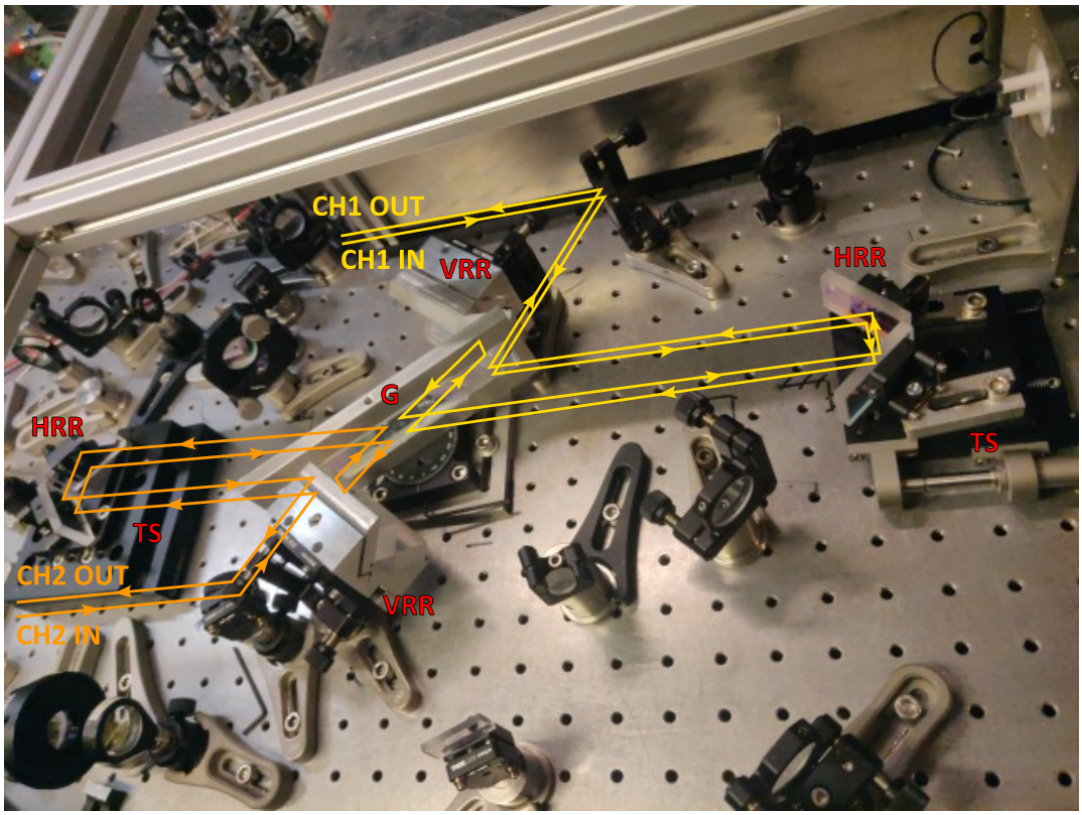

Figure 4.12: Spatially-multiplexing grating compressor for two channels.

Chapter 5

Phase-Scrambled CPA (PSCPA)

A multitude of applications require millijoule pulse energies with only a small degree of spectral selectivity, for which the generation and amplification of bursts with a handful ($N \leq 10$) of pulses can be a useful approach. In general, burst-mode amplification is frequently perceived as more efficient compared to single-pulse amplification, because the energy stored in the laser material is shared among N pulses. Therefore, the effective pulse duration is increased by a factor of N in the amplifier and the extractable energy scales with the square root of the pulse number $\sqrt{N}$, an advantage which is explored in many variants of divided-pulse amplification. This is comparable to CPA, where for pulse durations longer than 10 ps, the energy extraction scales with the square root of the stretched pulse duration $\sqrt{\tau}$ [131–134]. Several challenges arise, however, when applying the concept of CPA to ultrashort-pulse bursts at THz intraburst rates with $N > 1$. Burst pulses are very close together, with maximum interpulse spacings of only a few picoseconds. Strongly chirping burst pulses with such parameters together up to several hundreds of picoseconds for CPA leads to strong pulse overlap, which induces several challenges during amplification. To meet these challenges, phase-scrambled CPA (PSCPA) was developed in the course of this thesis and its results are shown in this chapter, which is structured as follows: The parameter space in which PSCPA becomes relevant is discussed in detail in Chapter 5.1. Chapter 5.2 communicates the underlying concept. Experimental results for the technique are shown in Chapter 5.3. In the end, scalability regarding the extractable energy for increasing pulse numbers, especially in comparison to the CPA-only case, is discussed in Chapter 5.4. The author notes that parts of this subchapter were already published in a similar form in the author's work [1, 5].

5.1 The Regime of PSCPA

It is highly relevant to consider the regime in which PSCPA becomes relevant. For sufficiently strongly chirped pulse durations compared to the temporal duration of the compressed burst $(N-1)\Delta t$, the burst spectrum is well present in the time domain (as will be demonstrated experimentally in Chapter 7). Assuming linearly chirped pulses, as formulated in Eq. 1.3, the burst temporal intensity can be derived numerically using Fourier transform methods together with Eq. (1.10). From the compressed-pulse case up to strongly chirped pulses with hundreds of ps duration, the temporal peak intensity was

calculated for up to $N = 10$ pulses with 1 ps spacing, while keeping the total burst energy constant. The results can be seen in Fig. 5.1. The sub-ps duration range determines the regime where divided-pulse amplification (DPA) is applied [132] and is indicated by a $1/N$-decrease of the temporal peak intensity (see Fig. 5.1, lower left inlay) by an equal distribution of the total energy among the burst pulses. In the other case, for strongly stretched pulses with chirped pulse durations of several hundreds of picoseconds, the behavior is the opposite: by increasing pulse number, we see an N-times increase in the temporal peak intensity compared to the single pulse case (see Fig. 5.1, upper right inlay), which identifies the PSCPA regime. In this region, the burst spectral peaks are well present in the time domain and thus decrease amplifier reachable energy and stability.

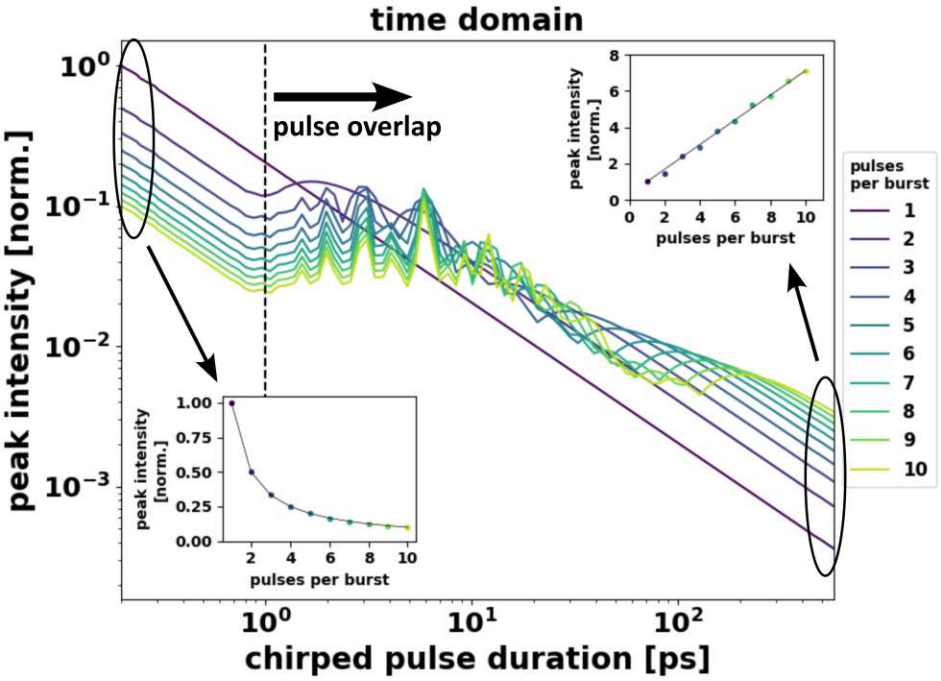

Figure 5.1: Maximum temporal peak intensity for a burst of chirped pulses with a pulse spacing of 1 ps, depending on the chirped pulse duration. The plot is shown for various pulse numbers while keeping the total burst energy constant, with temporal peak intensity being normalized to the compressed single pulse case. Lower left inlay: Maximum temporal peak intensity (normalized to the corresponding single-pulse case) vs. pulse number in the case of fully compressed 250 fs pulses. Upper right inlay: Maximum temporal peak intensity (normalized to the corresponding single-pulse case) vs. pulses number in the case of pulses stretched to 600 ps.

5.2 Concept

As illustrated in Fig. 5.2, the energy safely extractable from a chirped pulse amplifier rapidly drops for $N > 1$. A burst composed of N spectrally overlapping pulses with constant phase offsets exhibits discrete spectral lines, spaced at the intraburst repetition rate, as an outcome of spectral interference. Therefore, compared to single-pulse operation,

the peak intensities inside the amplifier increase by a factor of N for the same output energy (Fig. 5.1). The N-proportional scaling reflects the growth of temporal peak intensities due to interference, as a result of frequency-to-time mapping at high chirp rates. To resolve this detrimental consequence of mode formation, a phase-scrambling technique can be employed which inhibits constructive interference by applying programmable phase offsets $\phi_{offset,n}$ to each intraburst pulse. These offsets are combined with a constant pulse-to-pulse phase slip $\Delta\phi_s = k\Delta L = k(L_{MO} - L_{RA})$ which follows from the mismatch of the MO-RA cavity roundtrip lengths ΔL, with k being the wavenumber. The phase differences between subsequent intraburst pulses become

$$\phi_n - \phi_{n-1} = \Delta\phi_s + (\phi_{offset,n} - \phi_{offset,n-1}), \tag{5.1}$$

with $n = 2, 3, ..., N$.

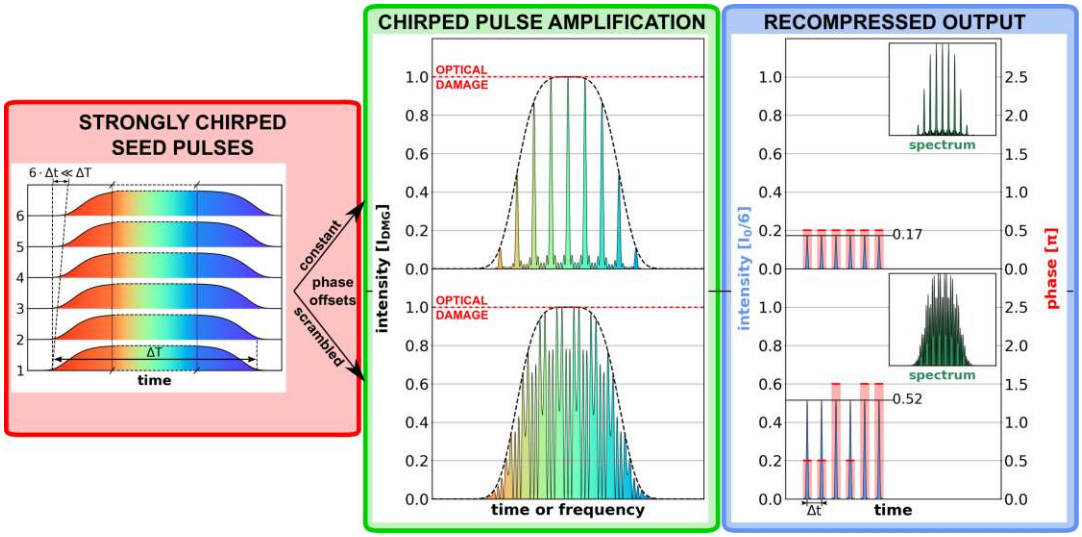

Figure 5.2: Safe chirped amplification of a burst utilizing phase-scrambling. Left: Composition of the seed burst from strongly chirped overlapping intraburst pulses. Middle: Spectral or temporal intensity of the amplified strongly chirped burst, normalized to the optical damage threshold intensity I_{DMG} of the RA, with pronounced spectral modes in the case of constant phase offsets (middle, upper panel). This can be avoided by programmable scrambling of the phase offsets (middle, lower panel). An amplified single chirped pulse is shown for comparison (black dashed line). Right: Time-domain representation of intensity (blue) and phase (red) after compression with the intensity normalized to I_0/N, with I_0 being the maximum output peak intensity of a single pulse and N the pulse number. The inset shows the spectrum (green).

5.3 Experimental Demonstration

To demonstrate PSCPA experimentally, SHG autocorrelations and spectra of several bursts were measured. By an appropriate choice of burst phase offsets, the burst spectrum is shaped to maximally resemble the single-pulse spectrum. The bursts were amplified to 100 μJ using the CPA technique with sub-ps pulse duration, about 1 ps pulse spacing and

varying pulse number. Amplification dynamics in the RA and modulation of the phases slightly affected the amplitudes of burst pulses, however, this could be precompensated by the AOM settings for intensity modulation to achieve a constant intensity level.
The measured SHG autocorrelations and spectra could be well reproduced by numerical calculations (See Figs. 5.3-5.8) with the pulse-to-pulse phase slip as the only fit parameter. The measured single pulse spectrum and programmed phase offsets together with the Fourier-shift theorem were used to calculate the burst spectrum. It was assumed, that every intraburst pulse contains the measured single-pulse spectrum. The applied phase offsets were assumed to be imprinted on the pulses as they were programmed to the AOM and are listed in Tab. 5.1. The listed phase offsets were calculated to enable the highest achievable extractable energies in this burst regime when allowing only π-phase shifts.

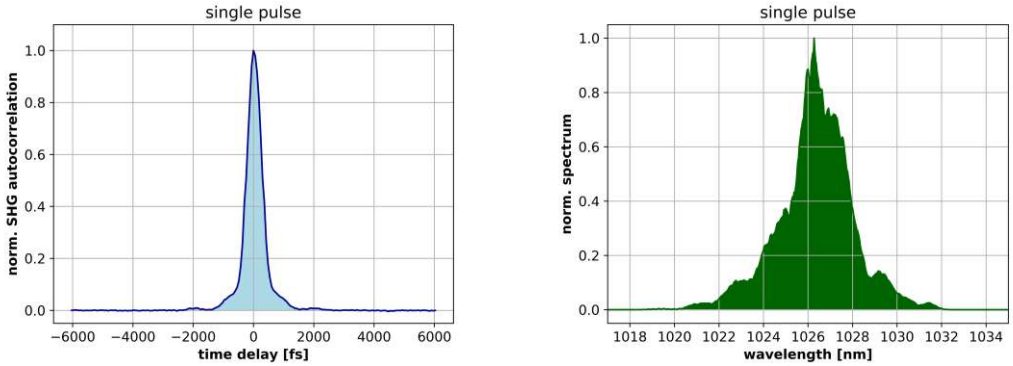

(a) (b)

Figure 5.3: Measurement results for a single pulse. Normalized a) SHG autocorrelation and b) spectrum.

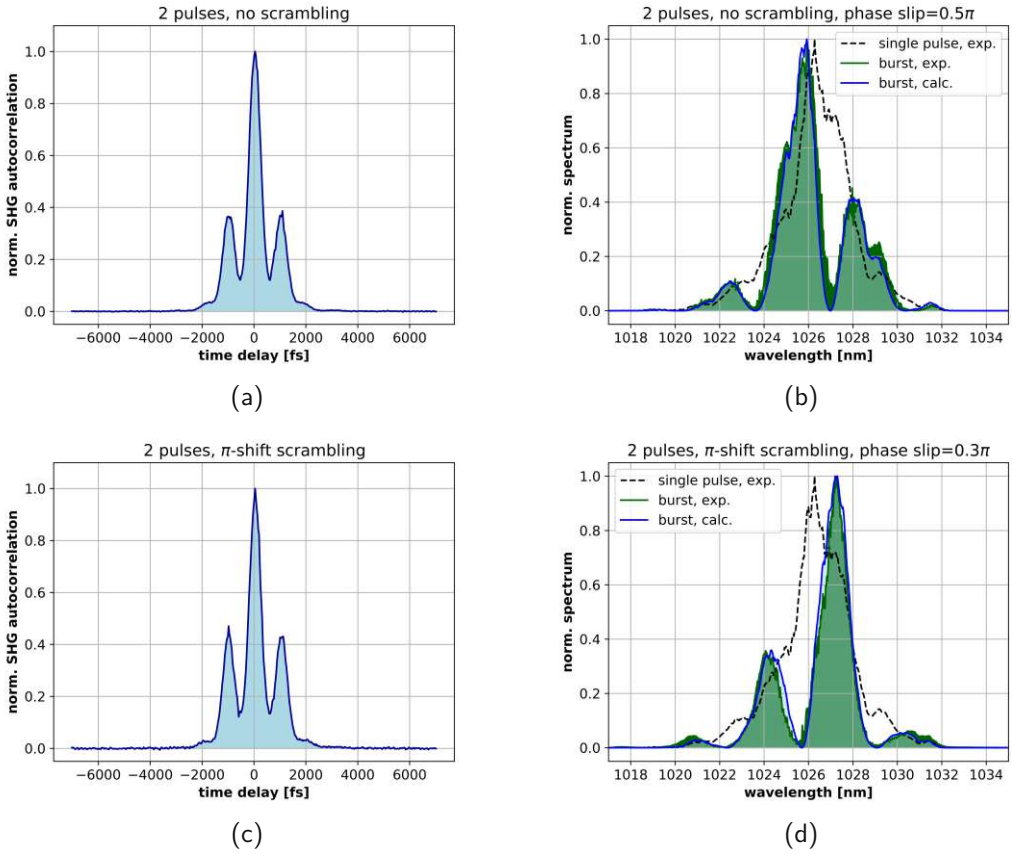

Figure 5.4: Measurement results for a burst with 2 pulses. Normalized SHG autocorrelation and spectrum with a), b) zero programmable phase offsets, and with c), d) scrambled phases with π phase shifts.

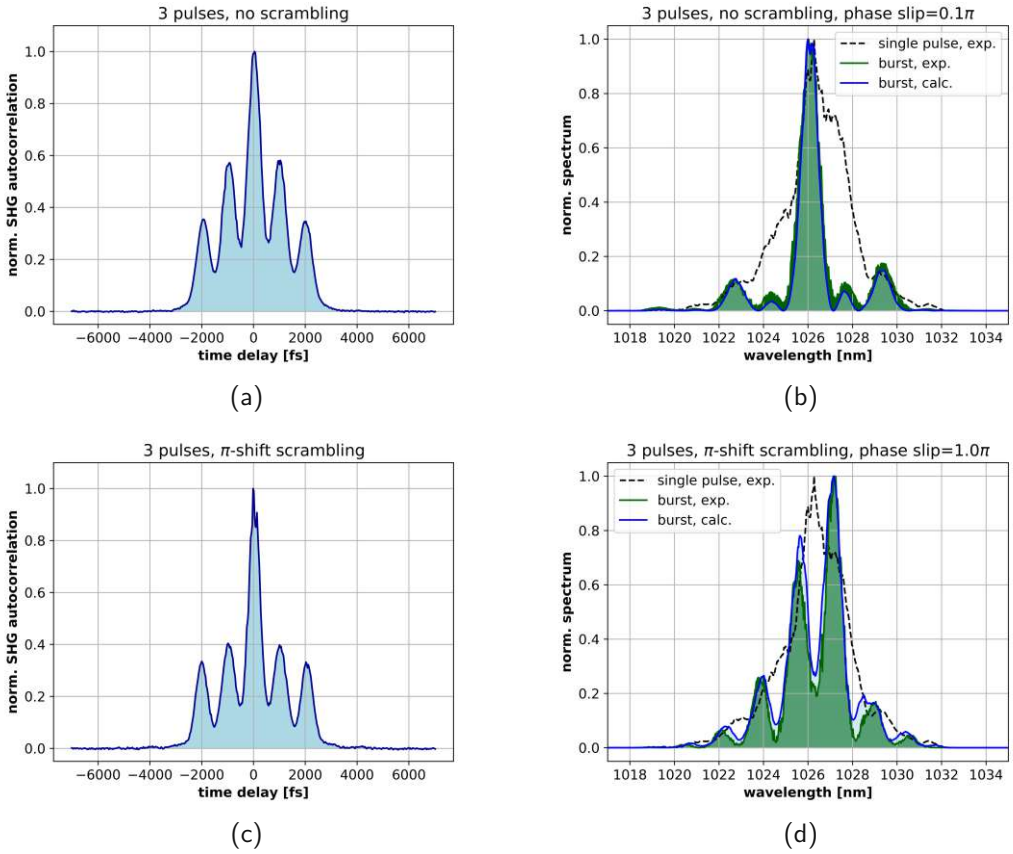

Figure 5.5: Measurement results for a burst with 3 pulses. Normalized SHG autocorrelation and spectrum with a), b) zero programmable phase offsets, and with c), d) scrambled phases with π phase shifts.

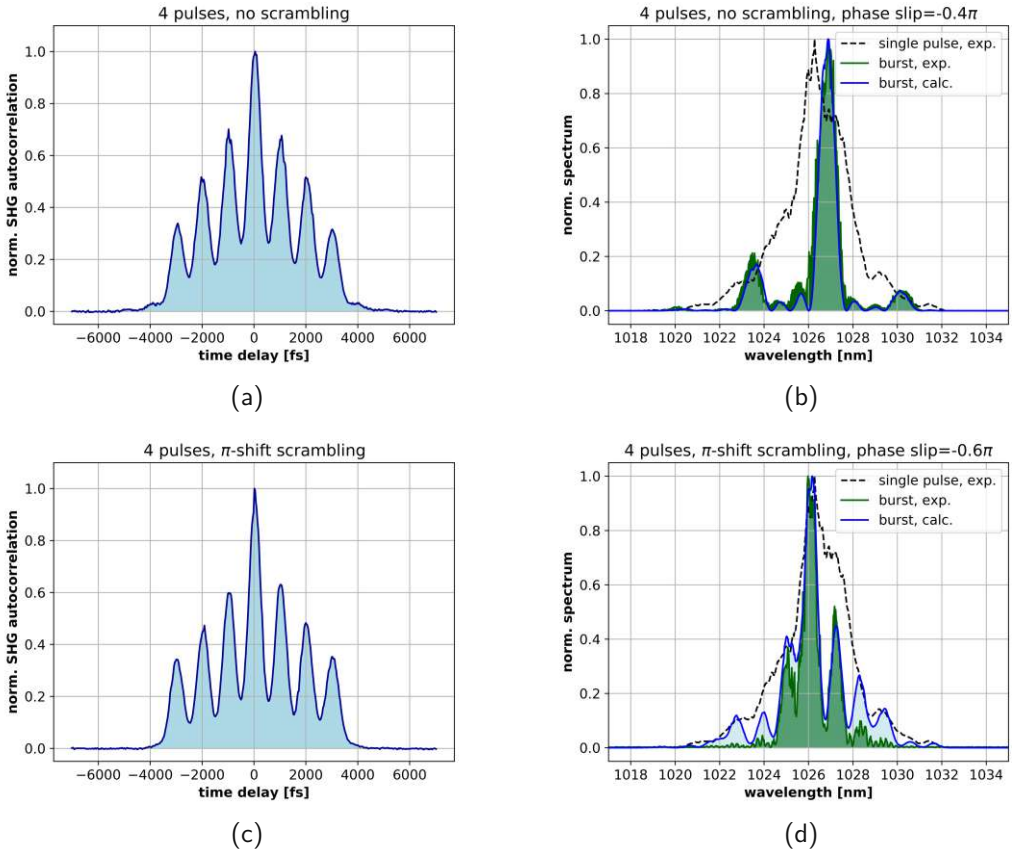

Figure 5.6: Measurement results for a burst with 4 pulses. Normalized SHG autocorrelation and spectrum with a), b) zero programmable phase offsets, and with c), d) scrambled phases with π phase shifts.

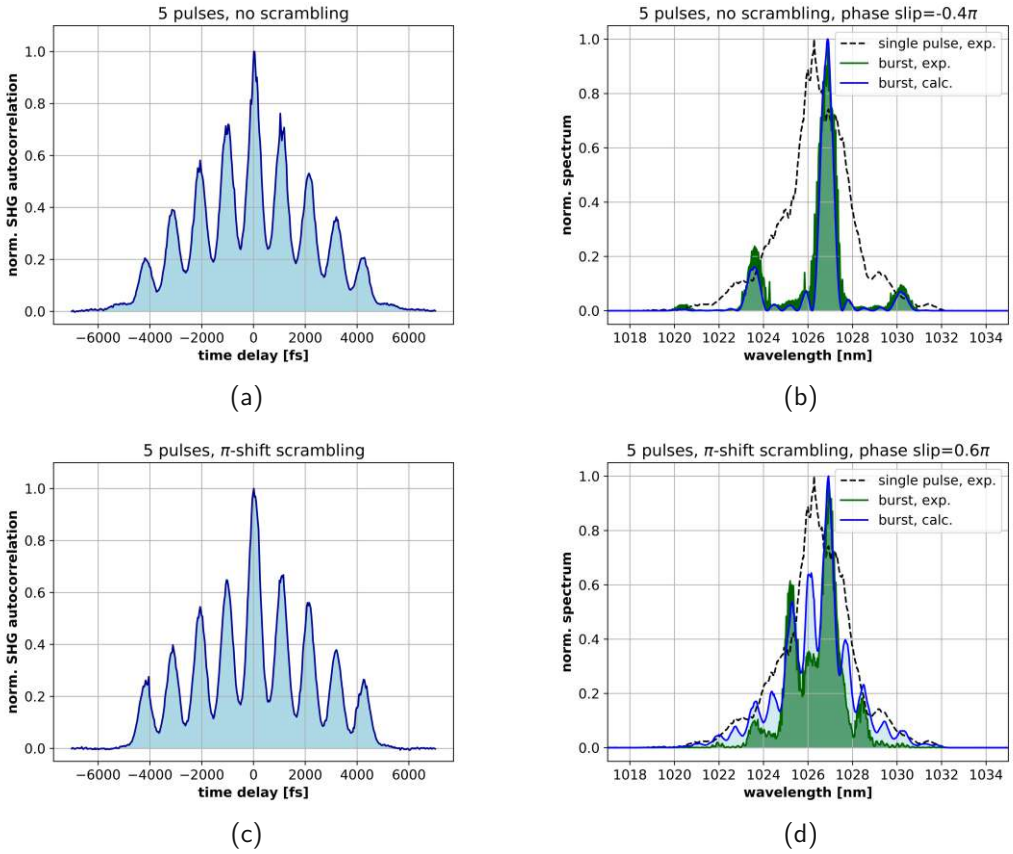

Figure 5.7: Measurement results for a burst with 5 pulses. Normalized SHG autocorrelation and spectrum with a), b) zero programmable phase offsets, and with c), d) scrambled phases with π phase shifts.

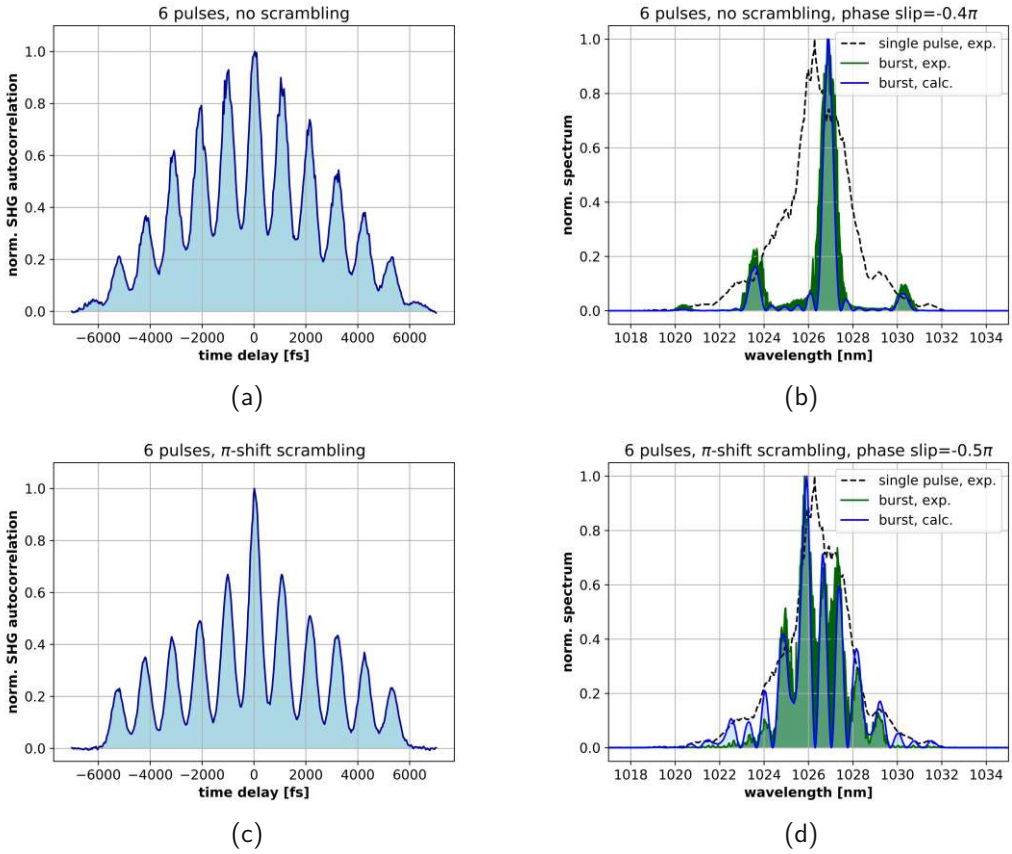

Figure 5.8: Measurement results for a burst with 6 pulses. Normalized SHG autocorrelation and spectrum with a), b) zero programmable phase offsets, and with c), d) scrambled phases with π phase shifts.

N	$\phi_{offset,n}$
2	$0, \pi$
3	$0, 0, \pi$
4	$0, 0, \pi, 0$
5	$0, 0, 0, \pi, 0$
6	$0, 0, \pi, 0, \pi, \pi$

Table 5.1: Programmable phase offsets applied for phase-scrambling.

5.4 PSCPA Extractable Energy

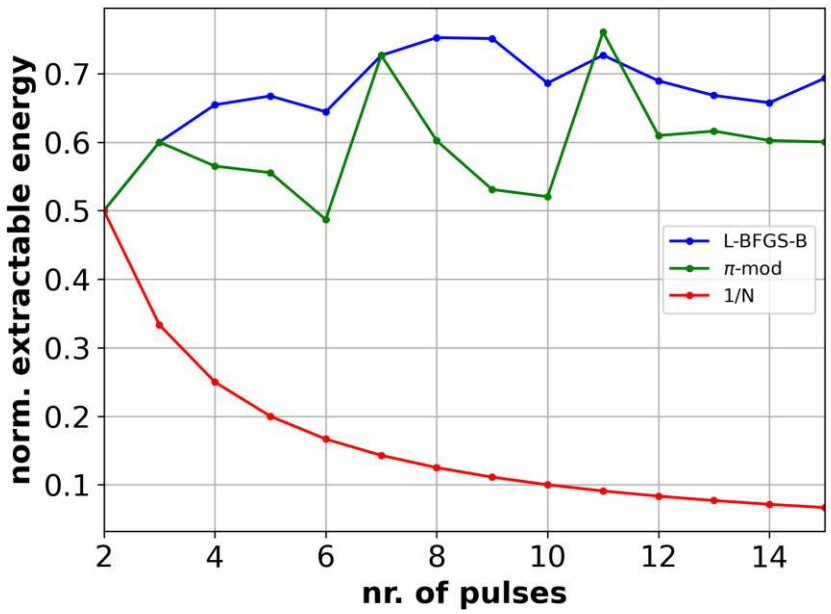

Figure 5.9: Maximum extractable energy without exceeding the optical damage threshold in burst-mode normalized to the single-pulse case vs. pulse number N. Calculation with a programmable phase offset which is constant (red), optimized by a numerical L-BFGS-B algorithm (blue) and the global maximum when allowing only 0 or π phase offsets (green).

In this section, the potential of PSCPA is explored by determining the maximum extractable energy achievable by phase-scrambling as a function of the burst pulse number N. In the PSCPA regime, it can be assumed in good approximation, that the chirped pulses overlap strongly in time. Thus, the functional form of the temporal intensity profile is equal to the spectral profile of the waveform. This statement is proven numerically and experimentally in chapter 7. Therefore, these calculations evaluate energies by considering the burst spectra. The burst energy ϵ_B is calculated relative to the extractable single-pulse energy ϵ_P under the assumption of identical Gaussian spectra for intraburst pulses (Fig. 5.9):

$$\frac{\epsilon_B}{\epsilon_P} = \frac{\int I_B(\omega)d\omega}{\int I_P(\omega)d\omega}, \tag{5.2}$$

where $I_B(\omega)$, $I_P(\omega)$ are the spectral intensities of a burst and a single pulse, respectively, and $\max\{I_B(\omega)\} = \max\{I_P(\omega)\} = I_{THR}$.
Optimized sets of phase offsets are determined in two ways: first, by a numerical optimization algorithm (L-BFGS-B) [135] and second, by calculating the global maximum energy with restricting the phase offset to 0 and π (π-mod). Without phase-scrambling, the maximum extractable energy is inversely proportional to the pulse number. In contrast, for both illustrated phase-scrambling cases, the relative extractable energy stays reliably above 50% and approaches approximately 70% of the maximum single-pulse energy for higher pulse numbers.

5.5 PSCPA in the Viewpoint of the Burst Spectrum Fourier Series

An insight into why particular phase slip patterns are more useful for phase scrambling than others can be acquired by analyzing the Fourier series of the burst spectrum.
The spectral intensity of a burst can be formulated as

$$I(\omega) = \tilde{E}(\omega)\tilde{E}^*(\omega) \tag{5.3}$$

$$= \sum_{n=0}^{N-1} \tilde{E}_P(\omega)e^{i(\phi_{n1}-n\Delta t\omega)} \sum_{m=0}^{N-1} \tilde{E}_P^*(\omega)e^{-i(\phi_{m1}-m\Delta t\omega)} \tag{5.4}$$

$$= I_P(\omega) \sum_{n=0}^{N-1}\sum_{m=0}^{N-1} e^{i(\phi_{n1}-\phi_{m1})} \cdot e^{-i\Delta t\omega(n-m)}. \tag{5.5}$$

By separation of the summands with indices $m = n$ and $m \neq n$ this can be formulated as

$$I(\omega) = I_P(\omega) \cdot \left(N + \sum_{n=0}^{N-1}\sum_{\substack{m=0 \\ m\neq n}}^{N-1} e^{i(\phi_{n1}-\phi_{m1})} \cdot e^{-i\Delta t\omega(n-m)} \right) \tag{5.6}$$

$$= I_P(\omega)\cdot$$

$$\left(N + \sum_{n=0}^{N-1}\sum_{m=0}^{n-1} (e^{i(\phi_{n1}-\phi_{m1})}e^{-i\Delta t\omega(n-m)} + e^{-i(\phi_{n1}-\phi_{m1})}e^{i\Delta t\omega(n-m)}) \right) \tag{5.7}$$

$$= I_P(\omega) \cdot \left(N + \sum_{n=0}^{N-1}\sum_{m=0}^{n-1} 2\cos((\phi_{n1}-\phi_{m1}) - \Delta t\omega(n-m)) \right) \tag{5.8}$$

With a change of variables

$$s = m \tag{5.9}$$

$$s - r = n \tag{5.10}$$

and an appropriate change of the summation limits, Eq. (5.8) can be formulated as

$$I(\omega) = I_P(\omega) \cdot \left(N + \sum_{r=1}^{N-1} \sum_{s=r}^{N-1} 2\cos(\phi_{(s-r)1} - \phi_{s1} + \Delta t \omega r) \right) \tag{5.11}$$

$$= I_P(\omega) \cdot \left(N + \sum_{r=1}^{N-1} \sum_{s=r}^{N-1} 2\cos(\phi_{(s-r)1} - \phi_{s1})\cos(\Delta\omega r) - 2\sin(\phi_{(s-r)1} - \phi_{s1})\sin(\Delta t \omega r) \right) \tag{5.12}$$

$$= I_P(\omega) \cdot \left(N + \sum_{r=1}^{N-1} a_r \cos(r\Delta t\omega) + b_r \sin(r\Delta t\omega) \right) \tag{5.13}$$

$$a_r = \sum_{s=r}^{N-1} 2\cos(\phi_{(s-r)1} - \phi_{s1}) \tag{5.14}$$

$$b_r = -\sum_{s=r}^{N-1} 2\sin(\phi_{(s-r)1} - \phi_{s1}) \tag{5.15}$$

The Fourier coefficients a_r, b_r give a qualitative understanding of the optimally scrambled phases which give the maximum extractable energy without optical damage: Index r corresponds to the interference of pulses which have a temporal spacing of $r \cdot \Delta t$[1]. In Fig. 5.10, the Fourier coefficients were calculated according to a numeric optimization algorithm (L-BFGS-B) and according to the global optimum when allowing only π phase-shifts[2]. For the latter case, all sine-coefficients b_r are zero due to the phase restriction. However, also for the former case, the cosine-coefficients a_r have a greater value than the sine-coefficients a_r with the $r = 15$ coefficient being the largest and absolute values decreasing for decreasing r. This makes sense in such a way, that those pulses that are farthest apart from each other represent the spectral modulation with the lowest spectral period (See Eq. (5.13)), which needs to be favored for generating a quasi-incoherent spectrum.

[1] See e.g. the argument of cosine and sine in Eq. (5.13)
[2] allowed phases being restricted to zero and π

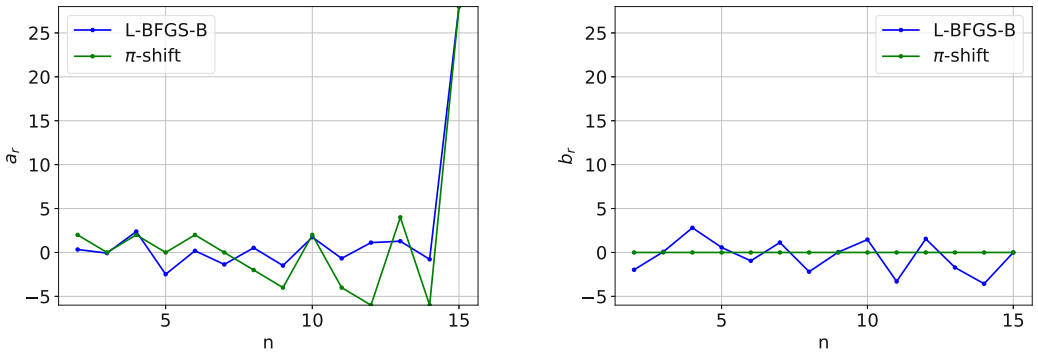

(a) (b)

Figure 5.10: Fourier (a) sine-coefficients a_r, (b) cosine-coefficients b_r (b) with optimal phases according to a numeric optimization algorithm (L-BFGS-B) and globally optimized while allowing only π phase-shifts (π-shift), both concerning optimal energy extraction.

Chapter 6

Spectral Peak Recovery by Parametric Amplification

PSCPA solved the problem of scaling the amplifier reachable energy of THz rate bursts of ultrashort pulses. However, it required the scrambling of the burst spectrum. This means giving up the burst spectral peak structure, which in many cases can be highly useful to several applications (see Chapter 3). In this chapter, a method is presented that combines PSCPA with a parametric frequency converter that automatically restores the desired spectral peak structure and delivers narrow linewidths for bursts of ultrashort pulses at microjoule energies.
The general concept is communicated in Chapter 6.1, followed by the experimental realization in Chapter 6.2. Finally, the experimental results are presented in Chapter 6.3, including single-shot cross-correlations and scanning cross-correlations of the NIR amplified burst with a compressed reference pulse and measured spectra of the initial NIR driver burst and the OPA idler/signal bursts which were further compared to theory. The author notes that parts of this subchapter were already published in a similar form in the author's work [127].

6.1 Concept

To be a useful tool for several applications, ultrashort pulses need to be amplified to at least sub-millijoules. While for an intraburst repetition rate of some GHz or lower, amplification is a straightforward task, the application of chirped-pulse amplification (CPA) [45] to THz-repetition-rate bursts leads to various difficulties, such as a strong reduction of the reachable energy and potential amplifier damage due to interference effects during amplification, as was discussed in Chapter 5. This is because of the translation of the burst spectrum into the time domain when amplifying a handful of ps-spaced, strongly chirped pulses in an amplifier when the stretched pulse duration strongly exceeds the duration of the burst. The use of PSCPA overcomes the mentioned technical limitations, which leads to a smearing of the burst-typical spectral peak structure.
However, while the suppression of spectral peaks allows for mJ burst amplification, it removes the capability to be spectrally selective when applying amplified bursts. In this chapter, the recovery of the burst spectral peak structure after PSCPA by parametric

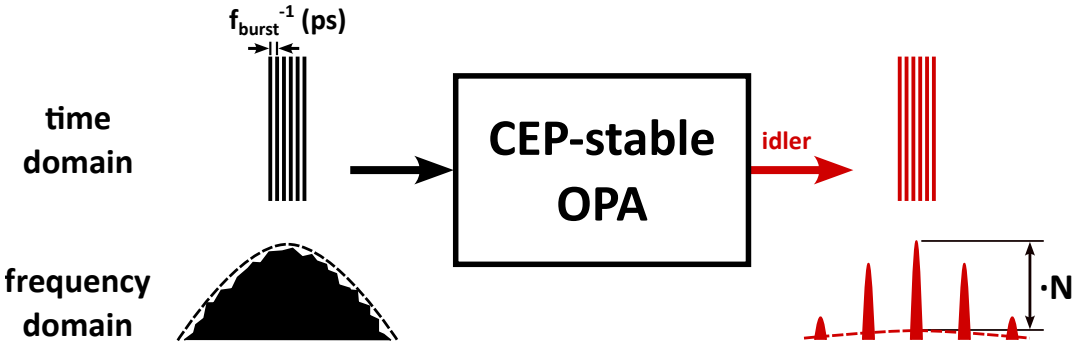

Figure 6.1: Concept of utilizing a passive CEP-stabilizing OPA to recover the spectral peak structure of a burst of ps-spaced ultrashort pulses amplified via PSCPA by the generation of a μJ phase-descrambled idler burst. Bursts are outlined in the time- and frequency domain. In the frequency domain, the single pulse spectrum is depicted as a dashed line and the burst spectrum as a solid line with a filled area underneath. On the left side, the phase-scrambled spectrum shows a resemblance to the single pulse spectrum because the spectral interference is suppressed. On the right side, the phase-descrambled spectrum shows an N-proportional increase in spectral peak intensity compared to the spectrum of a single pulse with the same total energy.

amplification is demonstrated. As outlined in Fig. 6.1, an Optical-Parametric Amplifier (OPA), that is capable of passive CEP stabilization, is driven with a burst that is amplified to sub-mJ energies by application of PSCPA. For individual pulses, the concept of passively stabilizing the CEP with OPAs is already widely known [118]. It is based on the cancellation of signal and pump pulse CEPs when being imprinted on the idler signal. In the present work, the same applies to every individual pulse within the burst, given the fact that all relevant nonlinear processes (SHG, SFG, DFG, SPM) occur on timescales much smaller than the pulse spacing of > 1 ps. The second harmonic of the driving burst serves as a pump and generates a white-light continuum signal seed. This leads to a μJ idler signal with phase-descrambled burst pulses and a recovery of the spectral peak structure.

6.2 Experimental Setup

6.2.1 Overview

The full experimental overview of this work can be seen in Fig. 6.2a, together with a temporal and spectral visualization of the burst labeled with Roman digits in between each of the stages in Fig. 6.2b. In general, the amplification chain consists of a PSCPA part (Fig. 6.2b I-V) followed by a phase-descrambling spectral peak recovery part represented by the OPA (Fig. 6.2b V-VI). The PSCPA setup is the same as it is described in Chapter 4.3. The OPA and the cross-correlation stage were built up for this experiment.
The MHz-repetition-rate mode-locked oscillator generates nanojoule pulses, which correspond to narrowband, MHz-spaced spectral comb teeth below the single-pulse envelope (Fig. 6.2b I). The stretcher mainly imprints a spectral phase to stretch the pulses (Fig. 6.2b II). Because of gain narrowing during amplification, precompensation by shaping the pulse spectrum in the Fourier plane of the stretcher is also applied but not depicted in

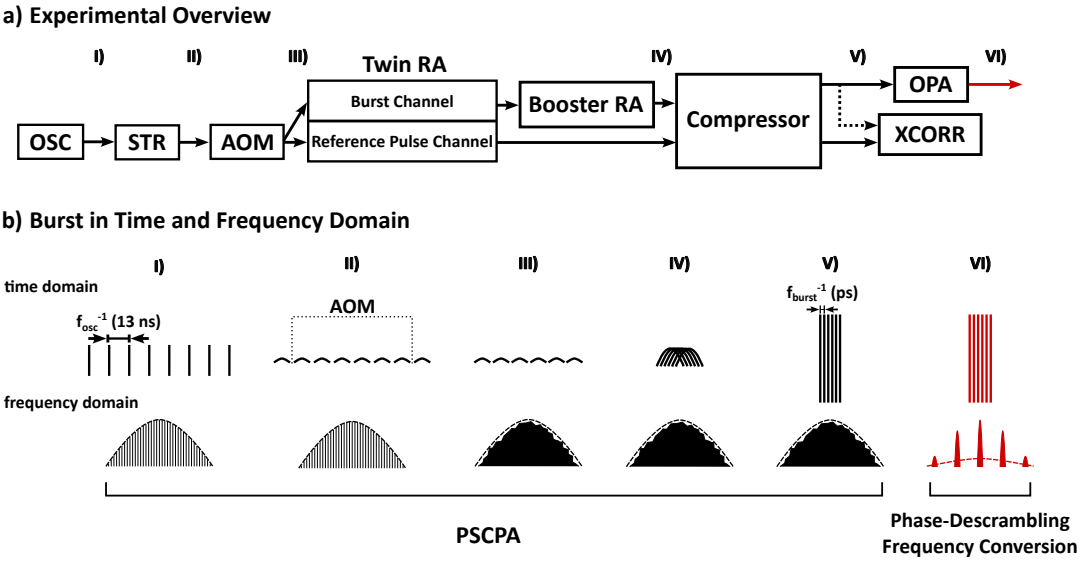

Figure 6.2: a) Experimental Overview. OSC: Mode-locked MHz Oscillator. STR: Stretcher. AOM: Acoustic-Optic Modulator. RA: Regenerative Amplifier. OPA: Optical Parametric Amplifier. XCORR: Cross-Correlation Stage. PSCPA: Phase-Scrambled Chirped Pulse Amplification. b) Burst Hybrid Amplification in the time and frequency domain. Single-pulse spectra are represented as dashed lines, and multi-pulse spectra as solid lines with a filled area underneath.

the Figure due to clarity. The constructive spectral interference is suppressed because of the phase scrambling by suitable pseudo-random pulse phase modulation. Thus, the multi-pulse spectrum resembles the single-pulse spectrum (6.2b III). Amplification takes place at a repetition rate of 1 kHz. For being able to determine individual burst pulse energies after amplification, a single pulse is amplified as a reference parallel to the burst for direct temporal burst characterization. This enables the equalization of burst pulse energies by gain precompensation carried out by amplitude modulation in the AOM. Strong variations in burst pulse energies would otherwise deteriorate the parametric conversion performance of the burst in the OPA since all relative intensity variations are increased further by nonlinear processes. In the Twin RA, the burst is amplified to about 100 μJ of burst energy and the reference pulse to 50 μJ. The burst is amplified further up to 200 μJ for each burst pulse (Fig. 6.2b IV) in a home-built cryogenically cooled Yb:CaF_2 booster amplifier. The burst pulses and the reference pulse are then recompressed (Fig. 6.2b V) to a pulse duration of 250 fs in the compressor. Losses in the compressor have been determined to be around 30%, resulting in a compressed burst pulse energy of 140 μJ and a compressed reference pulse energy of 35 μJ. Bursts consisting of 6 pulses were generated, which results in a compressed burst energy of 840 μJ. The compressed pulse burst is then sent into a passive CEP-stabilizing OPA for spectral peak recovery. The idler output of the OPA gives a burst of ultrashort pulses at μJ energies with a clean spectral modulation coming from the spectral interference of phase-descrambled burst pulses (Fig. 6.2b VI). A small part (few μJ) of the PSCPA burst is sent together with the reference pulse to a cross-correlation stage for the determination of individual burst pulse energies. For the cross-correlation measurement, the temporal envelope of the whole burst

is measured by scanning the time delay between the burst and the reference pulse with a mechanical delay line. As a signal the sum frequency signal generated in a type I β-barium borate (BBO) nonlinear crystal during the overlap of the burst with the reference pulse under a few-degree angle is detected.

6.2.2 Phase-Descrambling Frequency Conversion in an OPA

The OPA represents a phase-descrambling frequency conversion stage, in which the phase difference between the pump and the signal is imprinted on the idler. The burst spectral peaks and the scrambling of phases in PSCPA regard only the relative CEP $\phi_{0,i}$ that is given by the CEP of burst pulse i relative to the first burst pulse. In contrast, the OPA can passively stabilize the total CEP of burst pulses and therefore also the relative CEP $\phi_{0,i}$ of burst pulses with respect to each other. When the CEPs of each pump and signal pulse pair are equal, the idler pulses are all expected to have the same CEP. This is the burst equivalent of a well-known process for individual pulses, whose single-pulse description is completely applicable to this case since the individual burst pulses are well separated from each other in time, given a pulse duration of about 250 fs and a pulse spacing of more than 1 ps [118]. This way, passive CEP stabilization demodulates individual burst pulses in their phase and thus allows for a recovery of the burst spectral peak structure that is lost during PSCPA. Further, this concept of OPA phase descrambling enables conversion of the carrier frequency from the NIR, where highly efficient amplification is possible, to any OPA-reachable desired frequency.

Fig. 6.3 shows a conceptual scheme of the passive CEP-stabilizing OPA used for the experiments in this work. As mentioned in the section before, the OPA is driven by an NIR burst consisting of 6 pulses, each amplified to 140 μJ. The second harmonic of the NIR input burst is applied both as the pump for the OPA stages and generation of the WLG seed burst. The second-harmonic conversion efficiency is about 35% resulting in a 50 μJ second-harmonic burst. The individual burst pulse energy is not increased further because of the onset of parametric superfluorescence in the OPA stages at higher pump energies. Due to the use of the second harmonic, there are twice the individual pulse relative phases $\phi_{0,j}$ each imprinted on the pump pulses and the WLG seed pulses. The first-stage OPA crystal (BBO Type I) is tuned to an angle to achieve phase matching at around 690 nm. While the signal of the first stage acquires twice the original individual pulse relative phases, the idler has a constant CEP for all burst pulses ($\phi_{0,j}$=0). However, to get a sufficient signal-to-noise ratio (SNR), the first stage is operated non-collinearly, and the signal is separated spatially from the idler burst by a few-degree angle and, further, the signal is amplified in a collinear second stage (BBO Type I). The spectra of the seed pulse, of the second-stage signal at around 690 nm and of the idler at 2030 nm are measured, with idler energies being a few μJ.

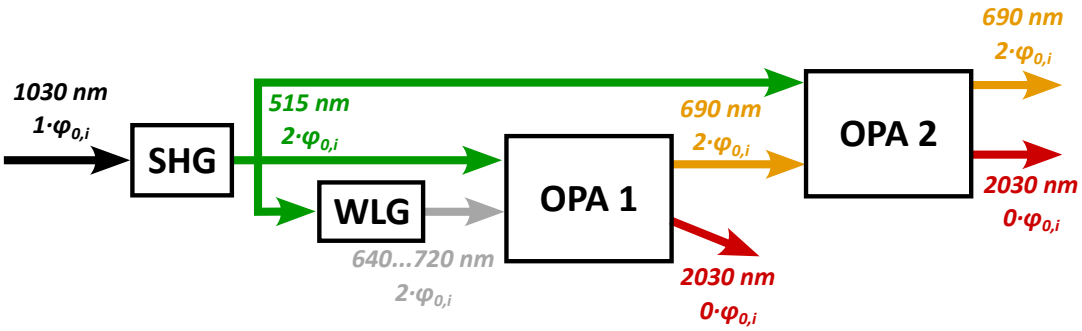

Figure 6.3: 2-stage OPA scheme for phase-descrambling and frequency conversion. SHG: Second-Harmonic Generation. WLG: White-Light Generation. OPA: Optical-Parametric Amplifier.

6.2.3 Detailled description of passively CEP-stabilizing two stage OPA

Fig. 6.4 shows the setup of the passively CEP-stabilizing two-stage OPA in detail. The burst with original fundamental frequency ω_{in} is generating a second-harmonic signal (SHG). Each burst pulse had an energy of about 140 μJ, out of which a second harmonic pulse with about 50 μJ has been generated corresponding to a conversion efficiency of 35%. After SHG conversion, a dichroic mirror (DM) reflects the fundamental signal on a beam dump (BD) allowing only the SHG signal to enter the OPA. Control of the ratio of pump vs. white-light generation (WLG) driver was done by a combination of half-wave plate (HWP) and thin-film polarizer (TFP). Only a few microjoules were used for the generation of the white-light seed. The WLG process was controlled by the amount of driver energy, the opening of the aperture (AP) and the distance between the lens (L1) and the YAG plate. After the plate, the SHG pump is filtered (F1) and the generated WL is focused by a lens (L2) into the first OPA stage (OPA1) which was realized by a type I BBO crystal angle-matched to about 690 nm, with 4 μJ of the SHG pump whose timing was controlled by a translation stage (TS). The OPA1 was operated non-collinearly to separate the signal from the idler signal. The signal from the first stage is then sent into a second collinear stage (also BBO Typ I) for further amplification using 8 μJ of the SH pump. The 2030 nm idler from the second stage is then converted into a 1015 nm signal by SHG in a type I BBO, such that its wavelength fits the wavelength range of our lab-available high-resolution spectrometer (Avantes AvaSpec-ULS4096CL-EVO) after filtering out the green 515 nm pump after both stages (by F2, F3) and the amplified 690 nm signal (by F4).

6.3 Results

First, results for a single-shot cross-correlation technique are shown, which has the advantage of being able to deliver information about burst pulse energies from individual cycles. From these, we could see, that the burst is sufficiently stable and that scanning cross-correlation can be applied, which provides a larger scan range for a limited nonlinear crystal size. Followingly, scanning Sum-Frequence Generation (SFG) cross-correlation

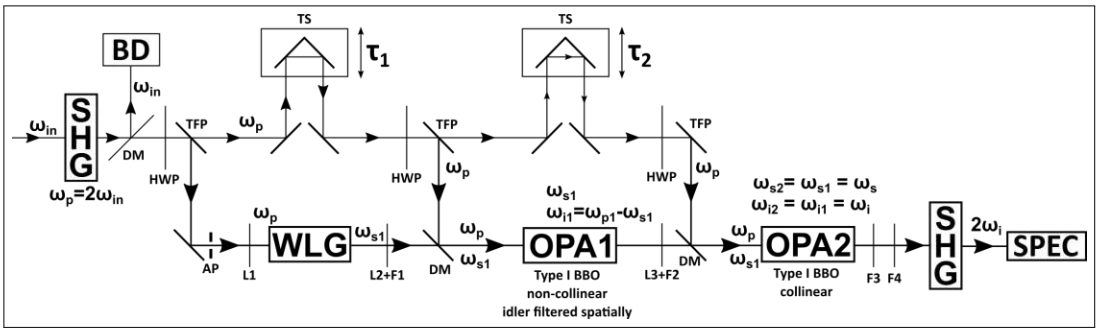

Figure 6.4: Detailled description of the passively CEP-stabilizing two-stage OPA. **SHG:** Second-Harmonic Generation. **BD:** Beam Dump. **DM:** Dichroic Mirror. **HWP:** Half Waveplate. **WLG:** White-Light Generation. **TFP:** Thin-Film Polarizer. **TS:** Translation Stage. **SPEC:** Spectrometer. **BBO:** Beta-Barium Borate. **AP:** Aperture. **Lx:** Lens. **Fx:** Filter.

traces and spectra were acquired in parallel. At first, the measurements were carried out with a single pulse for initial OPA alignment and signal optimization. Then, the procedure is carried out with a burst of 6 pulses and a burst pulse spacing of 1.63 ps. Finally, the burst cavity round-trip time in the twin RA burst channel was adjusted by using a micrometer screw that finely tunes the position of the cavity end mirror. By this, a burst was set to a pulse spacing of 1.99 ps and another measurement was carried out.

6.3.1 Single-Shot Cross-Correlation

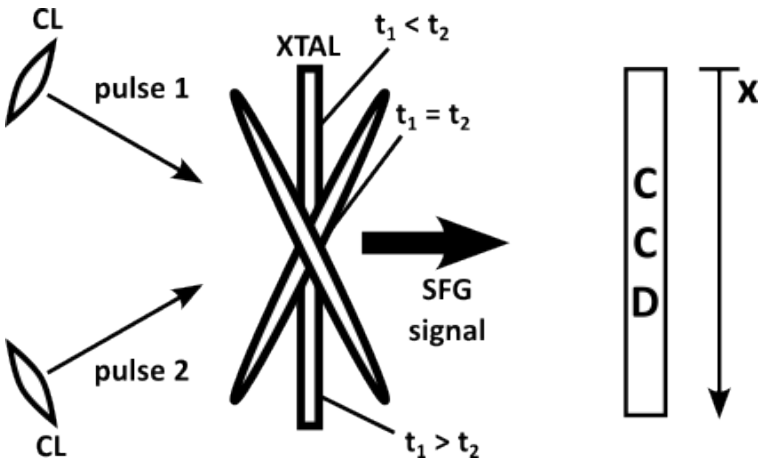

Figure 6.5: Concept to measure picosecond-long waveforms by crossing two pulses under a large angle in a nonlinear crystal, which leads to a time-to-space mapping of the temporal waveform: t_i is the time of arrival of pulse i. Pulse 1 arrives on the top side of the crystal earlier than pulse 2, giving a positive delay. In the middle is the zero-delay overlap. On the bottom side of the crystal, pulse 1 arrives later than pulse 2. Figure adapted from [136, p. 142].

Single-shot characterization techniques are a well-established way to measure the shot-to-shot characteristics of ultrashort pulses. They are used in several realizations, such as in Frequency-Resolved Optical Gating (FROG) measurements [136] or in cross-correlation

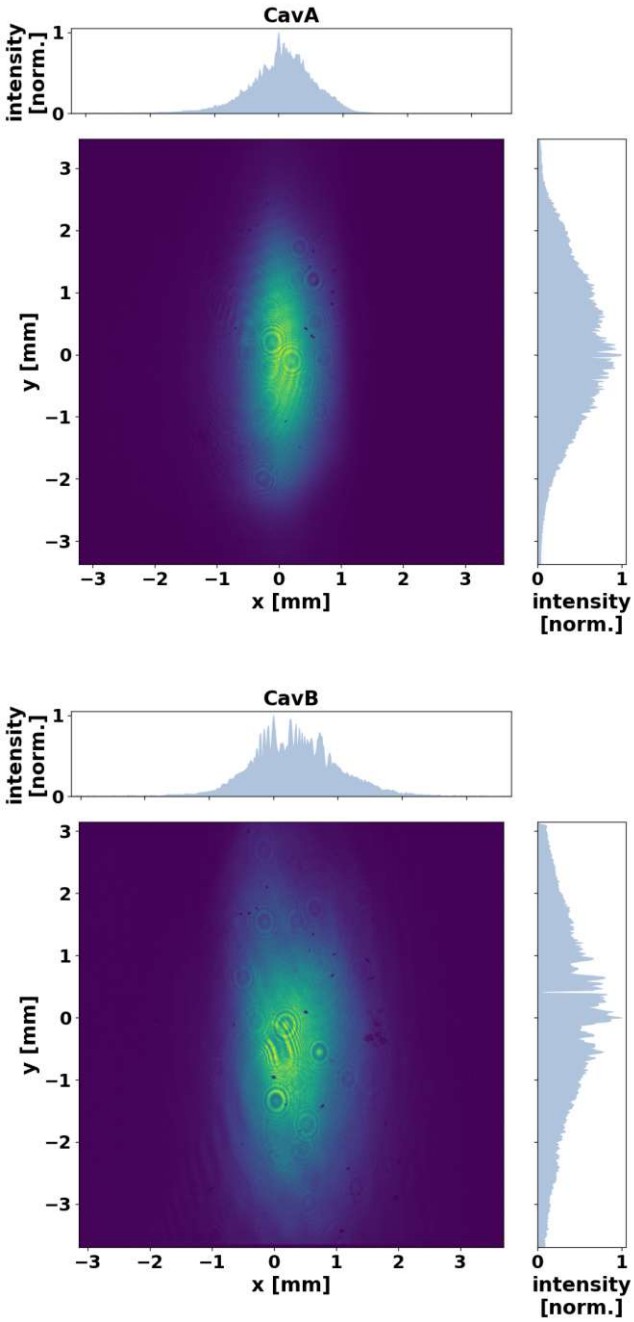

Figure 6.6: Beam spatial profiles measured 10 mm before the crystal.

measurements with a known reference pulse. They allow the characterization of distinct waveforms without the assumption that the individual samples are equal to the ensemble average, which is performed when applying multi-shot techniques. In this section, such a single-shot cross-correlation technique is applied to demonstrate the reproducibility of the NIR burst system by cross-correlating the burst with an amplified compressed reference pulse in a nonlinear crystal under a large angle (See Fig. 6.5). The range of delays $\Delta\tau$ which is covered by such a measurement is [136]

$$\Delta\tau = 2(d/c_0)\tan\theta/c_0, \tag{6.1}$$

with d being the beam diameter in the crystal and c_0 being the speed of light in vacuum.

Inside the crystal, the two pulses generate sum-frequencies at positions, which depend on their time delay. Thus, their temporal delays are translated into spatial positions. To gain enough efficiency for the nonlinear process, the pulses are focussed with a cylindrical lens, that focuses the pulses perpendicular to the axis on which the temporal information is acquired (the x-axis in Fig. 6.5). The x-dependent line profiles containing the temporal waveform information were acquired with a commercial fast CCD line camera (MightexSystems TCE-1209-U) that was triggered synchronously to the 1 kHz amplification repetition rate. The spatial beam profile of both pulse beams need to be broad enough to cover the required delay range (Equ. 6.1). Further, the spatial beam profiles need to be sufficiently smooth, such that spatial inhomogeneities don't deteriorate the signal. This was confirmed by measuring the spatial beam profile 10 mm before the crystal each, where, apart from dirt on the beam profile detector, a smooth spatial profile was observed (See Fig. 6.6).

As a demonstration of the technique, a burst of 4 pulses was generated with a pulse spacing of 1 ps and cross-correlated with the reference pulse in a BBO crystal (6 mm diameter, 0.5 mm thickness). The measurement results for 100 amplification cycles show good reproducibility (Fig. 6.7) and pulse stability. However, as can be seen by looking at individual cross-correlation traces (Fig. 6.8), the first and the last pulses only show about half the intensity in their signal. This could be determined to be due to the limited delay range of the cross-correlation window by tuning one of the mirrors and examining the changes in the cross-correlation trace. Further, an increase in the supported delay range, however, would have required a crystal with a larger diameter than the one already in use (which would have been unnecessarily expensive and was not available at this time in our lab). So while the single-shot approach gives good insights into burst-to-burst amplification dynamics and reproducibility, it lacks the support of longer (> 3 ps) delay ranges with commonly accessible hardware. It does, however, allow confirmation of the shot-to-shot reproducibility and whether a scanning cross-correlation technique is reasonable to apply.

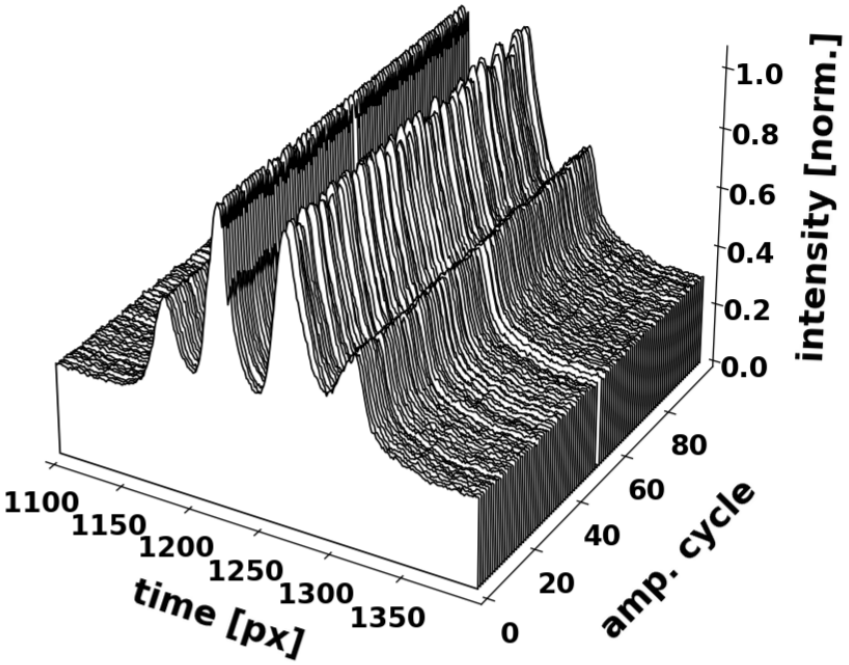

Figure 6.7: Single-Shot cross-correlation traces over 100 amplification cycles. A burst with 4 pulses and 1 ps temporal spacing between pulses was generated and crossed with a single compressed reference pulse for each cycle.

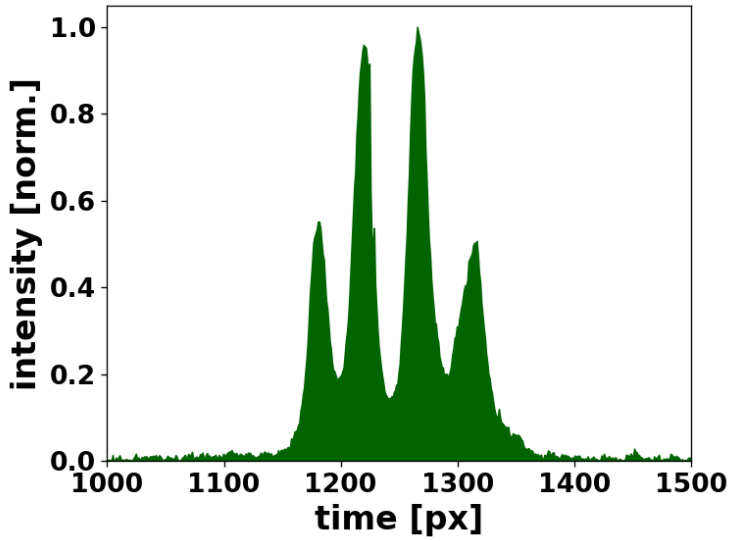

Figure 6.8: Single-Shot cross-correlation trace. A burst with 4 pulses and 1 ps temporal spacing between pulses was generated and crossed with a single compressed reference pulse.

6.3.2 Scanning Cross correlations and spectra

Instead of applying a single-shot technique as in Chapter 6.3.1, one can simply delay one of the two channels with a delay stage and scan the delay over the delay stage position setting, which includes averaging over many cycles. In Fig. 6.9, the results consisting of the scanning cross-correlation traces and spectra of the pump, the WLG seed, the 2-stage signal, and the idler are shown. The pulse duration of 250 fs is confirmed by the cross-correlation measurement. The pulse spacing was 1.63 ps and 1.99 ps in the two burst settings used for the measurement. For the idler, the second harmonic is measured in a single-shot manner with an integration time of 1 ms (Avantes Avaspec-ULS4096CL-EVO) synchronously to the burst amplification repetition rate of 1 kHz. In all experiments, the pump spectrum coming from the phase-scrambled burst has a stochastic structure without any pronounced burst modulation. It is confirmed by the measurement that, as outlined in the section before, the phase scrambling is transferred to both the WLG seed and the signal (Ocean Optics HR4000/HR4000CG-UV-NIR), which thus lacks any sign of periodic modulation with a period according to the pulse spacing. In agreement with the theoretical predictions, the burst idler spectra consist of a clear periodic modulation with high modulation depth resulting from spectral interference of phase-descrambled burst pulses according to their temporal spacing. Burst idler spectral periods can be determined to be 2.1 nm and 1.7 nm, which at 1015 nm (SH of idler) corresponds well to the given pulse spacings of 1.63 ps and 1.99 ps, respectively. As expected for a single pulse, spectral interference modulations are completely absent in its idler spectrum.

6.3.3 Comparison with the theoretical limit

To further confirm the assumption of the origin of the idler spectral modulation, the measured SH idler spectra are compared with an analytical calculation. For a burst of N pulses, the burst spectral intensity can be calculated from Eqs. (1.10, 1.12). From this, a fit for each of the measurements is performed and the results are plotted together with the measured spectra in Fig. 6.10.

Overall, the comparison looks very promising, with a broadening of experimentally measured spectral peaks compared to the theoretically calculated ones: For the short/long pulse spacing case, the peak width (FWHM) was determined to be 320/240 GHz in the measurement compared to 90/80 GHz according to the calculation. This broadening can be explained by the fact, that the idler is angularly chirped which is also the reason why after optimization via alignment of the beam into the spectrometer the central frequency can differ by a few THz. The angular chirp is given by slight non-collinearity between signal and pump in the second stage because of the finite beam size, limiting the alignment. The angular chirp could be estimated to be smaller than 1.1 mrad/m, which in combination with the travel distance to the spectrometer incoupling mirror (0.8 m) and the spectrometer entrance slit (5 um) lead to slight clipping of the SH idler. This effect is noticeable by a change in the measured central frequency from 295.5 THz at 1.63 ps spacing to 294.4 THz at 1.99 ps spacing. Since an angular chirp also leads to time

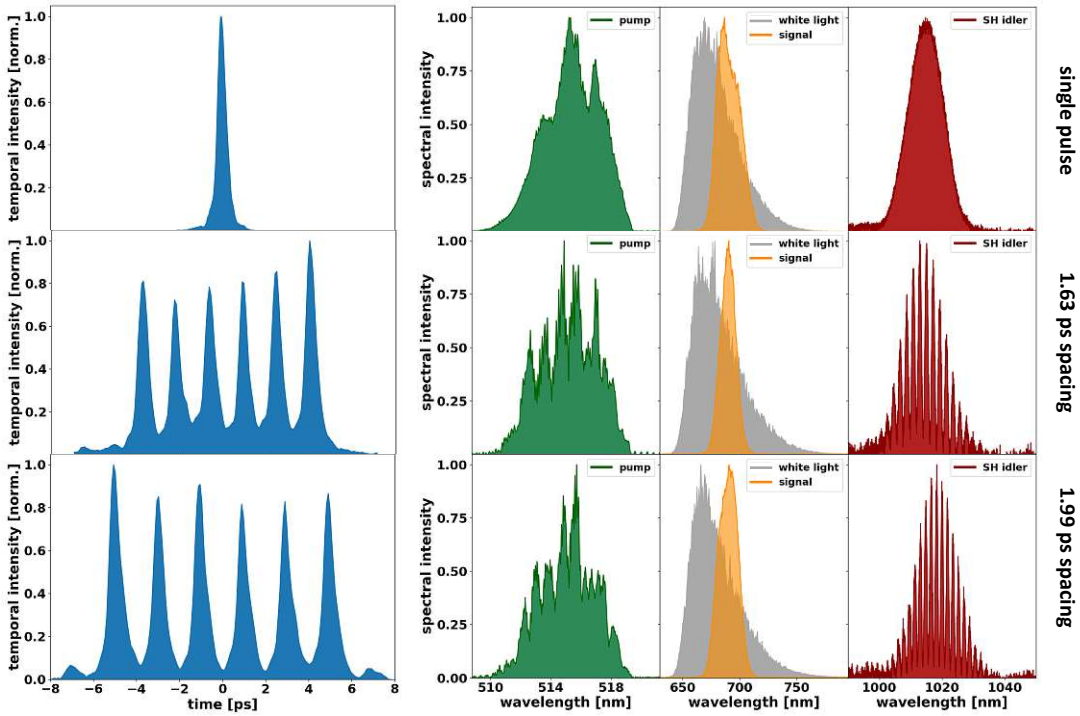

Figure 6.9: Cross Correlations (left, blue) and spectra (other) acquired for a single pulse (top) and a burst of 6 pulses with a temporal spacing of 1.63 ps (middle) and 1.99 ps (bottom). The white-light-generated seed spectrum (light orange) and the second-stage signal spectrum (orange) can be seen. The second-harmonic of the idler signal generated in the second stage (red) is also visible, showing a clean periodic modulation, originating from the phase-descrambling of the burst pulses.

smearing, this smearing effect also explains the broadening of the spectral peaks that are formed by the very short pulse spacing.

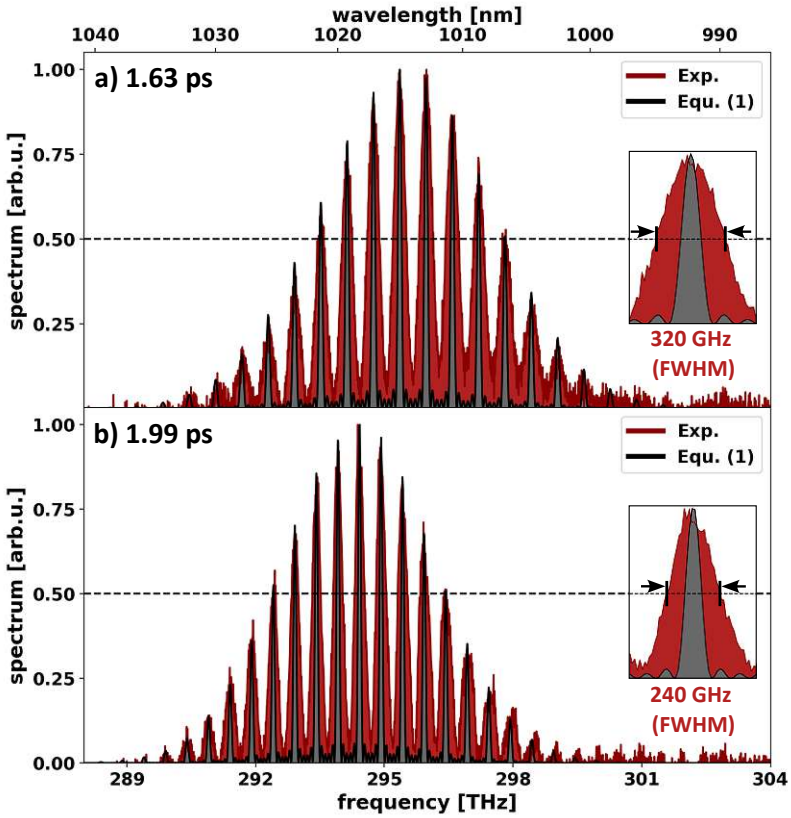

Figure 6.10: Comparison of the measured SH idler spectrum (red) with the calculated fit (black) according to Equ. (1) for a pulse spacing of a) 1.63 ps and b) 1.99 ps.

Chapter 7

Pulse Number Scalability of THz-Rate Bursts

This chapter focuses on the scalability in pulse number of Vernier-type burst generation. A gradual smoothing of temporal intensity profiles at an increasing number of pulses is discovered, demonstrating an unexpected recovery of the CPA performance at terahertz (THz) intraburst repetition rates. A numerical model is developed and its results are analyzed (see Chapter 7.1). An operating regime corresponding to an intrinsic smoothing of the temporal intensity profile of chirped THz-rate bursts is identified at high pulse numbers (See Fig. 7.1c). This burst amplification regime gives a sustainable energy extraction from an amplifier, even at high ($N \gg 10$) pulse numbers without risk of intensity-induced optical damage. Further than that, for burst durations larger than the chirped pulse duration, the extractable energy of an amplifier can be shown to be increased. The experimental setup for an experimental demonstration is described in Chapter 7.2 and its results are shown in Chapter 7.3. A self-referenced stable burst spectral peak structure with megahertz (MHz) peak width is generated, without risk of amplifier damage caused by interference of chirped pulses. In the course of this effort, the time-frequency properties of ultrashort-pulse THz-rate bursts at high ($N \gg 10$) pulse numbers are validated experimentally. For such high pulse numbers the proposed technique combines CPA and Divided Pulse Amplification (DPA) [132] in an unprecedented way and further gives an optimistic outlook on the energy scalability on THz rate bursts with extraordinarily high pulse numbers (See Chapter 7.4). The author notes that parts of this subchapter were already published in a similar form in the author's work [1].

7.1 Numerical results

The Wigner distribution $\mathcal{W}_B(t,\omega)$ for an ultrashort-pulse burst is calculated numerically, according to the definition given in Eq. (1.15), with an intraburst pulse spacing of 1 ps. Depending on the FWHM pulse duration τ_{FWHM} (by variation of the chirp parameter C) and on the compressed burst duration $(N-1)\Delta t$ (by variation of the pulse number N), three regimes can be identified: compressed pulses (250 fs pulse duration), few strongly chirped pulses (200 ps, 10 pulses) and many strongly chirped pulses (200 ps, 80 pulses). Further, only calculations with zero phase slip $\phi_s = 0$ are shown.

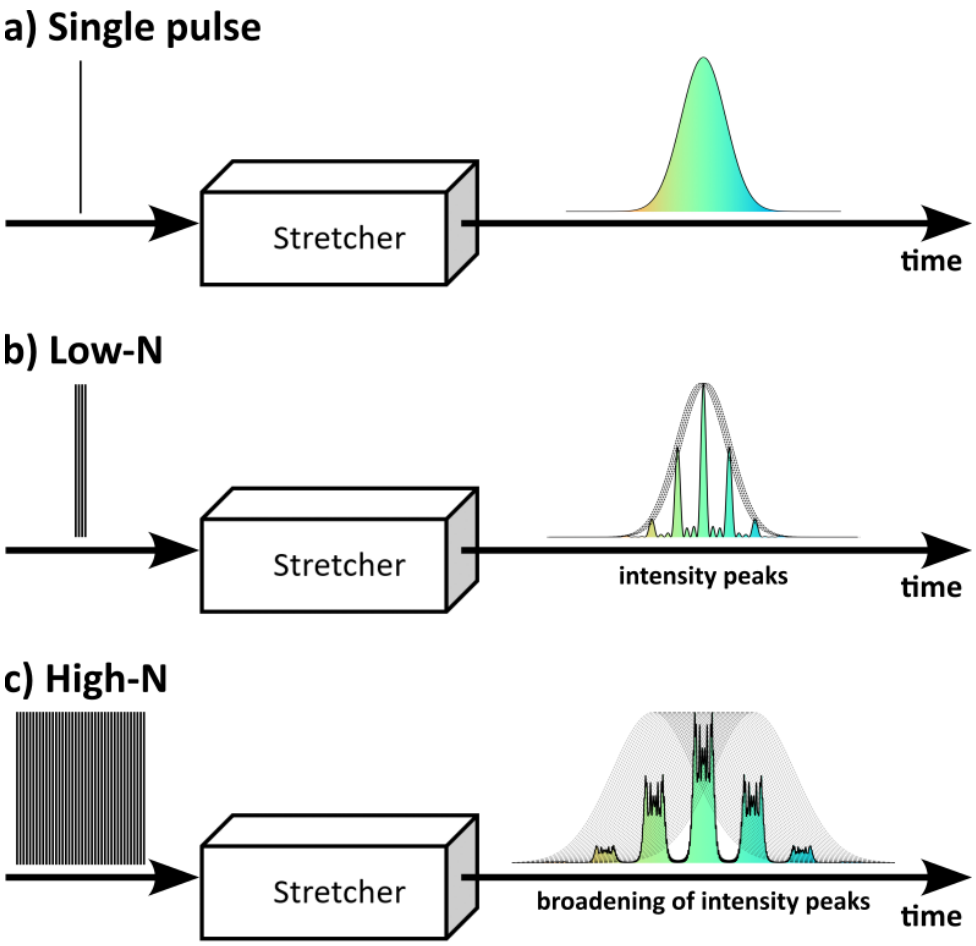

Figure 7.1: **Depiction of the effect of temporal intensity peak broadening for chirped THz-rate bursts at increasing pulse numbers.** After the stretcher, the pulse spacing is much smaller than the chirped pulse duration. The temporal scaling before and after the stretcher differs for visualization purposes. **a) Single-pulse:** High-frequency, blue components advance lower-frequency, red components in time. For a linear chirp, the spectrum is translated into the time domain. **b) Low-N regime:** When chirping only a handful of pulses closely together, burst-typical spectral peaks are mapped into the time domain. **c) High-N regime:** As soon as the pulse number becomes large enough, there is no clear overlap in time of all the pulses anymore. The spectral peaks are not mapped into the time domain and temporal intensity peaks are broadened.

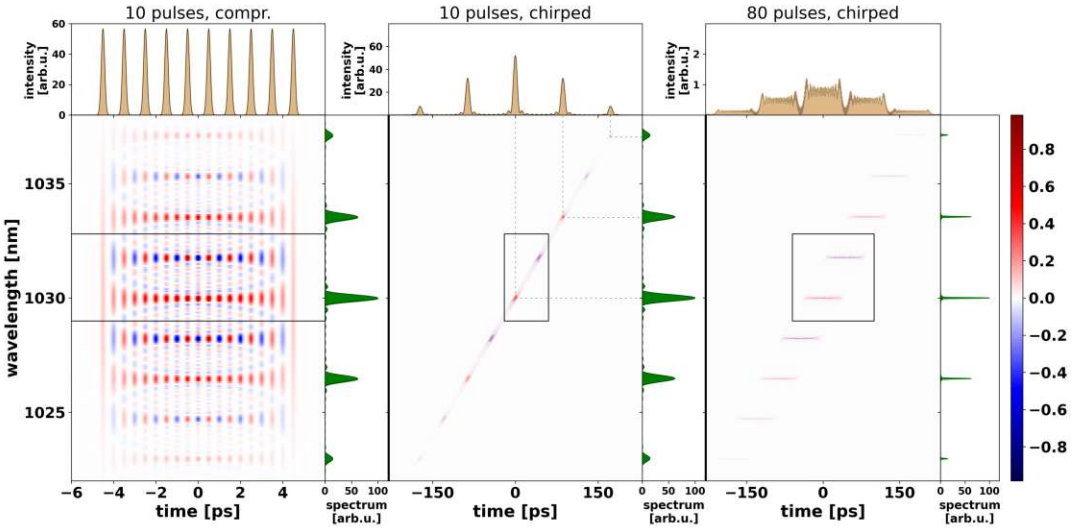

(a) Real part of the Wigner distribution $\mathcal{W}_B(t, \lambda)$ and its marginal distributions (intensity $I(t)$ and spectrum $S(\lambda)$). The mapping between spectral and temporal peaks is marked by dashed lines (middle plot).

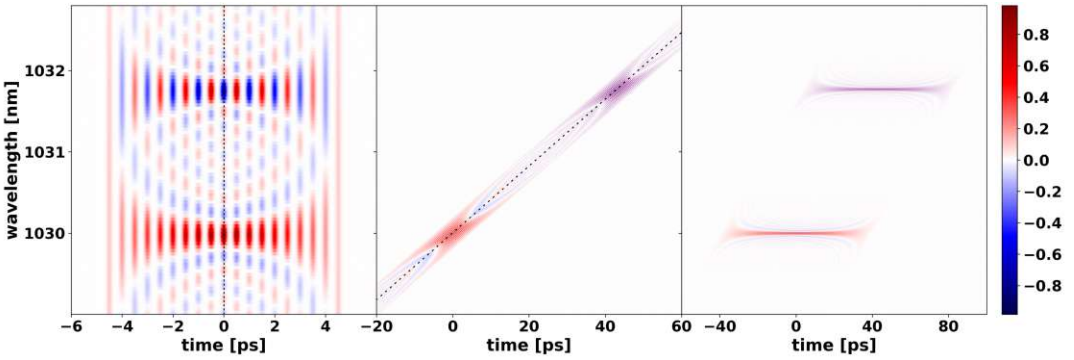

(b) Zoom into the Wigner distribution $\mathcal{W}_B(t, \lambda)$ as indicated by the black rectangles in (a). The symmetry lines of the 10-pulse Wigner distributions are marked by dashed lines.

Figure 7.2: **Numerical Wigner calculation results** consisting of the calculated real part of the Wigner distribution $\mathcal{W}_B(t, \lambda)$ (red and blue) and (a) its marginal distributions, i.e. intensity $I(t)$ (light brown) and spectrum $S(\lambda)$ (green), and (b) zoom into the Wigner distribution for better visualization of the periodic pattern. The results are represented depending on wavelength λ, instead of frequency ω, for a better comparison with the experimental results shown later in this article. Calculations were performed with a burst with 8.5 nm bandwidth at 1030 nm (corresponding to a compressed pulse duration of 250 fs) with a pulse spacing of 2 ps. Left: 4 pulses compressed ($C = 0, \tau_{FWHM} = 250$ fs). Middle: 4 pulses chirped ($C = 1.66 \cdot 10^7, \tau_{FWHM} = 200$ ps). Right: 40 pulses chirped ($C = 1.66 \cdot 10^7, \tau_{FWHM} = 200$ ps).

7.1.1 Compressed Pulses

The chirp parameter C is negligible and the pulse duration τ_{FWHM} is smaller than the pulse spacing Δt

$$C \approx 0, \tag{7.1a}$$

$$\tau_{FWHM} < \Delta t. \tag{7.1b}$$

This is the typically known case before, or after, Chirped-Pulse Amplification (CPA) where all pulses are compressed and well separated from each other in time (Fig. 7.2, left side). For the first ($n = 0$) and last ($n = N - 1$) pulse, the Wigner distribution consists only of non-oscillatory positive-valued signal terms $\mathcal{W}^{(S)}_{B,n=0/n=N-1}(t, \omega)$. For each pair (n, m) of pulses, that are located at times $t^{(S)}_n$ and $t^{(S)}_m$, respectively, exists an oscillating interference contribution $\mathcal{W}^{(I)}_{B,nm}(t, \omega)$ at time [4]

$$t^{(I)}_{nm} = \frac{t^{(S)}_n + t^{(S)}_m}{2}, \tag{7.2}$$

which for $|n - m| = q\Delta t$, q being a positive even number, overlaps with the signal term of another pulse in the Wigner space.
The Wigner interference pattern shows a discrete symmetry along the frequency axis with period $2\pi/\Delta t$. For each period along the frequency axis, interference in the time-frequency Wigner space leads either to a strong spectral peak or to very weak spectral secondary maxima in between, explaining the burst-typical peak structure in the spectrum. For the time-domain marginal, there are no secondary maxima besides the burst pulses. It is noted that the Wigner interference contributions $\mathcal{W}^{(I)}_{B,nm}(t, \omega)$ do have a physical significance and are not a mere mathematical artifact. Their total energy can be shown to be zero because the individual pulse Wigner distributions are time-frequency disjoint (Moyal's formula) [137]. However, they are responsible for the spectral interference structure, which can be measured with any spectrometer with sufficient resolution. Another symmetry property of the Wigner distribution is given by the vertical line at $t = 0$, across which it has an even symmetry $\mathcal{W}_B(t, \omega) = \mathcal{W}_B(-t, \omega)$. This symmetry is given by the fact, that pulses that are equal in their energy are assumed in the calculation. However, it is also preserved for a nonzero phase slip $\phi_s \neq 0$.

7.1.2 The low-N regime: Few Strongly Chirped Pulses

The chirp parameter C is very high. The chirped pulse duration τ_{FWHM} is much larger than the pulse spacing Δt and also even larger than the whole compressed burst duration $(N - 1)\Delta t$

$$C \gg 1, \tag{7.3a}$$

$$\tau_{FWHM} \gg (N - 1)\Delta t > \Delta t \tag{7.3b}$$

As it is generally known for a single pulse [136], the Wigner distribution $\mathcal{W}_{B,chirped}(t,\omega)$ of a chirped burst in this regime (Fig. 7.2, middle) can be seen to be a tilted version of the Wigner distribution of the compressed pulses $\mathcal{W}_{B,compr}$ (Fig. 7.2, left):

$$\begin{aligned}\mathcal{W}_{B,chirped}(t,\omega) &= \mathcal{W}_{B,compr}\left(t - \frac{4\ln(2)C}{\omega_{FWHM}^2}\cdot\omega, \omega\right)\\ &= \mathcal{W}_{B,compr}\left(t, \omega + \frac{4\ln(2)C}{\tau_{FWHM}^2}\cdot t\right)\end{aligned} \tag{7.4}$$

Given this tilt in combination with the even symmetry of the compressed-pulse distribution, the presence of a diagonal symmetry line is given in this case, which is in agreement with the mapping of the spectrum into the time domain. Therefore, the burst intensity $I(t)$ is, up to a chirp-dependent factor $a(C)$ in the argument, well represented by the burst spectrum $S(\omega)$

$$I(t) \propto S\left(a(C)\cdot t\right). \tag{7.5}$$

This is confirmed by the numerical calculations, as can be seen by comparing the Wigner marginal distributions of Fig. 7.2, middle.

7.1.3 The high-N regime: Many Strongly Chirped Pulses

The chirp parameter C is very high. The chirped pulse duration τ_{FWHM} and, due to the large number of pulses N, the compressed burst duration $(N-1)\Delta t$ are both much larger than the pulse spacing Δt

$$C \gg 1, \tag{7.6a}$$

$$\tau_{FWHM} \gtrapprox (N-1)\Delta t \gg \Delta t \tag{7.6b}$$

In this regime, the diagonal symmetry of the chirped low-pulse Wigner distribution is broken due to many chirped-pulse replicas along the horizontal/time axis. When presenting the data while covering a large coordinate range (Fig. 7.2, right), the Wigner distribution can be seen to consist of horizontally spread contributions. When taking a closer look at the individual contributions, each contribution consists primarily of diagonal, closely spaced lines (Fig. 7.2b, right). Wigner signal and interference contributions are hardly distinguishable at this point. Performing the horizontal sum over time to acquire the spectrum, the contributions can be either attributed to signal and constructive interference terms (only positive lines, lower contribution in Fig. 7.2b, right), retaining the strong spectral peaks, or, to signal and destructive interference terms (positive and negative lines, upper contribution in Fig. 7.2b, right), suppressing the spectral density in between the peaks. The intensity distribution in time is smoothed out by interference in the time-frequency Wigner space and thus the CPA technique is a useful way to amplify ultrashort-pulse bursts safely without amplifier damage.

Energy scalability of the high-N regime

Interpulse interferences between strongly chirped pulses lead in the low-N regime to an overshoot of the chirped burst temporal intensity profile. The high-N regime allows for a self-smoothing effect. In this section, this phenomenon is investigated numerically, with the focus on how much energy can be extracted from an amplifier per amplification cycle, under equal conditions, compared to single-pulse operation when the only limitation is a peak-intensity-induced optical damage threshold I_{THR}. The reachable burst energy ϵ_B is compared with that of a single pulse ϵ_P at a given intensity threshold I_{THR}:

$$\frac{\epsilon_B}{\epsilon_P} = \frac{\int I_B(t)dt}{\int I_P(t)dt}, \tag{7.7}$$

which gives the burst-extractable amplifier energy normalized to single-pulse operation. $I_B(t)$, $I_P(t)$ are the chirped intensity profiles of a burst and a single pulse, respectively, and $\max\{I_B(t)\} = \max\{I_P(t)\} = I_{THR}$.
The results of the numerical investigation can be seen in Fig. 7.3 where, depending on the number of pulses N, the normalized extractable energy of bursts with pulses chirped to 200 ps and an interpulse spacing of 1 ps (corresponding to a 1 THz burst rate) is shown. For less than about 10 pulses, a $1/N$ decrease is given. This refers to an N-times increase in peak intensity of the chirped temporal intensity profile. This is the same behavior as from the spectral peak intensity, as can be calculated from Eq. (1.10). This indicates the discussed frequency-to-time mapping of the spectral peak structure and the absence of the temporal self-smoothing effect. At $N \gtrapprox 10$, a continuous increase in the normalized extractable energy can be observed, which is given by the onset of the self-smoothing of the temporal intensity profile of the chirped burst.

7.2 Experimental Setup

The motivation is to directly measure the increasing effect of temporal intensity smoothing in THz-rate bursts of chirped pulses, arising when raising the number of pulses to $N > 10$ pulses. For this, μJ bursts with 1.8 ps spaced pulses (corresponding to a 0.56 THz burst rate) at various pulse numbers are generated and characterized. An overview of the experimental setup is given in Chapter 7.2.1. For this experiment, the self-referenced method to stabilize the pulse-to-pulse phase slip ϕ_s (See Chapter 2.4.2) is applied. Spectrogram measurements of the chirped burst by cross-correlation with the synchronous, compressed reference pulse are shown in Chapter 7.2.2. Finally, the compressibility of the burst waveform by autocorrelation and techniques for optimization of the burst generation process is described in Chapter 7.2.3.

7.2.1 Ultrashort-Pulse Burst Laser System

The experimental setup is based on the same system as described in Chapter 4. In contrast to the efforts outlined in Chapter 6, CPA of ultrashort-pulse bursts does not require any

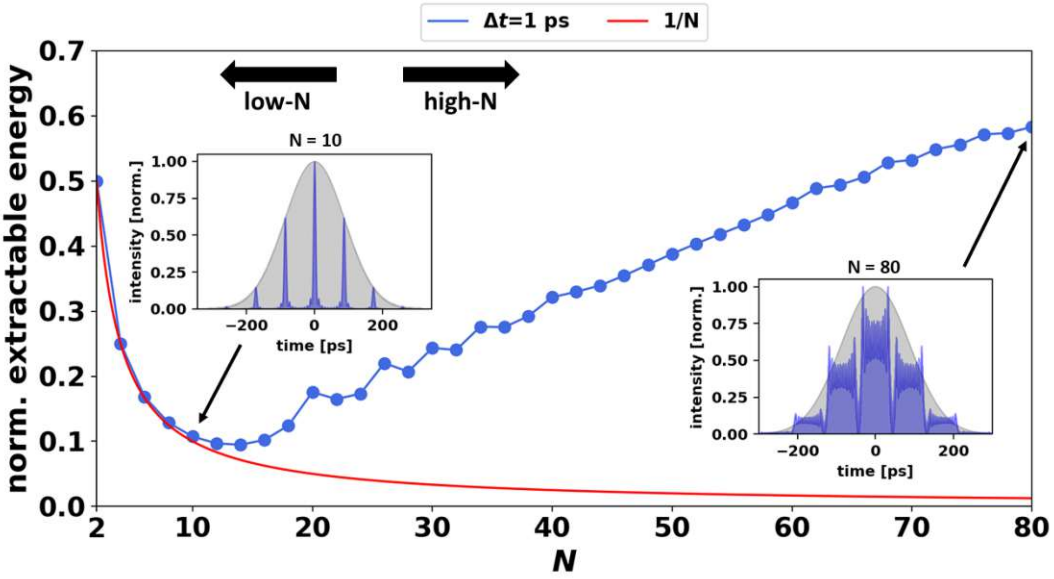

Figure 7.3: **Normalized extractable energy from an amplifier** at 1 ps interpulse spacing, corresponding to 1 THz burst rate, versus pulse number N (blue). The black solid line shows the $1/N$ scaling behavior that would apply in the absence of the self-smoothing effect. The inlays show the temporal intensity profile (blue) of chirped bursts at $N = 10$ (upper left) and at $N = 80$ (lower right) and that of a single chirped pulse (grey), normalized to the intensity threshold I_{THR}. Pulse parameters: $C = 1.66 \cdot 10^7, \tau_{FWHM} = 200$ ps

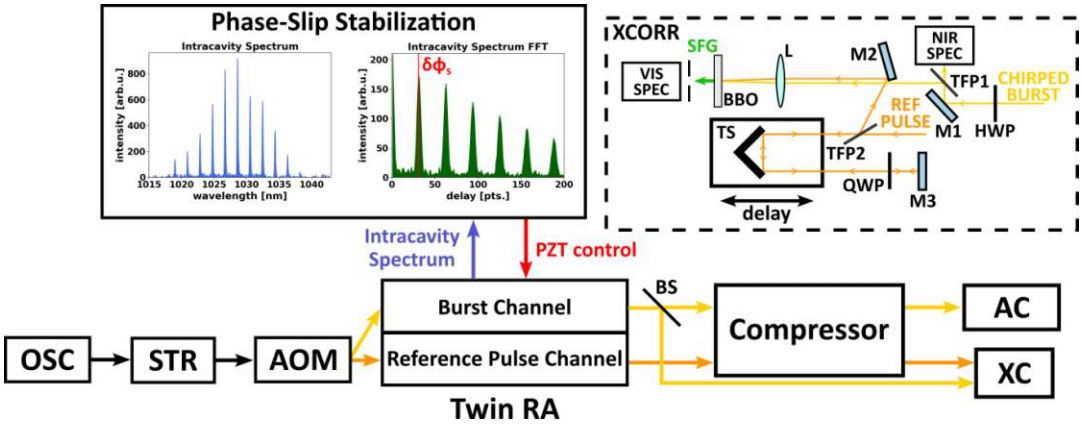

Figure 7.4: **Overview of the experimental setup** with a Twin Regenerative Amplifier providing two channels: The burst channel (yellow) and the reference pulse channel (orange). The upper left inlay shows the intracavity spectrum of 40 pulses (blue) and its Fourier Transform (green) including the reference phase (red). The upper right inlay shows the cross-correlation setup in detail. **OSC:** Oscillator. **STR:** Stretcher. **AOM:** Acoustic-Optical Modulator. **RA:** Regenerative Amplifier. **AC:** Auto-Correlation setup. **XC:** Cross-Correlation setup. **TFP1/2:** Thin-Film Polarizer. **TS**: Translation Stage. **QWP:** Quarter Waveplate. **HWP:** Half Waveplate. **M1/2**: Mirror. **L:** Lens. **BBO:** Beta-Barium Borate Crystal. **VIS SPEC:** Visual Spectrometer. **NIR SPEC:** Near-Infrared Spectrometer.

phase-modulation techniques (phase scrambling) due to the smoothing of the temporal intensity peaks in the high-N regime (Fig. 7.2 right, Fig. 7.3).

7.2.2 Spectrogram Measurements of the Chirped Burst

The chirped amplified burst is cross-correlated (**XC**) with the compressed reference pulse quasi-collinearly (2°crossing angle) in a type I Beta-Barium Borate (BBO) crystal and the sum-frequency generated (SFG) spectrogram (**VIS SPEC**, Ocean Optics HR4000CG-UV-NIR) is measured, i.e. the spectrum of the SFG signal for each burst-reference time delay point (See Fig. 7.4, upper right inlay). The SFG spectrogram is given as [4]

$$\mathcal{S}_E^{(SFG)}(t,\omega) = \left| \int E_B(t')h(t-t')\exp\left(i\omega t'\right)dt' \right|^2 \tag{7.8}$$

with $h(t)$ being a window function, which is given by the compressed reference pulse with 250 fs duration $\tau_{FWHM,ref}$. The spread of the window function $h(t)$ is much smaller ($\tau_{FWHM,ref}$ = 250 fs) than the temporal spacing in all pairs of interfering pulses ($\geq \Delta t$ = 1.8 ps), therefore, interference terms that arise in the burst Wigner distribution are strongly attenuated in the spectrogram. Summation over the wavelength axis gives the time-dependent intensity of the chirped burst waveform. Due to the large duration of the 300 ps chirped pulses, a long-range, high-precision translation stage is used in a double-pass configuration by a combination of thin-film polarizer, quarter waveplate and back-reflecting mirror, to allow for an 800 ps temporal range with 1 ps step size.

7.2.3 Compressed Burst SHG Auto-Correlations

Second Harmonic Generation (SHG) autocorrelation measurements (**AC**) of the compressed ultrashort-pulse burst are performed with a nonlinear type I BBO crystal. This way, the compressibility of the burst pulses is shown, without interpulse crosstalk that distorts the phases of individual amplified pulses. This measurement is also used to set the proper settings for the burst generation process: The optimal PC intermediate voltage can be found primarily by two measures

- When looking at the burst spectrum, the ratio of spectral peak height and the spectral background in between the maxima is maximized while keeping the energy constant.
- The envelope of the AC should, at its best, be triangular.

This way, it is made sure that for a given gain a number of N amplified pulses with equal energies are generated.

7.3 Experimental results

First, the cross-correlation method is validated by comparing the result for a single chirped pulse with its spectrum (Chapter 7.3.1). Then, measurements are performed for ultrashort-pulse bursts with 20 pulses up to 40 pulses (Chapter 7.3.2). Finally, performance data of the phase slip stabilization (Chapter 7.3.3) and the autocorrelation of the compressed burst (Chapter 7.3.4) are shown.

7.3.1 Cross-Correlation Validation with a Chirped Single Pulse

To validate the cross-correlation measurement, the measured temporal intensities of a 300 ps chirped single pulse are compared with its spectrum since it is expected that they are equal to each other for such large chirp parameters ($C > 10^7$). This confirms a good spatial overlap of both channels within the BBO crystal over the whole multiple-100 ps travel range. The result can be seen in Fig. 7.5. The spectrum of the original near-infrared (NIR) chirped pulse, is well reproduced by the temporal intensity distribution. Both, the temporal intensity profile and the directly measured spectrum show a periodic modulation structure introduced by the etalon effect in the intracavity air-spaced waveplate. In the spectrogram, the primarily linear chirp is visible, also the chirped pulse duration of 300 ps is confirmed by the time-dependent intensity.

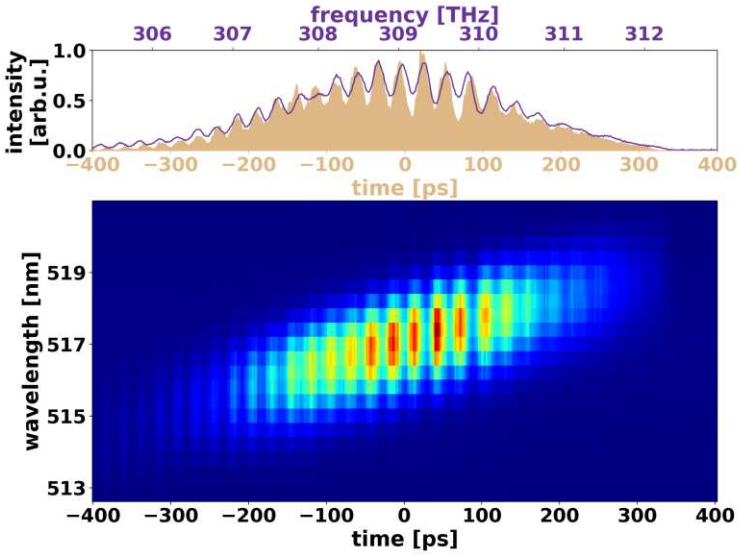

Figure 7.5: **Measured spectrogram of a chirped single pulse** by SFG cross-correlation with the compressed reference pulse. Top panel: Intensity over time (brown) acquired by summation over the wavelength axis for each delay point, in comparison with its spectrum (violet).

7.3.2 Cross-Correlation of Chirped Bursts with a Compressed Reference Pulse

The gain is set to a given value to get sufficient signal on the SFG spectrometer and in the autocorrelation. For this, bursts with an intraburst pulse spacing of 1.8 ps are

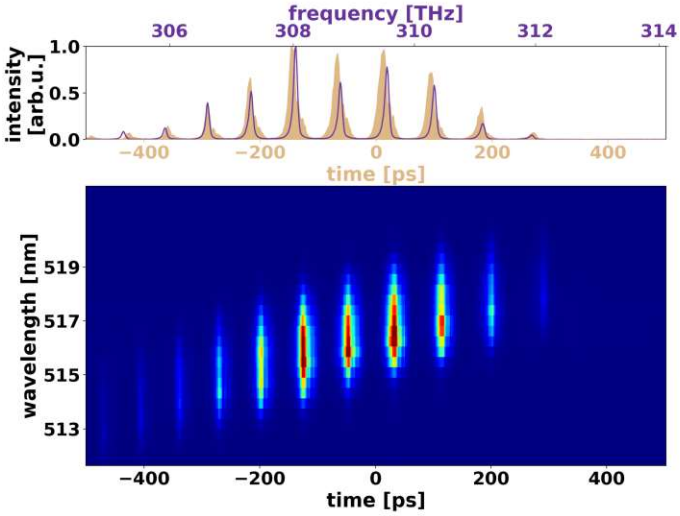

(a)

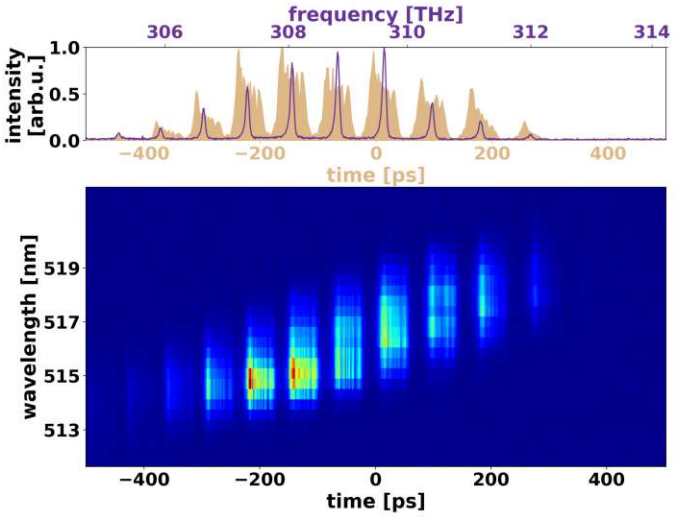

(b)

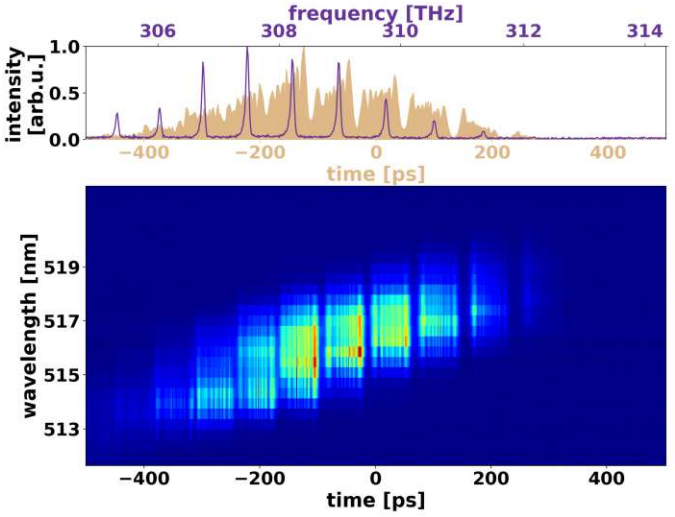

(c)

Figure 7.6: **Measured spectrogram of bursts** consisting of **(a) 20 (b) 30 (c) 40 chirped pulses** by SFG cross-correlation with the compressed reference pulse. Top panel: Intensity over time (brown) acquired by summation over the wavelength axis, in comparison with its spectrum (violet).

generated, corresponding to a 0.56 THz burst rate. The burst and the reference are amplified to about 10 μJ each, and optimized the PC intermediate voltage as described in Chapter 7.2.3. The phase slip stabilization was then turned on. This procedure was done after every time the burst seed pulse number was set by the AOM electronics and the burst accumulation time window in the burst RA channel was adjusted accordingly. Measurements were performed from 20 pulses up to 40 pulses in 5-pulse steps.

The cross-correlation spectrograms, together with the temporal intensities acquired by summation of the spectrogram data over the wavelength axis are shown in Fig. 7.6 for 20, 30 and 40 pulses, including a comparison of the acquired temporal intensities with the NIR burst spectra. For 20 pulses (Fig. 7.6a) one can see a good agreement of the intensities with the spectra, as it is the case for a single pulse (Chapter 7.3.1). This is an indication that for 0.56 THz rate bursts with 20 pulses, which are chirped to 300 ps, one is still in the low-N regime, as discussed in Chapter 7.1.2. The spectrogram shows, in contrast to the numerically calculated Wigner distributions (Fig. 7.2, middle) only a signal at delay times where peaks in the temporal intensity are visible. In between, no interference structure was recorded. This is in agreement with the formulation of the spectrogram as a smoothed version of the Wigner distribution, where the interference terms are suppressed by a short temporal window. When further increasing the pulse number (Figs. 7.6b, 7.6c), a gradual intrinsic smoothing of the signal in time over the whole bandwidth in the spectrogram is visible, which also leads to a smoothing of the time-dependent chirped-burst intensity. In Fig. 7.7, the number of 20 pulses seems to be indeed the threshold between the low-N and the high-N regime in this particular case, until at 40 pulses the temporal intensity profile is completely smoothed out. It is underlined that the high-N regime thus serves for the optimal conditions for CPA.

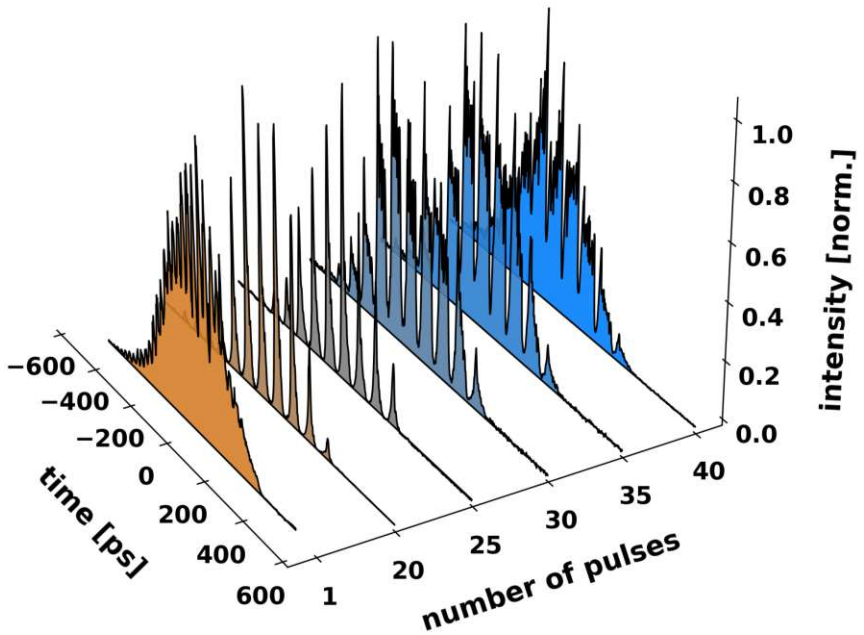

Figure 7.7: **Temporal intensity profiles of chirped bursts** acquired from the measured spectrograms by summation over the wavelength axis, shown for a single pulse and for multi-pulse bursts with 20 up to 40 pulses.

7.3.3 Phase-Slip Stabilization

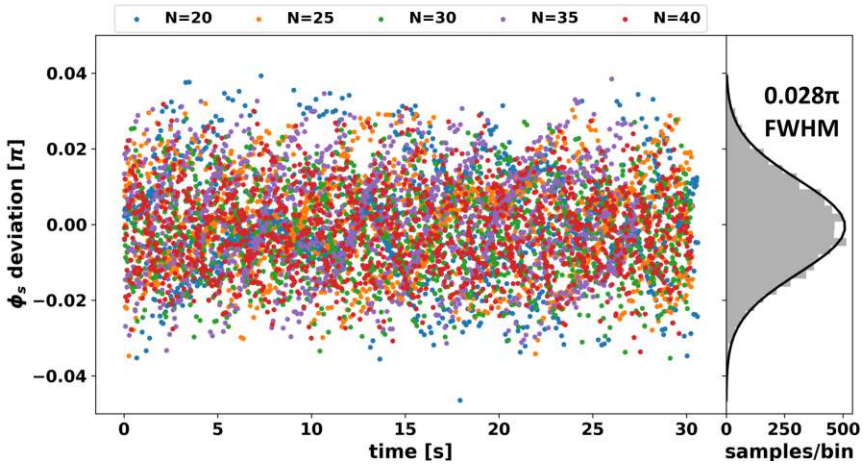

Figure 7.8: **Time-dependent deviation of the phase slip** ϕ_s from an arbitrary target value for 20 up to 40 pulses. On the right side, the stochastic distribution by summation of all data points over time (gray) is shown, including a Gaussian fit with a 0.028π FWHM width (black).

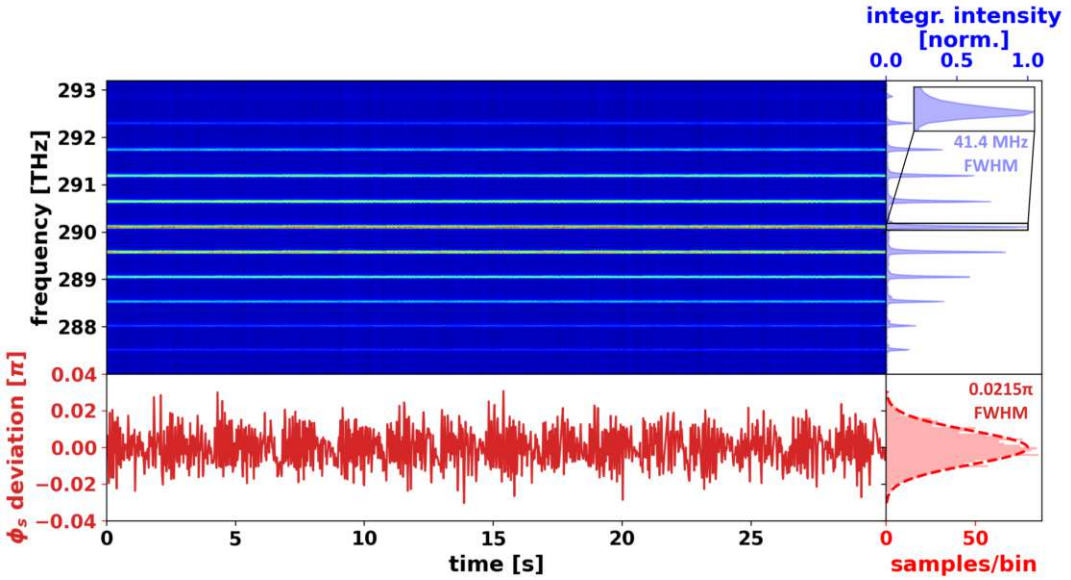

Figure 7.9: **Intracavity spectrum from the RA burst channel cavity** over time (top) and the derived time-dependent deviation of the phase slip ϕ_s (bottom).

In the following, the self-referenced phase-slip stabilization performance for this measurement is shown. It is implemented as described in Chapter 7.2. The stabilization data was recorded in parallel to the acquisition of the cross-correlation data (see Chapter 7.3.2). In Fig. 7.8, the measured deviation of the phase slip ϕ_s over time can be seen. The stochastic distributions of the time-dependent deviations do not depend strongly on the pulse number, which is why all data points were summed up over the time axis. The total phase deviation distribution is Gaussian with an FWHM width of 0.028π, which corresponds at 1030 nm to an FWHM group delay deviation of only 48 as in the pulse

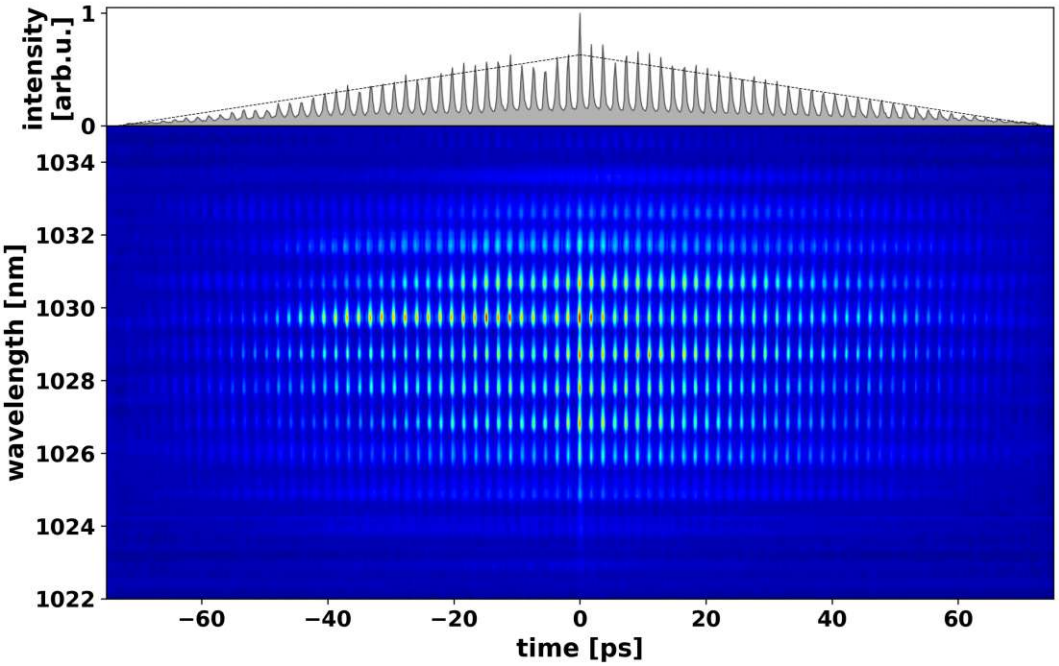

Figure 7.10: **Characterization of a 40-pulse 0.56 THz burst at μJ level**: The burst consists of compressed pulses with 250 fs pulse duration. The SHG FROG trace (bottom) and the derived autocorrelation by summation over the wavelength axis (top). The dashed line shows the triangle envelope of the peak maxima (ignoring the zero-delay artifact).

spacing. The phase-slip stabilization performs well even at high pulse numbers. For 40 pulses, the intracavity spectrum over time and its derived phase deviations are plotted in Fig. 7.9. A guided PZT with a 40 μm travel range (Piezosystem Jena PU 40) is used. This travel range is much larger than the 14.4 nm translation that would correspond to the measured FWHM width of the phase deviation distribution. A main factor for the stochastic width of the phase deviation is given by the limited control loop bandwidth. The slow control loop was running software-controlled with a mean sample rate of 49 Hz, which could be easily improved by applying a fast hardware-running control loop in the future. Because of the good stability of the phase slip, the peak structure in the burst spectrum can be seen to be very stable.

7.3.4 Autocorrelation of the Compressed Burst

The compressibility of the burst pulses is shown by the demonstration of SHG autocorrelation results for compressed bursts, which in the case of N pulses is supposed to show $2N-1$ signal peaks. The result for 40 pulses can be seen in Fig. 7.10, including the SHG FROG trace from which the autocorrelation is derived. The SHG FROG trace proves further the phase slip control stability by a stable peak structure over time without any noticeable wavelength-detuning drift. The autocorrelation can be seen to be typical for a complex waveform with a broad background component and a coherent artifact [138, 139], visible by the overshoot at zero time delay. The peak maxima can be approximately fitted with a triangle-shaped line, indicating equalization of the burst pulse energies. Deviations

from the ideal triangle course do not only arise because of the pulses themselves but also because of the set time delay step of 200 fs of the delay stage that is comparable to the compressed pulse duration of 250 fs, leading to discretization errors. Nonetheless, this delay step value is found to be a good trade-off between step size and a large, almost 160 ps, scan range for this proof-of-concept experiment. It is also noted, that bursts with any higher pulse number can be easily generated with the described method, however, due to limited scan range and signal-to-noise ratio (SNR) in the AC, higher pulse numbers than 40 were not reasonable for the given demonstration. The theoretical limit of the burst duration is given by the RA burst channel cavity round-trip time, which is approximately 13 ns in this case (corresponding to the 76 MHz oscillator repetition rate). This would correspond to a burst of 13,000 pulses at a 1 THz burst rate.

7.4 Outlook on Energy Scalability for Extraordinarily High Pulse Numbers

The primary focus of this chapter is to investigate, both numerically and experimentally, the onset of the high-N regime given by the intrinsic self-smoothing of the chirped temporal intensity profile. In order to give a further outlook on the capabilities given by direct time-domain generation of bursts and the self-smoothing phenomenon at THz burst rates, the normalized extractable energy at pulse numbers $N \rightarrow 1000$ at a 1 THz burst rate is investigated (Fig. 7.11).

A partial periodic revival of the temporal peak structure at every 90 pulses is visible, i.e. at $N = 100$, $N = 190$, $N = 280$, ..., which is indicated by a decrease in extractable burst energy. The energy decrease due to the partial peak revivals, however, becomes less the higher the number of pulses. In consequence, normalized extractable energy keeps increasing for sufficiently many pulses, until it becomes linearly dependent on the pulse number N.

For sufficiently large N, the largest interpulse spacing $(N-1)\Delta t$ (that is the spacing between the first and the last burst pulse) becomes larger than the duration of the individual chirped pulses τ_{FWHM} (200 ps in this simulation). In this case, the burst-extractable energy is higher than the extractable energy with a single pulse under the same conditions. This can be well understood when considering the temporal intensity profile of a chirped burst with $N \rightarrow 1000$, or more, as shown in Fig. 7.12 with $N = 2000$ pulses. In this case, there is a 10 times higher maximum interpulse spacing than the chirped pulse duration. The intensity profile of a strongly chirped THz-rate burst almost completely fills out the intensity-time area, resembling a waveform with a rectangular shape. It also exceeds the temporal range of the single stretched pulse and thus allows for higher energies at a given chirp rate C. When zooming into the waveform (right subplot of Fig. 7.12), a periodic temporal peak structure can be observed, with a period equal to the interpulse spacing Δt. The reason for the normalized extractable energy increase is similar to that of Divided Pulse Amplification (DPA) [132]. In DPA, the total amplified energy is distributed over time over multiple compressed pulses, while peak intensity is kept below a given damage

threshold. We note, that the regime $N \to 1000$, or higher, thus includes advantages of DPA and CPA.

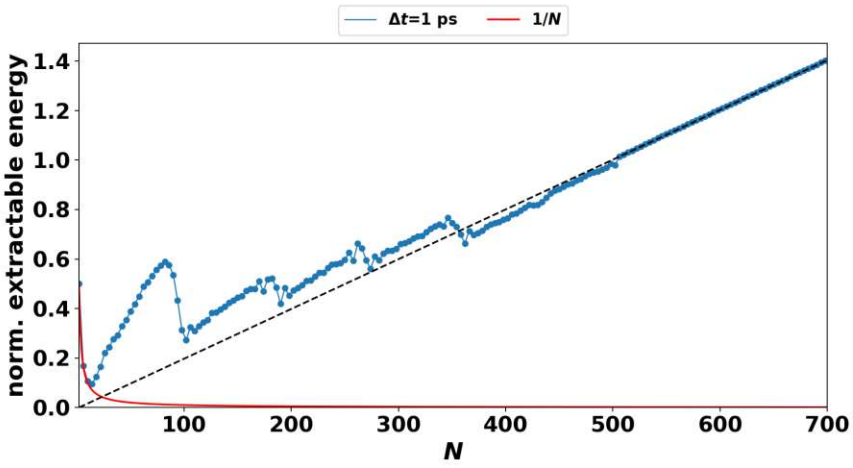

Figure 7.11: **Normalized extractable amplifier energy for burst-mode operation compared to single-pulse operation** depending on pulse number N, at a given intensity damage threshold I_{THR}. The black solid line shows the $1/N$ scaling behavior that would apply in the absence of the self-smoothing effect. The dashed line in black indicates when the maximum interpulse spacing $(N-1)\Delta t$ becomes larger than the duration of an individual chirped pulse τ_{FWHM}. Pulse parameters: $C = 1.66 \cdot 10^7, \tau_{FWHM} = 200$ ps.

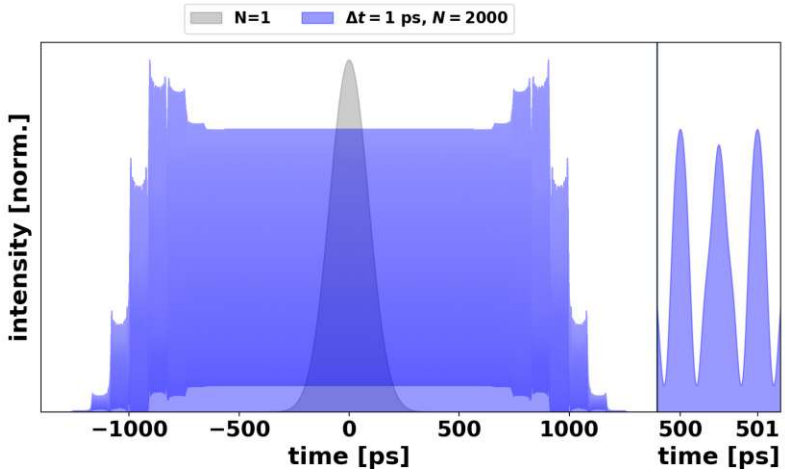

Figure 7.12: **Normalized temporal intensity profile of the chirped waveform** in the case of a single pulse (grey), $N = 2000$ pulses spaced by $\Delta t = 1$ ps (light blue). Pulse parameters: $C = 1.66 \cdot 10^7, \tau_{FWHM} = 200$ ps.

Chapter 8

Rapid-Scan Nonlinear Time-Resolved Spectroscopy over Arbitrary Delay Intervals

The ability of a controlled time delay between two optical pulses is a fundamental necessity for time-resolved measurements, which allow for the understanding of a system's time-dependent behavior. In Ramsey-comb Spectroscopy, controlled time delays lead to the acquisition of spectra with comb accuracy and resolution while using pulse pairs at millijoule energies [140]. Biomolecular dynamics and charge recombination in photovoltaic devices show characteristics over several orders of magnitude on timescales from picoseconds to microseconds [141, 142]. Further research of these kinds of phenomena requires the development of optical sources with a stable, controlled time delay over a wide temporal range. This chapter is dedicated to this task: Chapter 8.1 describes the state of the art of tunable delay generation for pairs of ultrashort amplified pulses. In Chapter 8.2, the operation of an ideal tunable delay system is described. An experimental setup that comes quite close to the ideal system and was built up is outlined in Chapter 8.3. Finally, the experimental results are presented in Chapter 8.4, including a transient-absorption pump-probe measurement of a perovskite sample over a large dynamical range with adaptable temporal resolution.

8.1 State of the Art

In general, the current technical state requires a tradeoff, where one either needs to decide between femtosecond precision in a small nanosecond scan range, or a high microsecond scan range with only picosecond, or even worse, precision. An overview is given in Tab. 8.1.

The most typical approach for setting a time delay of two pulses, is using a mechanical delay stage (Fig. 8.1). This method has the properties of high versatility and simplicity since it consists only of a retroreflector and a translation stage. However, its application over a larger temporal range, which exceeds several dozens of picoseconds, leads to lateral beam pointing instabilities and defocussing effects. Tuning the position of the retroreflector also requires a certain amount of time, leading to comparably slow scan speeds. This

Table 8.1: Selected methods with their primary working principle to generate tunable delays between two pulses.

Control over Time Delay				
Delay Stage	ASOPS	Bredenbeck et al.	kHz-ADASOPS	This work
Retroreflector Position	Detuned and Locked Rep. Rate of OSC Pair	$< 1/f_{rep}$: as ASOPS $> 1/f_{rep}$: AMP triggering	No control	Dual-Comb OSC + AMP triggering

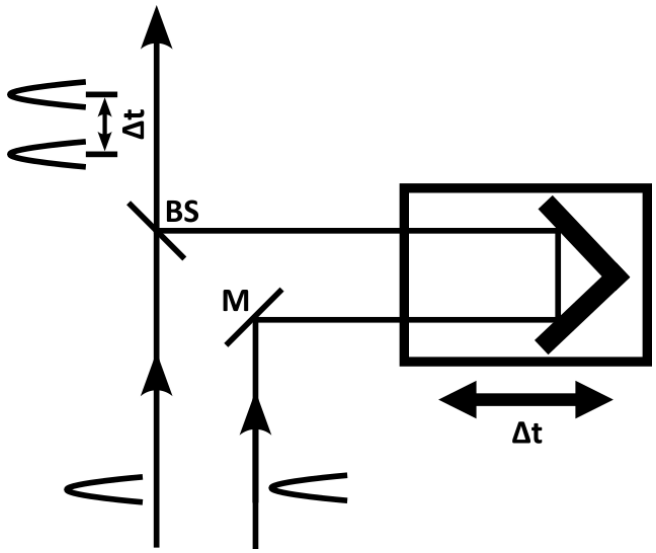

Figure 8.1: Concept of applying a delay stage to generate a tunable time delay between two pulses. **M:** Mirror. **BS:** Beam Splitter.

makes the use of a mechanical delay stage unattractive for e.g. microscopic applications, where not only one but multiple pump-probe traces are recorded, one for each position or pixel.

Thus, it became clear that for fast and accurate time-delay settings, suitable electronically tunable methods without moving optical arms need to be found. The emergence of femtosecond dual-comb sources led to a broad palette of applications in frequency metrology and linear Fourier domain spectroscopy. It allows for a continuous sampling of the time interval between pulse pairs. While in certain configurations it is commonly known as Asynchronous Optical Sampling (ASOPS), the general concept is shown in Fig. 8.2 [143, 144]: It is based on the synchronization of two mode-locked oscillators, each with a given repetition rate $f_{rep,1}, f_{rep,2}$, such that their repetition rate detuning $f_{rep,2} - f_{rep,1}$ is constant. A stable repetition rate detuning between two combs generates a time delay that scans continuously between zero delay interval and the repetition time, with a step size that is given by $|1/f_{rep,2} - 1/f_{rep,1}|$. This makes fast and simple acquisition of pump-probe data with fs precision possible. However, the technique's outstanding performance is only available for time delays up to the oscillator repetition time which typically means a few dozen nanoseconds.

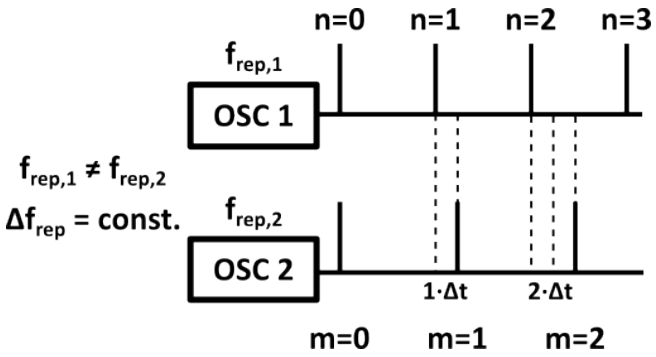

Figure 8.2: Concept of ASyncronous Optical Sampling (ASOPS) to generate a tunable time delay between two pulses.

The challenge to extend the dynamical range was taken by Bredenbeck et al. [145] where by means of two synchronized oscillators together with two individually triggered amplifiers, a dynamical range up to the amplifier repetition period was achieved. The oscillators are locked in a master-slave configuration, where the photodiode-acquired pulse signals are combined in a mixer whose output controls the round-trip time of the slave oscillator. Fine-tuning of the time delay below the oscillator round-trip time is achieved by setting a phase-shifter between the slave photodiode and the mixer. Coarse-tuning can be done by shifting the RA triggers by an integer multiple of the oscillator round-trip time. However, temporal resolution is limited to $<$1.8 ps due to synchronization jitter between the oscillators. Further, the method requires that the oscillators have comparable repetition rates, with one of them being needed to be controllable (e.g. by a movable intracavity mirror).

High scan range methods with higher precision can be realized when dropping the

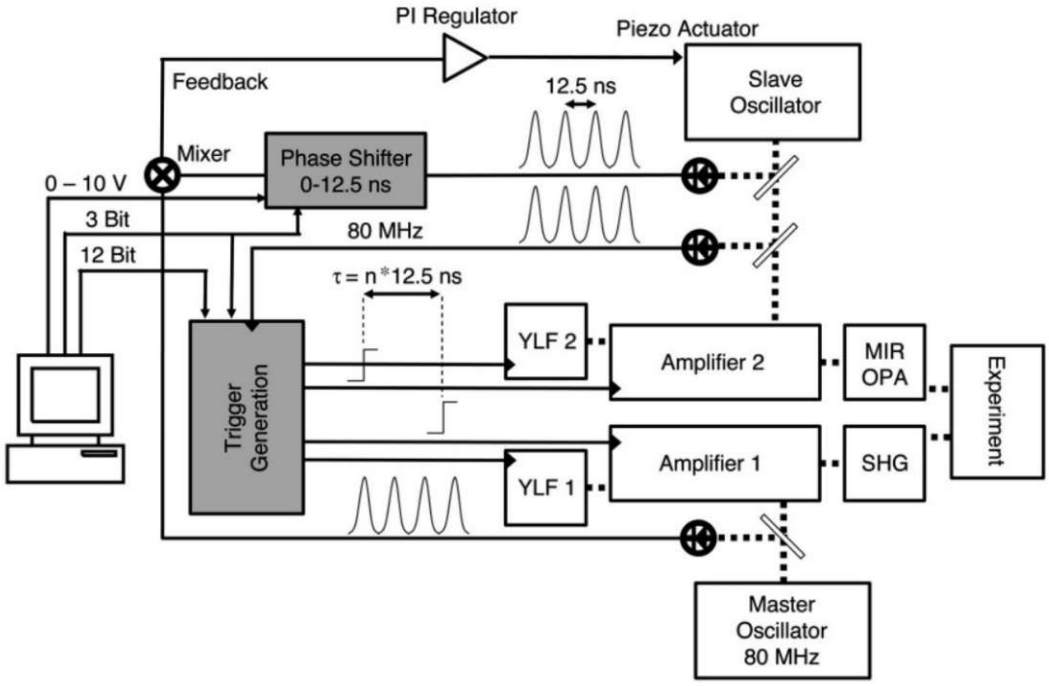

Figure 8.3: Concept of Bredenbeck et al. to generate a tunable time delay between two pulses. Figure from [145], with the permission of AIP Publishing.

possibility of controlling the time delay deterministically. An example of this is Arbitrary-Detuning ASOPS (AD-ASOPS) [146], where the need for an active oscillator repetition rate detuning is replaced by advanced post-processing methods based on tracking the timings of two free-running oscillators. This allows for a sub-ps accuracy in determining a-posteriori the time delay on a short scale. In order to reach larger time delays up to a millisecond, the free-running oscillators can seed one amplifier each (kHz AD-ASOPS) with the amplifier trigger signals controlling the long-scale delay [147, 148]. The fine delay then, however, still shows a jitter in the nanosecond range. Regarding the need for a controllable time-delay source with a high dynamic range, this method is already quite close. The drawback, which results in notably extended data collection durations, is that the consistent emergence of a specific delay setting within an anticipated range of delays becomes dependent on statistical variation.
As summary, the method's specifications are outlined in Tab. 8.2.

8.2 Concept of an Optimal Approach

Fig. 8.5 shows the concept of how an optimal system would be able to generate a-priori controllable time delays. Two synchronized pulse trains have a continuously changing delay with a time delay increment of

$$\Delta\tau = \frac{1}{f_{rep,2}} - \frac{1}{f_{rep,1}} \approx \frac{\Delta f_{rep}}{f_{rep}^2} \tag{8.1}$$

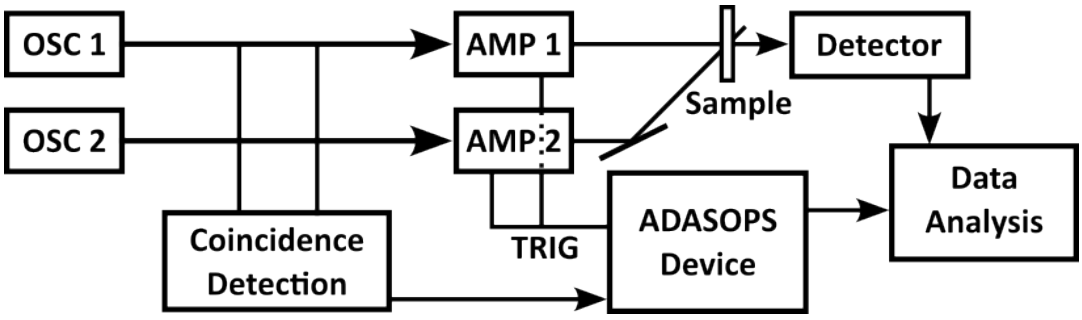

Figure 8.4: Concept of ADASOPS to generate various time delays between two pulses. Figure adapted from [147].

Table 8.2: Specifications of selected methods to generate tunable delays between two pulses.

Specifications					
	Delay Stage	ASOPS	Bredenbeck et al.	kHz-ADASOPS	This Work
Temporal Resolution	fs	≈ 1 ps	< 1.8 ps	ns (a priori) sub-ps (a posteriori)	sub-ps
Delay Range	≥ 1 ns	< 1/frep	practically unlimited	practically unlimited	practically unlimited
Full Controllable Delay	Yes	No	Yes	No	Yes

as in ASOPS. Their repetition rate detuning is stable enough, to provide for a temporal jitter much less than any of the dynamical time scales under investigation. The zero-delay overlap can be determined, by e.g. a cross-correlation measurement, providing a reference for the temporal axis. A pulse pair with a specific temporal spacing is selected by counting the pulses in the respective channels to provide for the desired time delay. The time delay setting is then given by

$$\tau = n\Delta t + \frac{k}{f_{rep,2}}, \tag{8.2a}$$

$$m = n + k \tag{8.2b}$$

where $n\Delta t$ sets the fine delay smaller than the oscillator repetition period and $k/f_{rep,2}$ sets the coarse delay larger than the oscillator repetition period.

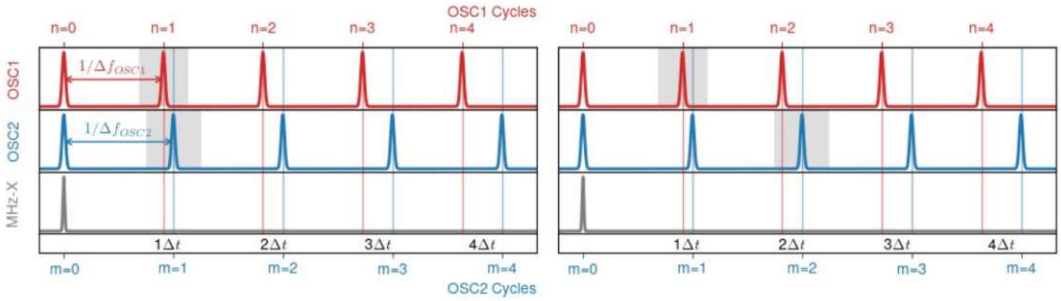

Figure 8.5: Concept of how an optimal system would be able to generate a tunable time delay between two pulses. Plot generated by T. Flöry.

8.3 Experimental Setup

In the following, a method is demonstrated that is able to allow for deterministic control of time delays from fs to ms with a precision that scales with the time delay and shows fs precision at fs time delays. This is enabled by the use of a dual-comb oscillator, providing fs pulses with passively stable time delay operation combined with a slow-feedback loop for low-frequency disturbances [149]. Alltogether, the results show a technique that comes close to the ideal system described in Chapter 8.2.

Fig. 8.6 shows a scheme of the experimental setup for a proof-of-concept demonstration of the technique. An 80 MHz spatially multiplexed single-cavity dual-comb oscillator (Yb:CaF_2, $\lambda = 1050$ nm), provided by ETH Zürich, provides 2.4 W average power per comb, sub-140 fs pulses with a sub-cycle relative timing jitter of only 2.2 fs due to common cavity path architecture with a slow feedback loop for low-frequency disturbances. The repetition rate detuning is set to 500 Hz for the proof-of-concept demonstration, giving a time delay increment of about 80 fs (see Eq. (8.1)). The overlap of the pulse pair is determined by a nonlinear cross-correlation measurement with an SFG signal generated in a BBO crystal in a type 1 phase-matching configuration. The cross-correlation signal generates a

START trigger signal for the timing electronics (Photodiode: Thorlabs PDA10A2, 150 MHz bandwidth). Both, the oscillator pulses and the pulse overlap signal are captured by timing electronics that are used to activate a pair of Pockels Cells (PC) inside two amplifier cavities, with one PC in each cavity, by using a commercial delay generator (Bergmann Messgeräte Entwicklung KG, BME_SG08p). The PCs select in a shot-to-shot manner the pulses for the time delay generation (see Equ. (8.2)) and set the amplification window inside the amplifier. Because of the ultrashort duration of the pulses, the pulses are stretched in a single-grating stretcher and compressed after amplification (CPA) in a single-grating compressor. Amplification takes place in a monolithic dual regenerative amplifier which provides low drift between the cavities, with the RA repetition rate set to the OSC repetition rate detuning of 500 Hz. Amplified pulses show a pulse duration of 600 fs at 1 mJ pulse energy.

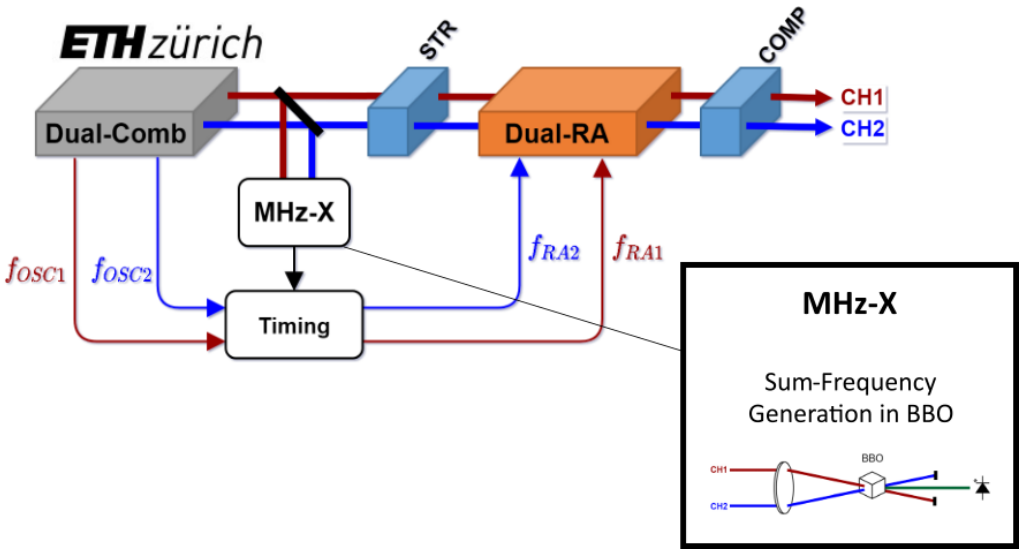

Figure 8.6: Experimental setup. Plot adapted by the thesis author and originally generated by T. Flöry.

8.4 Results

8.4.1 Cross-Correlations of Amplified Pulse Pairs

To show the feasibility of the approach, SFG cross-correlation measurements have been performed by crossing the amplified and compressed pulses spatiotemporally in a type 1 BBO crystal (See Fig. 8.7). The step size was chosen to be 80 fs. Scattered light was suppressed by an aperture and by introducing optical short-pass filters. In Fig. 8.7a, both pulses are well compressed and the cross-correlation trace FWHM width shows a value of 954 fs that is in good agreement with the expected pulse duration. For further proof, one of the compressor arms was detuned on purpose, to lengthen one of the two pulses. This effect is visible in Fig. 8.7b with a reduced peak intensity. For each of these

measurements, 10 scans were performed that all align well with the average, which shows the reproducibility of the technique.

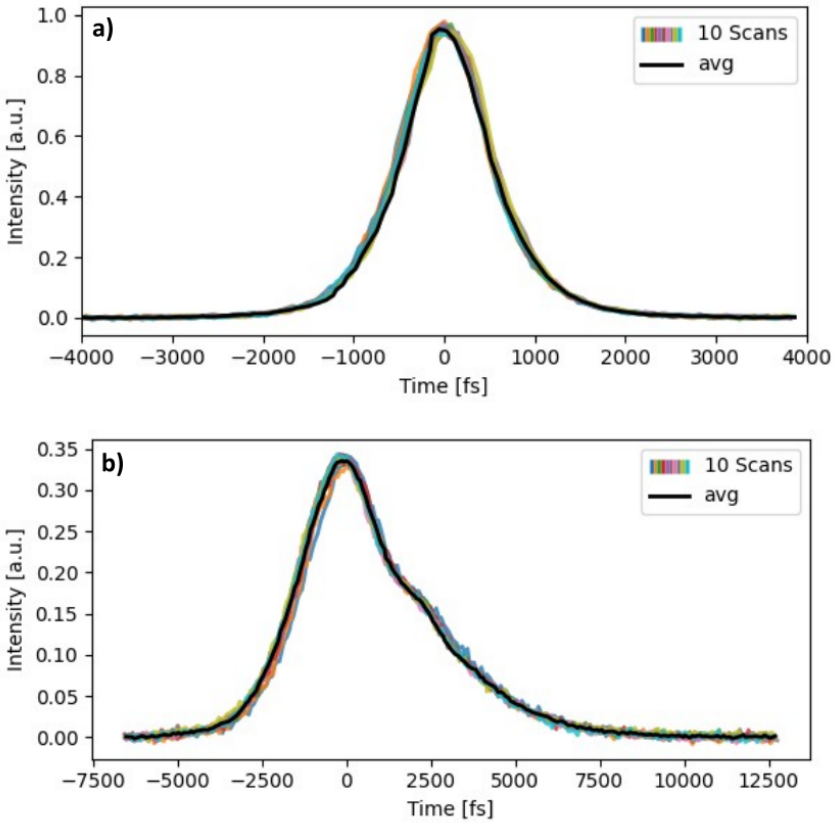

Figure 8.7: Proof-of-concept cross-correlation measurements of the amplified pulses a) with both pulses being compressed to 600 fs. b) with one compressor arm slightly detuned. Plot generated by T. Flöry.

One of the advantages of the technique is that it is possible to stay at a certain time delay by picking the pulse pair (with indices n, m) as needed. This decreases measurement time since one can stay at a certain delay where an increase in SNR from a single scan is required while accumulating less signal at ranges where this is not the case. The demonstration of this capability can be performed, by acquiring measurement results with 400 scans per delay point and analyzing the data statistics. The results of such a measurement can be seen in Fig. 8.8a, where the intensity distributions for four delay values were analyzed (Fig. 8.8b) and calculated against their corresponding timing jitter. The uncertainty due to jitter is about 80 fs (Fig. 8.8c), which was identified to be mainly due to the trigger signal generation.

8.4.2 Pump-Probe measurements of a Perovskite Sample

The demonstration of an application showing the versatility of the technique and its high dynamic range is given in this section. It is done by demonstration of a transient-absorption measurement of a perovskite sample, which was chosen to be a polycrystalline thin film of $CH_3NH_3PbI_3$. It is a proper candidate for this experiment, because when pumped with

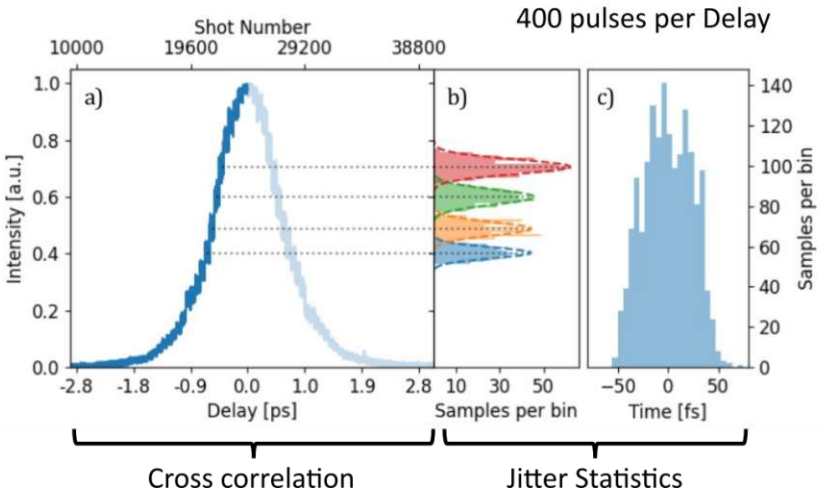

Figure 8.8: For two amplified compressed pulses: Cross-correlation data and signal analysis in the case of 400 pulse scans per delay. Plot generated by T. Flöry.

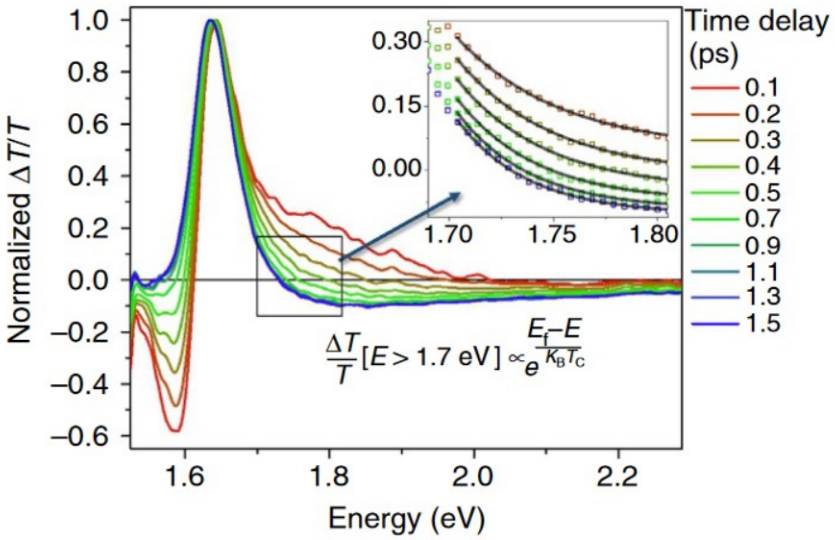

Figure 8.9: Figure from [150], published by Nature Communications under a CC BY 4.0 license.

a pulse at a photon energy of 2.25 eV, it shows a long-lived photoinduced absorption above the band edge ($>$ 1.7 eV), but also short-lived features below the bandgap at 1.58 eV [150]. Above the bandgap, these features are given by quasi-thermalized hot carrier distributions at temperatures, that are higher than the lattice temperature of the sample, with hot carriers progressively cooling down to the band edge as the delay increases (Fig. 8.9).

The two-color pump-probe setup is shown in Fig. 8.10. The pump pulse is generated by SHG of one of the channels leading to a wavelength of 525 nm, which corresponds to a photon energy of 2.36 eV and thus with an excess energy of 780 meV above the bandgap. The pump beam is chopped at 250 Hz, being one-half of the amplifier repetition rate for lock-in detection. The probe pulse is acquired by feeding a non-collinear optical parametric amplifier (NOPA) with the other channel and by tuning the NOPA near the bandgap to 760 nm. Permanent photobleaching was avoided by keeping the pump fluence sufficiently low.

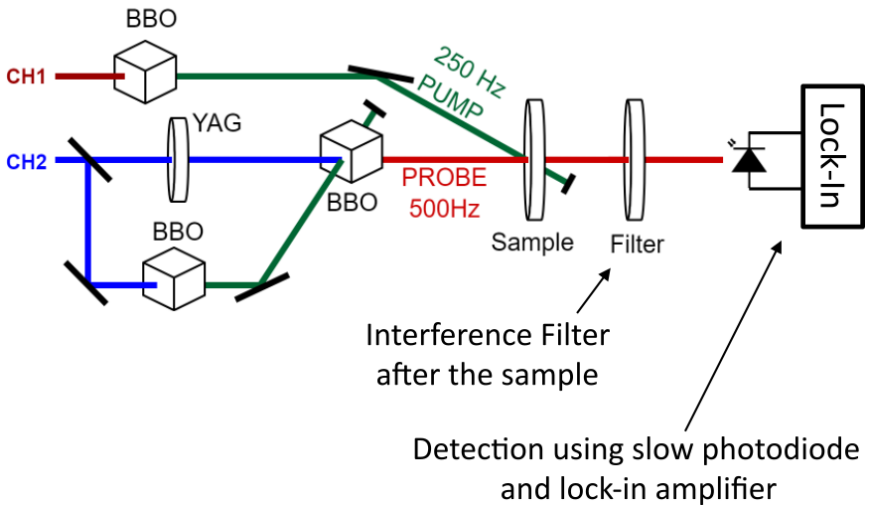

Figure 8.10: Pump-probe setup for transient absorption measurements of a polycrystalline thin film of $CH_3NH_3PbI_3$. Figure adapted by the thesis author and originally generated by T. Flöry

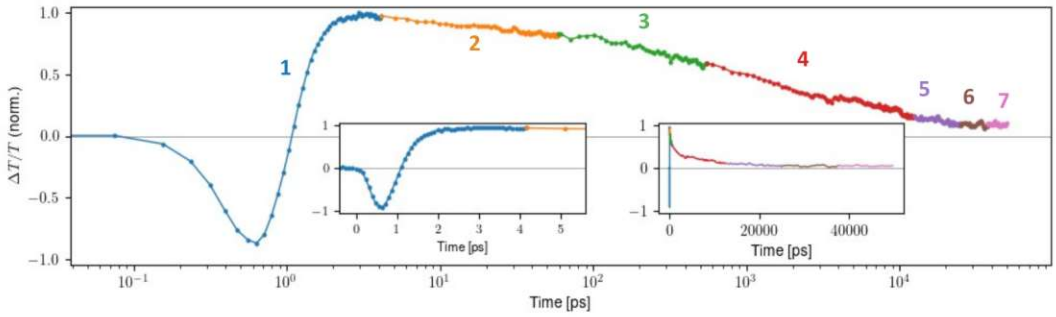

Figure 8.11: Results for transient absorption measurements of a polycrystalline thin film of $CH_3NH_3PbI_3$. Plot generated by T. Flöry.

The results of the pump-probe measurement are plotted in Fig. 8.11 showing the

Table 8.3: Step sizes and measurement times in the experiment.

Range	Stepsize (ps)	Number of Steps	Measurement Time (s)
1	0.08	150	90
2	0.96	110	66
3	99.92	128	76.8
4	255.92	50	30
5-7	511.92	25	15
			Total: 337.8

normalized transmission depending on the pump-probe time delay. The scan range was 50 ns with a measurement time of less than 6 minutes. To resolve the dynamics on all time scales, the step size of the scan was adapted, being 80 fs at the femtosecond range, up to about 512 ps at the longer, nanosecond range (See Tab. 8.3). At short delay times, the photoinduced absorption due to bandgap renormalization leads to a red-shift in the bandgap [151]. As the temperature of the charge carriers decreases and they migrate towards the band edge, the initially induced absorption due to the pump pulse gradually transitions into photobleaching-typical characteristics associated with excitons and carriers that have reached thermal equilibrium. This transition leads to a reversal in the direction of the changes observed in transmission. The generation of the positive signal occurs within 2 picoseconds, aligning with findings from earlier research [150, 151]. Subsequently, the signal undergoes decay over nanoseconds, illustrating a combination of recombination processes involving trap-assisted as well as Auger recombination [152, 153].

Appendix: Burst Python Class

```
import numpy as np
import numpy.fft as fft

class Burst():
    """
    class representing a burst of pulses

    Attributes
    ----------
    mandatory attributes for initialization:

    EITHER
    N:  int
        number of gridpoints,
        fourier relation for frequency and time resolution is given by
        (\Delta f)*(\Delta t) = 1/N
    OR
    df: float
        frequency step

    ...AND FURTHER
    M:  int
        number of pulses
    dT: float
        pulse spacing
    wl_0: float
        central wavelength
    bw_wl: float
        bandwidth
    ---
    ampl:   M-array, float
        amplitudes
    phis:    M-array, float
        CE phases of pulses
    wl_m: M-array, float
        carrier wavelength of pulses, optionally allows to set central
        wavelengths of pulses individually
    f0: float
        central frequency
    bw_f:   float
        frequency BW of spectrum
    C:  float
        chirp of pulses
```

```
    TD: boolean
        if True: burst will be also calculated in the time-domain
    WINDOW_F: float
        frequency domain range = bw_f*WINDOW_F
    SGAUSS: int
        super-gaussian order of envelope
    f: N-array, float
        frequency axis
    t: N-array, float
        time axis
    dt: float
        time step
    pulse_f:    N-array, complex
        single pulse in frequency domain
    burst_f:    N-array, complex
        burst in frequency domain
    pulse_t:    N-array, complex
        single pulse in time domain
    burst_t:    N-array, complex
        burst in time domain
    tau:    float
        pulse duration
    """

    def __init__(self,N=0,df=None,M=0,ampl=None,phis=None,dT=0,wl_0=0,
                 bw_wl=0,wl_m=None,C=0,TD=False,WINDOW_F=100,SGAUSS=2):
        c0 = 299792458
        self.M=M

        if ampl is None: self.ampl=np.array([1]*M)
        else: self.ampl=ampl

        if phis is None: self.phis=np.array([0]*M)
        else: self.phis=phis

        self.dT=dT
        self.wl_0=wl_0
        self.f0 = c0/self.wl_0
        self.bw_wl=bw_wl
        self.bw_f = c0*self.bw_wl/self.wl_0**2
        self.C=C
        self.TD=TD
        self.WINDOW_F=WINDOW_F
        self.SGAUSS=SGAUSS
        self.N = N

        if wl_m is None:
            self.wl_m = np.array([wl_0]*M)
            self.f_m = c0/self.wl_m
        else:
            self.wl_m = wl_m
            self.f_m = c0/self.wl_m
```

```
        if N==0 and not(df is None):
            self.df = df
            self.generateBurst()
        elif N==0 and df is None:
            self.df = 0
            self.t=np.zeros((N))
            self.dt=0
            self.f=np.zeros((N))
            self.df=0
            self.pulse_f=np.zeros((N))
            self.pulse_t=np.zeros((N))
            self.burst_f=np.zeros((N))
            self.burst_t=np.zeros((N))
        else: self.generateBurst()

    def generateBurst(self):
        self.GenFreqAxis()
        self.dt = 1/((self.N-1)*self.df)
        self.t = np.linspace(-self.N/2*self.dt,self.N/2*self.dt,self.N,\
            endpoint=True)
        self.pulse_f = self.Envelope()*self.Chirp()
        self.burst_f = self.GenBurstFf()
        if self.TD:
            self.pulse_t,self.burst_t = self.GenTimeDomainSignal()
            self.tau = self.calc_fwhm(self.t,self.pulse_t)
        else:
            self.pulse_t = np.zeros((self.N),dtype=np.complex)
            self.burst_t = np.zeros((self.N),dtype=np.complex)
            self.tau = 0

    def GenFreqAxis(self):
        window_f = self.WINDOW_F*self.bw_f
        if self.N == 0:
            # set up via df
            self.f = np.arange(-window_f/2+self.f0,window_f/2+self.f0,self.df)
            self.N = len(self.f)
        else:
            # set up via N
            self.f = np.linspace(-window_f/2+self.f0,window_f/2+self.f0,self.N)
            self.df = self.f[1]-self.f[0]

    def Envelope(self):
        return np.exp(-2*np.log(2)*((self.f-self.f0)/self.bw_f)**self.SGAUSS)

    def Chirp(self):
        return np.exp(-1j*2*np.log(2)*self.C*((self.f-self.f0)/self.f0)**2)

    def ShiftMod(self,arr,f0,DT):
        # need to subtract f0 from f here, because frequency coordinate
        # system origin is at f0
        return arr*np.exp(-1j*2*np.pi*(self.f-f0)*DT)
```

```
def GenBurstFf(self):
    ### calculate complex burst field F in frequency domain with
    ### M pulses and phase offsets phis
    sF_f = self.pulse_f
    df = self.f[1]-self.f[0]
    fidx_shift = np.array(((self.f_m-self.f0)/df),dtype=int)
    F_f = np.zeros((len(sF_f)),dtype=np.complex128)
    if (self.M%2)==0:
        # M even
        for k in np.arange(int(self.M/2)):
            idx = int(self.M/2)+k
            F_temp = self.ShiftArr(sF_f,fidx_shift[idx])
            F_f += self.ampl[idx]*\
                self.ShiftMod(F_temp,\
                              self.f0,\
                              self.dT/2+k*self.dT)*\
                np.exp(1j*self.phis[idx])

            idx = int(self.M/2)-1-k
            F_temp = self.ShiftArr(sF_f,fidx_shift[idx])
            F_f += self.ampl[idx]*\
                self.ShiftMod(F_temp,\
                              self.f0,\
                              (-1)*self.dT/2-k*self.dT)*\
                np.exp(1j*self.phis[idx])
    else:
        # M uneven
        for k in np.arange(-int(self.M/2),int(self.M/2)+1):
            idx = int(self.M/2)+k
            F_temp = self.ShiftArr(sF_f,fidx_shift[idx])
            F_f += self.ampl[idx]*\
                self.ShiftMod(F_temp,self.f0,k*self.dT)*\
                np.exp(1j*self.phis[idx])
    return F_f

def MyIFFT(self,input):
    return fft.fftshift(fft.ifft(fft.ifftshift(input)))

def GenTimeDomainSignal(self):
    # --- create time pulse from spectrum via ifft
    temp_pulse_t = self.MyIFFT(self.pulse_f)
    temp_burst_t = self.MyIFFT(self.burst_f)
    return (temp_pulse_t,temp_burst_t)

def PulsePosTime(self):
    pos = np.arange(0,self.M*self.dT,self.dT)
    pos -= (self.M-1)*self.dT/2
    return pos

def PulsePosTimeIdx(self):
    pos = self.PulsePosTime()
```

```
        idx = np.array([],dtype=int)
        for p in pos:
            idx = np.append(idx,np.abs(self.t-p).argmin())
        return idx

    def RightShiftArr(self,arr,n):
        import numpy as np
        # Rightshifts elements of array arr by n
        # elements that exceed index are NOT put in back
        # on the other side of array
        if n>0:
            return np.pad(arr,(n,0), mode='constant')[:-n]
        else:
            return arr

    def LeftShiftArr(self,arr,n):
        import numpy as np
        # Leftshifts elements of array arr by n
        # elements that exceed index are NOT put in back
        # on the other side of array

        if n>0:
            return np.pad(arr,(0,n), mode='constant')[n:]
        else:
            return arr

    def ShiftArr(self,arr,n):
        import numpy as np
        # Shifts elements of array arr by n
        # elements that exceed index are NOT put in back
        # on the other side of array
        if n>=0:
            return self.RightShiftArr(arr,n)
        else:
            return self.LeftShiftArr(arr,-n)

    def calc_fwhm(self,x,y):
        # calc fwhm of y along dimensional array x
        import numpy as np
        _max2 = np.abs(y).max()/2
        _len2 = int(len(y)/2)

        idx1 = np.argmin(

                    np.abs(y[:_len2]-_max2)
                )
        idx2 = _len2 + np.argmin(
                            np.abs(y[_len2:]-_max2)
                        )

        return x[idx2]-x[idx1]
```

```
    def get_range(self,arr,start,stop):
        # useful snippet to get array with elements within
        # start and stop
        return arr[(arr>start)&(arr<stop)]
```

List of Publications

Articles

1. **Vinzenz Stummer**, Tobias Flöry, Matthias Schneller, Markus Zeiler, Audrius Pugžlys, Andrius Baltuška, "Direct Frequency-Mode-Stable Laser Amplification at Terahertz Burst Rates", arXiv:2307.07349, (2023), under peer review at APL Photonics. DOI: 10.48550/arXiv.2307.07349

2. **Vinzenz Stummer**, Tobias Flöry, Matthias Schneller, Markus Zeiler, Audrius Pugžlys, Andrius Baltuška, "Spectral Peak Recovery in Parametrically Amplified THz-Repetition-Rate Bursts", arXiv:2305.16067, (2023), accepted for publication at Optics Express. DOI: 10.48550/arXiv.2305.16067

3. **Vinzenz Stummer**, Tobias Flöry, Gergő Krizsán, Gyula Polónyi, Edgar Kaksis, Audrius Pugžlys, János Hebling, József András Fülöp, Andrius Baltuška, "Programmable generation of terahertz bursts in chirped-pulse laser amplification", Optica 7, 1758 (2020)

4. Tobias Flöry, **Vinzenz Stummer**, Justinas Pupeikis, Benjamin Willenberg, Alexander Nussbaum-Lapping, Edgar Kaksis, Franco VA Camargo, Martynas Barkauskas, Christopher R Phillips, Ursula Keller, Giulio Cerullo, Audrius Pugžlys, Andrius Baltuška, "Rapid-scan nonlinear time-resolved spectroscopy over arbitrary delay intervals", Ultrafast Science 3, 0027 (2023)

5. Hongtao Hu, Tobias Flöry, **Vinzenz Stummer**, Audrius Pugžlys, Markus Kitzler-Zeiler, Xinhua Xie, Alexei Zheltikov, Andrius Baltuška, "Hyper Spectral Resolution Stimulated Raman Spectroscopy with Amplified fs Pulse Bursts", arXiv:2305.16273, (2023), under peer review at Nature Light. DOI: 10.48550/arXiv.2305.16273

6. Lukas Tarra, Andreas Deutschmann-Olek, **Vinzenz Stummer**, Tobias Flöry, Andrius Baltuška, and Andreas Kugi, "Stochastic nonlinear model of the dynamics of actively Q-switched lasers", Opt. Express 30(18), 32411-32427 (2022)

7. Lukas Tarra, Andreas Deutschmann-Olek, **Vinzenz Stummer**, Tobias Flöry, Andrius Baltuška, Andrejus Michailovas, and Andreas Kugi, "Modellierung und Regelung aktiv gütegeschalteter Laser: Ein Überblick über stochastische und dynamische Effekte sowie die resultierende Regelungsaufgabe", Automatisierungstechnik 70(8), 682-691 (2022)

8. Andreas Deutschmann, Tobias Flöry, Katharina Schrom, **Vinzenz Stummer**, Andrius Baltuška, Andreas Kugi, "Bifurcation suppression in regenerative amplifiers by active feedback methods", Optics Express 28(2), 1722-1737 (2020)

9. Seyedreza Larimian, Christoph Lemell, **Vinzenz Stummer**, Ji-Wei Geng, Stefan Roither, Daniil Kartashov, Li Zhang, Mu-Xue Wang, Qihuang Gong, Liang-You Peng, Shuhei Yoshida, Joachim Burgdörfer, Andrius Baltuška, Markus Kitzler, Xinhua Xie, "Localizing high-lying Rydberg wave packets with two-color laser fields", Physical Review A 96(2), 021403 (2017)

Oral Contributions at International Conferences

Presenter:

1. **Vinzenz Stummer**, Tobias Flöry, Matthias Schneller, Edgar Kaksis, Markus Zeiler, Audrius Pugžlys, Andrius Baltuška, "Generation of phase-stable sub-mJ ultrashort laser pulse bursts with extremely high scalable pulse number", EOS Annual Meeting (2023)

2. **Vinzenz Stummer**, Matthias Schneller, Tobias Flöry, Edgar Kaksis, Markus Zeiler, Audrius Pugžlys, Andrius Baltuška, "Hybrid-Amplified THz-Repetition-Frequency Bursts"; CLEO/Europe-EQEC, Optica Publishing Group, CF-11.6 (2023)

3. Tobias Flöry, **Vinzenz Stummer**, Justinas Pupeikis, Benjamin Willenberg, Alexander Nussbaum-Lapping, Franco Valduga de Almeida Camargo, Martynas Barkauskas, Christopher R. Phillips, Ursula Keller, Giullio Cerullo, Audrius Pugžlys, Andrius Baltuška, "Nonlinear time-resolved spectroscopy with extremely high temporal dynamic range", CLEO: Science and Innovations, Optica Publishing Group, SM2F.2 (2023)

4. **Vinzenz Stummer**, Tobias Flöry, Edgar Kaksis, Matthias Schneller, Markus Kitzler-Zeiler, Audrius Pugžlys, Andrius Baltuška, "Single-Shot Acquisition of Hybrid-Amplified THz-Repetition-Frequency Bursts", CLEO: Science and Innovations, Optica Publishing Group, SF1I.7 (2023)

5. **Vinzenz Stummer**, Tobias Flöry, Markus Kitzler-Zeiler, Audrius Pugžlys, Andrius Baltuška, "Hybrid Amplification of THz-Repetition-Frequency Bursts", Advanced Solid State Lasers, Optica Publishing Group, AM5A.6 (2022)

6. **Vinzenz Stummer**, Tobias Flöry, Lukas Tarra, Andreas Deutschmann, Andrejus Michailovas, Andreas Kugi, Andrius Baltuška, "A model-based approach to achieve a multi-100kHz repetition rate, self-seeded Q-switched oscillator with stable pulse-to-pulse energies", CLEO: Applications and Technology, Optica Publishing Group, AM3I.5 (2022)

7. **Vinzenz Stummer**, Tobias Flöry, Edgar Kaksis, Audrius Pugžlys, Andrius Baltuška, "Robust Self-Referenced Generator of Programmable Multi- Millijoule THz-Rate Bursts", EOS Annual Meeting (2021)

8. **Vinzenz Stummer**, Tobias Flöry, Edgar Kaksis, Audrius Pugžlys, Andrius Baltuška, "Robust Self-Referenced Generator of Programmable Multi-Millijoule THz-Rate Bursts", CLEO: Science and Innovations, Optica Publishing Group, STh4N.4 (2021)

9. **Vinzenz Stummer**, Tobias Flöry, Edgar Kaksis, Audrius Pugžlys, Andrius Baltuška, Gergő Krizsán, Gyula Polónyi, József Fülöp, "Generation of Continuously-Tunable, Narrowband THz Pulses from Phase-Locked Femtosecond Pulse Bursts", International Conference on Ultrafast Phenomena, Optica Publishing Group, Tu4B.12 (2020)

10. **Vinzenz Stummer**, Tobias Flöry, Edgar Kaksis, Audrius Pugzlys, Andrius Baltuška, "Programmable Generation of Multi-Millijoule Femtosecond Pulse Bursts with Terahertz Intraburst Repetition Rate", 9th EPS-QEOD Europhoton Conference, (2020)

Poster Contributions at International Conferences

1. **Vinzenz Stummer**, Tobias Flöry, Edgar Kaksis, Audrius Pugžlys, Andrius Baltuška, Gergő Krizsán, Gyula Polónyi, József András Fülöp, "Generation of Continuously Tunable, Narrowband THz Pulses from Phase-Locked Femtosecond Pulse Bursts", The 22nd International Conference on Ultrafast Phenomena, Tu4B.12 (2020)

2. Tobias Flöry, **Vinzenz Stummer**, Edgar Kaksis, Audrius Pugžlys, Andrius Baltuška, "Phase-locked programmable femtosecond pulse bursts from a regenerative amplifier", Advanced Solid State Lasers, Optica Publishing Group, JM5A.36 (2019)

Co-author:

1. Hongtao Hu, Xinhua Xie, Tobias Flöry, **Vinzenz Stummer**, Audrius Pugzlys, Markus Kitzler, Alexei Zheltikov, Andrius Baltuška, "High-Spectral-Resolution Stimulated Raman Spectroscopy with Amplified fs Pulse Bursts", CLEO: Science and Innovations, Optica Publishing Group, SS2A.1 (2022)

2. Tobias Flöry, **Vinzenz Stummer**, Justinas Pupeikis, Benjamin Willenberg, Alexander Nussbaum-Lapping, Franco Valduga de Almeida Camargo, Martynas Barkauskas, Christopher R. Phillips, Ursula Keller, Giullio Cerullo, Audrius Pugžlys, Andrius Baltuška, "Rapid motion-free generation of interpulse delays for time-domain pump-probe spectroscopies with amplified fs pulses", CLEO: Science and Innovations, Optica Publishing Group, SM3F.2 (2022)

3. Gergő Krizsán, **Vinzenz Stummer**, Tobias Flöry, Edgar Kaksis, Audrius Pugžlys, Andrius Baltuška, Gyula Polónyi, József A Fülöp, "Generation of Continuously-Tunable, Narrowband THz Pulses from Phase-Locked Femtosecond Pulse Bursts", Compact EUV & X-ray Light Sources, Optica Publishing Group, JW1A.7 (2020)

4. Claudia Gollner, Hovan Lee, Xi Jiaqi, Cedric Weber, Elisa Sollinger, **Vinzenz Stummer**, Andrius Baltuška, Yan Zhang, Audrius Pugzlys, Mostafa Shalaby, "Efficient broadband terahertz generation in BNA organic crystals at ytterbium laser wavelength", 45th International Conference on Infrared, Millimeter, and Terahertz Waves, (2020), DOI: 10.1109/IRMMW-THZ46771.2020.9370510

5. József András Fülöp, Gyula Polónyi, Krizsán Gergö, Nelson M Mbithi, Priyo Syamsul Nugraha, Gábor Almási, László Pálfalvi, Zoltán Tibai, György Tóth, János Hebling, **Vinzenz Stummer**, Tobias Flöry, Edgar Kaksis, Audrius Pugžlys, Andrius Baltuška, "Novel intense single-and multicycle THz sources", 45th International Conference on Infrared, Millimeter, and Terahertz Waves, (2020), DOI: 10.1109/IRMMW-THz46771.2020.9370719

6. Audrius Pugžlys, Tobias Flöry, **Vinzenz Stummer**, Edgar Kaksis, Ignas Astrauskas, Pavel N Malevich, Andrius Baltuška, Gergö Krizsán, Gyula Polonyi, Jozsef A Fülöp, "Amplified programmable frequency-tunable fs pulse bursts: from THz synthesis to strong-field molecular applications", Ultrafast Optics XII, (2019)

List of Abbreviations

RA	**R**egenerative **A**mplifier
OSC	**O**scillator
CPA	**C**hirped **P**ulse **A**mplification
PSCPA	**P**hase **S**crambled **C**hirped **P**ulse **A**mplification
DPA	**D**ivided **P**ulse **A**mplification
OPA	**O**ptical **P**arametric **A**mplifier
SHG	**S**econd **H**armonic **G**eneration
SFG	**S**um **F**requency **G**eneration
SPM	**S**elf **P**hase **M**odulation
DFG	**D**ifference **F**requency **G**eneration
BBO	**B**eta-**B**arium **B**orate
CEP	**C**arrier-**E**nvelope **P**hase
SPEC	**S**pectrometer
VIS	**VIS**ual
NIR	**N**ear-**I**nfra**R**ed
XC	**X**/Cross **C**orrelation
AC	**A**uto**C**orrelation
STR	**S**tretcher
TFP	**T**hin-**F**ilm **P**olarizer
EM	**E**nd **M**irror
FM	**F**olding **M**irror
CM	**C**urved **M**irror
MT	**M**anual **T**ranslation Stage
PZT	**P**ie**Z**oelectric **T**ransducer
TS	**T**ranslation **S**tage
PC	**P**ockels **C**ell
FR	**F**araday **R**otator
HWP	**H**alf **W**ave**P**late
QWP	**Q**uarter **W**ave**P**late
L	**L**ens
F	**F**ilter
CBM	**C**urved **B**ack-reflecting **M**irror
CW	**C**ontinuous **W**ave
WLG	**W**hite-**L**ight **G**eneration
BD	**B**eam **D**ump

AP	**AP**erture
DDS	**D**irect **D**igital **S**ynthesis
SNR	**S**ignal-to-**N**oise **R**atio
THz	**T**erahertz
TPFP	**T**ilted-**P**ulse-**F**ront-**P**umping
MHz	**M**egahertz
kHz	**K**ilohertz
AOM	**A**coustic-**O**ptical **M**odulator
BS	**B**eam **S**plitter
FFT	**F**ast **F**ourier **T**ransform
FWHM	**F**ull **W**idth **A**t **H**alf **M**aximum
RRM	**R**epetition **R**ate **M**ultiplication
LIBS	**L**aser **I**nduced **B**reakdown **S**pectroscopy
PLD	**P**ulsed **L**aser **D**eposition
FEL	**F**ree **E**lectron **L**aser
SRS	**S**timulated **R**aman **S**cattering
REMPI	**R**esonantly-**E**nhanced **M**ulti-**P**hoton **I**onization
IRMPD	**I**nfrared **R**esonant **M**ulti-**P**hoton **D**issociation
PPLN	**P**eriodically **P**oled **L**ithium **N**iobate
BSRS	**B**urst-driven **S**timulated **R**aman **S**cattering
ASOPS	**AS**ynchronous **OP**tical **S**ampling
NOPA	**N**on-**C**ollinear **O**ptical **P**arametric **A**mplifier
QSW	**Q**-**SW**itch

Bibliography

[1] Vinzenz Stummer, Tobias Flöry, Matthias Schneller, Markus Zeiler, Audrius Pugžlys, and Andrius Baltuška. Direct Frequency-Mode-Stable Laser Amplification at Terahertz Burst Rates, July 2023.

[2] Vinzenz Stummer. Multi-millijoule femtosecond laser pulse bursts. Master's thesis, Technische Universität Wien, 2019.

[3] Jean-Claude Diels and Wolfgang Rudolph. *Ultrashort Laser Pulse Phenomena: Fundamentals, Techniques, and Applications on a Femtosecond Time Scale*. Optics and Photonics. Elsevier / Academic Press, Amsterdam ; Boston, 2nd ed edition, 2006.

[4] F. Hlawatsch and P. Flandrin. The interference structure of the Wigner distribution and related time-frequency signal representations. In *The Wigner Distribution - Theory and Applications in Signal Processing*. Elsevier, 1997.

[5] Vinzenz Stummer, Tobias Flöry, Gergő Krizsán, Gyula Polónyi, Edgar Kaksis, Audrius Pugžlys, János Hebling, József András Fülöp, and Andrius Baltuška. Programmable generation of terahertz bursts in chirped-pulse laser amplification. *Optica*, 7(12):1758, December 2020.

[6] A. B. Zylstra, O. A. Hurricane, D. A. Callahan, A. L. Kritcher, J. E. Ralph, H. F. Robey, J. S. Ross, C. V. Young, K. L. Baker, D. T. Casey, T. Döppner, L. Divol, M. Hohenberger, S. Le Pape, A. Pak, P. K. Patel, R. Tommasini, S. J. Ali, P. A. Amendt, L. J. Atherton, B. Bachmann, D. Bailey, L. R. Benedetti, L. Berzak Hopkins, R. Betti, S. D. Bhandarkar, J. Biener, R. M. Bionta, N. W. Birge, E. J. Bond, D. K. Bradley, T. Braun, T. M. Briggs, M. W. Bruhn, P. M. Celliers, B. Chang, T. Chapman, H. Chen, C. Choate, A. R. Christopherson, D. S. Clark, J. W. Crippen, E. L. Dewald, T. R. Dittrich, M. J. Edwards, W. A. Farmer, J. E. Field, D. Fittinghoff, J. Frenje, J. Gaffney, M. Gatu Johnson, S. H. Glenzer, G. P. Grim, S. Haan, K. D. Hahn, G. N. Hall, B. A. Hammel, J. Harte, E. Hartouni, J. E. Heebner, V. J. Hernandez, H. Herrmann, M. C. Herrmann, D. E. Hinkel, D. D. Ho, J. P. Holder, W. W. Hsing, H. Huang, K. D. Humbird, N. Izumi, L. C. Jarrott, J. Jeet, O. Jones, G. D. Kerbel, S. M. Kerr, S. F. Khan, J. Kilkenny, Y. Kim, H. Geppert Kleinrath, V. Geppert Kleinrath, C. Kong, J. M. Koning, J. J. Kroll, M. K. G. Kruse, B. Kustowski, O. L. Landen, S. Langer, D. Larson, N. C. Lemos, J. D. Lindl, T. Ma, M. J. MacDonald, B. J. MacGowan, A. J. Mackinnon, S. A. MacLaren, A. G. MacPhee, M. M. Marinak, D. A. Mariscal, E. V. Marley, L. Masse,

K. Meaney, N. B. Meezan, P. A. Michel, M. Millot, J. L. Milovich, J. D. Moody, A. S. Moore, J. W. Morton, T. Murphy, K. Newman, J.-M. G. Di Nicola, A. Nikroo, R. Nora, M. V. Patel, L. J. Pelz, J. L. Peterson, Y. Ping, B. B. Pollock, M. Ratledge, N. G. Rice, H. Rinderknecht, M. Rosen, M. S. Rubery, J. D. Salmonson, J. Sater, S. Schiaffino, D. J. Schlossberg, M. B. Schneider, C. R. Schroeder, H. A. Scott, S. M. Sepke, K. Sequoia, M. W. Sherlock, S. Shin, V. A. Smalyuk, B. K. Spears, P. T. Springer, M. Stadermann, S. Stoupin, D. J. Strozzi, L. J. Suter, C. A. Thomas, R. P. J. Town, E. R. Tubman, C. Trosseille, P. L. Volegov, C. R. Weber, K. Widmann, C. Wild, C. H. Wilde, B. M. Van Wonterghem, D. T. Woods, B. N. Woodworth, M. Yamaguchi, S. T. Yang, and G. B. Zimmerman. Burning plasma achieved in inertial fusion. *Nature*, 601(7894):542–548, January 2022.

[7] Arnaud Royon, Yannick Petit, Gautier Papon, Martin Richardson, and Lionel Canioni. Femtosecond laser induced photochemistry in materials tailored with photosensitive agents [Invited]. *Opt. Mater. Express, OME*, 1(5):866–882, September 2011.

[8] Adrea R. Johnson, Yoshitomo Okawachi, Jacob S. Levy, Jaime Cardenas, Kasturi Saha, Michal Lipson, and Alexander L. Gaeta. Chip-based frequency combs with sub-100 GHz repetition rates. *Opt. Lett.*, 37(5):875, March 2012.

[9] Avik Dutt, Chaitanya Joshi, Xingchen Ji, Jaime Cardenas, Yoshitomo Okawachi, Kevin Luke, Alexander L. Gaeta, and Michal Lipson. On-chip dual-comb source for spectroscopy. *Science Advances*, 4(3):e1701858, March 2018.

[10] Joohyung Lee, Seung-Woo Kim, and Young-Jin Kim. Repetition rate multiplication of femtosecond light pulses using a phase-locked all-pass fiber resonator. *Opt. Express, OE*, 23(8):10117–10125, April 2015.

[11] Miguel A. Preciado and Miguel A. Muriel. All-pass optical structures for repetition rate multiplication. *Opt. Express, OE*, 16(15):11162–11168, July 2008.

[12] Miguel A. Preciado and Miguel A. Muriel. Repetition-rate multiplication using a single all-pass optical cavity. *Opt. Lett., OL*, 33(9):962–964, May 2008.

[13] Yucheng Zhao, Seong-sik Min, Hsiao-chuan Wang, and Simon Fleming. High-power figure-of-eight fiber laser with passive sub-ring loops for repetition rate control. *Opt. Express, OE*, 14(22):10475–10480, October 2006.

[14] Haifeng Jiang, Jennifer Taylor, Franklyn Quinlan, Tara Fortier, and Scott A. Diddams. Noise Floor Reduction of an Er:Fiber Laser-Based Photonic Microwave Generator. *IEEE Photonics Journal*, 3(6):1004–1012, December 2011.

[15] A. Haboucha, W. Zhang, T. Li, M. Lours, A. N. Luiten, Y. Le Coq, and G. Santarelli. Optical-fiber pulse rate multiplier for ultralow phase-noise signal generation. *Opt. Lett., OL*, 36(18):3654–3656, September 2011.

[16] M. S. Kirchner, D. A. Braje, T. M. Fortier, A. M. Weiner, L. Hollberg, and S. A. Diddams. Generation of 20 GHz, sub-40 fs pulses at 960 nm via repetition-rate multiplication. *Opt. Lett., OL*, 34(7):872–874, April 2009.

[17] Jian Chen, Jason W. Sickler, Peter Fendel, Erich P. Ippen, Franz X. Kärtner, Tobias Wilken, Ronald Holzwarth, and Theodor W. Hänsch. Generation of low-timing-jitter femtosecond pulse trains with 2 GHz repetition rate via external repetition rate multiplication. *Opt. Lett., OL*, 33(9):959–961, May 2008.

[18] Guillaume Bonamis, Konstantin Mishchick, Eric Audouard, Clemens Hönninger, Eric Mottay, John Lopez, and Inka Manek-Hönninger. High efficiency femtosecond laser ablation with gigahertz level bursts. *Journal of Laser Applications*, 31(2):022205, May 2019.

[19] A. M. Weiner. Femtosecond pulse shaping using spatial light modulators. *Review of Scientific Instruments*, 71(5):1929–1960, May 2000.

[20] Andrew M Weiner and Ayman M Kan. Femtosecond Pulse Shaping for Synthesis , Processing , and Time-to-Space Conversion of Ultrafast Optical Waveforms. 4(2):317–331, 1998.

[21] M. A. Dugan, J. X. Tull, and W. S. Warren. High-resolution acousto-optic shaping of unamplified and amplified femtosecond laser pulses. *J. Opt. Soc. Am. B, JOSAB*, 14(9):2348–2358, September 1997.

[22] M. Hacker, G. Stobrawa, R. Sauerbrey, T. Buckup, M. Motzkus, M. Wildenhain, and A. Gehner. Micromirror SLM for femtosecond pulse shaping in the ultraviolet. *Appl Phys B*, 76(6):711–714, June 2003.

[23] Michael Müller, Christopher Aleshire, Joachim Buldt, Henning Stark, Christian Grebing, Arno Klenke, and Jens Limpert. Scaling potential of beam-splitter-based coherent beam combination. *Opt. Express, OE*, 29(17):27900–27911, August 2021.

[24] C. Radzewicz, M. J. la Grone, and J. S. Krasinski. Passive pulse shaping of femtosecond pulses using birefringent dispersive media. *Applied Physics Letters*, 69(2):272–274, July 1996.

[25] Shian Zhou, Dimitre Ouzounov, Heng Li, Ivan Bazarov, Bruce Dunham, Charles Sinclair, and Frank W. Wise. Efficient temporal shaping of ultrashort pulses with birefringent crystals. *Appl. Opt., AO*, 46(35):8488–8492, December 2007.

[26] B. Dromey, M. Zepf, M. Landreman, K. O'Keeffe, T. Robinson, and S. M. Hooker. Generation of a train of ultrashort pulses from a compact birefringent crystal array. *Applied Optics*, 46(22):5142–5142, 2007.

[27] M. Bitter and V. Milner. Generating long sequences of high-intensity femtosecond pulses. *Appl. Opt., AO*, 55(4):830–833, February 2016.

[28] Nathalie Picqué and Theodor W. Hänsch. Frequency comb spectroscopy. *Nature Photon*, 13(3):146–157, March 2019.

[29] Theodor W. Hänsch. Nobel lecture: Passion for precision. *Reviews of Modern Physics*, 78(4):1297–1309, 2006.

[30] Dr Rüdiger Paschotta. Carrier–envelope offset. https://www.rp-photonics.com/carrier_envelope_offset.html.

[31] Dr Rüdiger Paschotta. Cavity dumping. https://www.rp-photonics.com/cavity_dumping.html.

[32] W T Roberts. Cavity-Dumped Communication Laser Design. *IPN Progress Report*, 42(152), 2003.

[33] Q factor. *Wikipedia*, March 2023.

[34] W. Köchner. *Solid-State Laser Engineering*. Springer, 6th edition, 2006.

[35] Quasar® Hybrid Fiber Laser. https://www.spectra-physics.com/en/f/quasar-hybrid-fiber-laser.

[36] Lukas Tarra, Andreas Deutschmann-Olek, Vinzenz Stummer, Tobias Flöry, Anrius Baltuska, and Andreas Kugi. Stochastic nonlinear model of the dynamics of actively Q-switched lasers. *Opt. Express, OE*, 30(18):32411–32427, August 2022.

[37] Lukas Tarra, Andreas Deutschmann-Olek, Vinzenz Stummer, Tobias Flöry, Andrius Baltuska, Andrejus Michailovas, and Andreas Kugi. Modellierung und Regelung aktiv gütegeschalteter Laser: Ein Überblick über stochastische und dynamische Effekte sowie die resultierende Regelungsaufgabe. *at - Automatisierungstechnik*, 70(8):682–691, August 2022.

[38] Hamid Hemmati. *Deep Space Optical Communications*. John Wiley & Sons, June 2006.

[39] D.P. Adams, R.D. Murphy, D. Saiz, M. Rodriguez, and D. Hirschfeld. Nanosecond Pulsed Laser Color Marking of Titanium: Analysis of Oxide Layer Phase. In *CLEO: 2013*, page CM1H.7, San Jose, California, 2013. OSA.

[40] Cheng Luo and Liwei Lin. The application of nanosecond-pulsed laser welding technology in MEMS packaging with a shadow mask. *Sensors and Actuators A: Physical*, 97–98:398–404, April 2002.

[41] Yanyan Gao, Chong Liu, Yi Xie, Rilang Guo, Xuqi Zhong, Huanxin Ju, Li Qin, Peng Jia, Shaohang Wu, Ruud E. I. Schropp, and Yaohua Mai. Can Nanosecond Laser Achieve High-Performance Perovskite Solar Modules with Aperture Area Efficiency Over 21%? *Advanced Energy Materials*, 12(41):2202287, 2022.

[42] Sayan Biswas, Isaac Ekoto, Dan Singleton, and Kristapher Mixell. Nanosecond Pulsed Ignition for Automotive Applications: Performance and Emissions Characteristics of Gasoline Combustion in an Optical Engine. SAE Technical Paper 2021-01-0475, SAE International, Warrendale, PA, April 2021.

[43] John P.M. Wood, Malcolm Plunkett, Victor Previn, Glyn Chidlow, and Robert J. Casson. Nanosecond pulse lasers for retinal applications. *Lasers in Surgery and Medicine*, 43(6):499–510, 2011.

[44] Dr Rüdiger Paschotta. Master oscillator power amplifier. https://www.rp-photonics.com/master_oscillator_power_amplifier.html.

[45] Donna Strickland and Gerard Mourou. COMPRESSION OF AMPLIFIED CHIRPED OPTICAL PULSES. *Optics Communications*, 56(3):219–221, 1985.

[46] Dr Rüdiger Paschotta. Regenerative amplifiers. https://www.rp-photonics.com/regenerative_amplifiers.html.

[47] A. Baltuška, Th Udem, M. Uiberacker, M. Hentschel, E. Goulielmakis, Ch Gohle, R. Holzwarth, V. S. Yakovlev, A. Scrinzi, T. W. Hänsch, and F. Krausz. Attosecond control of electronic processes by intense light fields. *Nature*, 421(6923):611–615, February 2003.

[48] G. Cerullo, A. Baltuška, O.d. Mücke, and C. Vozzi. Few-optical-cycle light pulses with passive carrier-envelope phase stabilization. *Laser & Photonics Reviews*, 5(3):323–351, 2011.

[49] G. Steinmeyer, B. Borchers, and F. Lücking. Carrier-envelope phase stabliization. In *Progress in Ultrafast Intense Laser Science*, volume 9, pages 89–110. Springer, 2013.

[50] Ultrafast Lasers Market Size, Share and Analysis | Forecast - 2030. https://www.alliedmarketresearch.com/ultrafast-lasers-market-A12544.

[51] Research and Markets ltd. Global Ultrafast Laser Market by Laser Type (Diode Pumped Lasers, Fiber Laser, Mode Locked Diode Lasers), Pulse Duration (Femtosecond, Picosecond), Application - Cumulative Impact of COVID-19, Russia Ukraine Conflict, and High Inflation - Forecast 2023-2030. https://www.researchandmarkets.com/reports/4985916/global-ultrafast-laser-market-by-laser-type.

[52] M. D. Shirk and P. A. Molian. A review of ultrashort pulsed laser ablation of materials. *Journal of Laser Applications*, 10(1):18–28, February 1998.

[53] X. Liu, D. Du, and G. Mourou. Laser ablation and micromachining with ultrashort laser pulses. *IEEE Journal of Quantum Electronics*, 33(10):1706–1716, October 1997.

[54] B. N. Chichkov, C. Momma, S. Nolte, F. von Alvensleben, and A. Tünnermann. Femtosecond, picosecond and nanosecond laser ablation of solids. *Appl. Phys. A*, 63(2):109–115, August 1996.

[55] Can Kerse, Hamit Kalaycıoğlu, Parviz Elahi, Barbaros Çetin, Denizhan K. Kesim, Önder Akçaalan, Seydi Yavaş, Mehmet D. Aşık, Bülent Öktem, Heinar Hoogland, Ronald Holzwarth, and Fatih Ömer Ilday. Ablation-cooled material removal with ultrafast bursts of pulses. *Nature*, 537(7618):84–88, September 2016.

[56] F. Anabitarte, A. Cobo, and J. M. Lopez-Higuera. Laser-Induced Breakdown Spectroscopy: Fundamentals, Applications, and Challenges. *ISRN Spectroscopy*, 2012:1–12, 2012.

[57] Julius Skruibis, Ona Balachninaite, Simas Butkus, Virgilijus Vaicaitis, and Valdas Sirutkaitis. Multiple-pulse Laser-induced breakdown spectroscopy for monitoring the femtosecond laser micromachining process of glass. *Optics & Laser Technology*, 111:295–302, April 2019.

[58] Makoto Murakami, Bing Liu, Zhendong Hu, Zhenlin Liu, Yuzuru Uehara, and Yong Che. Burst-Mode Femtosecond Pulsed Laser Deposition for Control of Thin Film Morphology and Material Ablation. *Appl. Phys. Express*, 2:042501, March 2009.

[59] Christiane P. Koch, Mikhail Lemeshko, and Dominique Sugny. Quantum control of molecular rotation. *Rev. Mod. Phys.*, 91(3):035005, September 2019.

[60] S. Zhdanovich, C. Bloomquist, J. Floß, I. Sh. Averbukh, J. W. Hepburn, and V. Milner. Quantum Resonances in Selective Rotational Excitation of Molecules with a Sequence of Ultrashort Laser Pulses. *Phys. Rev. Lett.*, 109(4):043003, July 2012.

[61] I. Sh. Averbukh and R. Arvieu. Angular Focusing, Squeezing, and Rainbow Formation in a Strongly Driven Quantum Rotor. *Phys. Rev. Lett.*, 87(16):163601, September 2001.

[62] M. Bitter and V. Milner. Rotational excitation of molecules with long sequences of intense femtosecond pulses. *Phys. Rev. A*, 93(1):013420, January 2016.

[63] S. Zhdanovich, A. A. Milner, C. Bloomquist, J. Floß, I. Sh. Averbukh, J. W. Hepburn, and V. Milner. Control of Molecular Rotation with a Chiral Train of Ultrashort Pulses. *Phys. Rev. Lett.*, 107(24):243004, December 2011.

[64] S. Zhdanovich, E. A. Shapiro, M. Shapiro, J. W. Hepburn, and V. Milner. Population transfer between two quantum states by piecewise chirping of femtosecond pulses: Theory and experiment. *Physical Review Letters*, 100(10):1–4, 2008.

[65] A. Kamalov, D. W. Broege, and P. H. Bucksbaum. Dynamical localization in molecular alignment of kicked quantum rotors. *Phys. Rev. A*, 92(1):013409, July 2015.

[66] James P. Cryan, Philip H. Bucksbaum, and Ryan N. Coffee. Field-free alignment in repetitively kicked nitrogen gas. *Phys. Rev. A*, 80(6):063412, December 2009.

[67] Stefan Pabst and Robin Santra. Alignment of asymmetric-top molecules using multiple-pulse trains. *Phys. Rev. A*, 81(6):065401, June 2010.

[68] Julien Salomon, Claude M. Dion, and Gabriel Turinici. Optimal molecular alignment and orientation through rotational ladder climbing. *J. Chem. Phys.*, 123(14):144310, October 2005.

[69] Xiaoming Ren, Varun Makhija, and Vinod Kumarappan. Multipulse Three-Dimensional Alignment of Asymmetric Top Molecules. *Phys. Rev. Lett.*, 112(17):173602, April 2014.

[70] Kevin F. Lee, D. M. Villeneuve, P. B. Corkum, Albert Stolow, and Jonathan G. Underwood. Field-Free Three-Dimensional Alignment of Polyatomic Molecules. *Phys. Rev. Lett.*, 97(17):173001, October 2006.

[71] Claudia Gollner, Mostafa Shalaby, Corinne Brodeur, Ignas Astrauskas, Rokas Jutas, Evan Constable, Lorenz Bergen, Andrius Baltuška, and Audrius Pugžlys. Highly efficient THz generation by optical rectification of mid-IR pulses in DAST. *APL Photonics*, 6(4):046105, April 2021.

[72] B. Green, S. Kovalev, V. Asgekar, G. Geloni, U. Lehnert, T. Golz, M. Kuntzsch, C. Bauer, J. Hauser, J. Voigtlaender, B. Wustmann, I. Koesterke, M. Schwarz, M. Freitag, A. Arnold, J. Teichert, M. Justus, W. Seidel, C. Ilgner, N. Awari, D. Nicoletti, S. Kaiser, Y. Laplace, S. Rajasekaran, L. Zhang, S. Winnerl, H. Schneider, G. Schay, I. Lorincz, A. A. Rauscher, I. Radu, S. Mährlein, T. H. Kim, J. S. Lee, T. Kampfrath, S. Wall, J. Heberle, A. Malnasi-Csizmadia, A. Steiger, A. S. Müller, M. Helm, U. Schramm, T. Cowan, P. Michel, A. Cavalleri, A. S. Fisher, N. Stojanovic, and M. Gensch. High-Field High-Repetition-Rate Sources for the Coherent THz Control of Matter. *Sci Rep*, 6:22256, February 2016.

[73] Rui Pan, Ekaterina Zapolnova, and Nikola Stojanovic. Ultrafast High-Field THz beamline at X-ray FEL. In *2019 44th International Conference on Infrared, Millimeter, and Terahertz Waves (IRMMW-THz)*, pages 1–1, September 2019.

[74] Nikola Stojanovic and Markus Drescher. Accelerator- and laser-based sources of high-field terahertz pulses. *J. Phys. B: At. Mol. Opt. Phys.*, 46(19):192001, September 2013.

[75] M. Gensch, L. Bittner, A. Chesnov, H. Delsim-Hashemi, M. Drescher, B. Faatz, J. Feldhaus, U. Fruehling, G. A. Geloni, Ch. Gerth, O. Grimm, U. Hahn, M. Hesse, S. Kapitzki, V. Kocharyan, O. Kozlov, E. Matyushevsky, N. Morozov, D. Petrov, E. Ploenjes, M. Roehling, J. Rossbach, E. L. Saldin, B. Schmidt, P. Schmueser, E. A. Schneidmiller, E. Syresin, A. Willner, and M. V. Yurkov. New infrared undulator beamline at FLASH. *Infrared Physics & Technology*, 51(5):423–425, May 2008.

[76] József András Fülöp, Stelios Tzortzakis, and Tobias Kampfrath. Laser-Driven Strong-Field Terahertz Sources. *Advanced Optical Materials*, 8(3):1900681, 2020.

[77] J. G. Neumann, P. G. O'Shea, D. Demske, W. S. Graves, B. Sheehy, H. Loos, and G. L. Carr. Electron beam modulation using a laser-driven photocathode. *Nuclear Instruments and Methods in Physics Research Section A: Accelerators, Spectrometers, Detectors and Associated Equipment*, 507(1):498–501, July 2003.

[78] C. Caizergues, S. Smartsev, V. Malka, and C. Thaury. Phase-locked laser-wakefield electron acceleration. *Nature Photonics*, 14(August 2020):475–480, 2020.

[79] Morgan T. Hibberd, Alisa L. Healy, Daniel S. Lake, Vasileios Georgiadis, Elliott J.H. Smith, Oliver J. Finlay, Thomas H. Pacey, James K. Jones, Yuri Saveliev, David A. Walsh, Edward W. Snedden, Robert B. Appleby, Graeme Burt, Darren M. Graham, and Steven P. Jamison. Acceleration of relativistic beams using laser-generated terahertz pulses. *Nature Photonics*, 14(12):755–759, 2020.

[80] Hanxun Xu, Lixin Yan, Yingchao Du, Wenhui Huang, Qili Tian, Renkai Li, Yifan Liang, Shaohong Gu, Jiaru Shi, and Chuanxiang Tang. Cascaded high-gradient terahertz-driven acceleration of relativistic electron beams. *Nat. Photonics*, 15(6):426–430, June 2021.

[81] Spencer W. Jolly, Frederike Ahr, Nicholas H. Matlis, Sergio Carbajo, Koustuban Ravi, Tobias Kroh, Jan Schulte, Damian N. Schimpf, Andreas R. Maier, and Franz X. Kärtner. Narrowband terahertz generation with broadband chirped pulse trains in periodically poled lithium niobate. In *2017 Conference on Lasers and Electro-Optics (CLEO)*, pages 1–1, May 2017.

[82] J. A. Fülöp, L. Pálfalvi, G. Almási, and J. Hebling. Design of high-energy terahertz sources based on optical rectification. *Opt. Express, OE*, 18(12):12311–12327, June 2010.

[83] R L Swofford and A C Albrecht. Nonlinear Spectroscopy. *NONLINEAR SPECTROSCOPY*.

[84] Ahmed H. Zewail. Femtochemistry: Atomic-Scale Dynamics of the Chemical Bond. *J. Phys. Chem. A*, 104(24):5660–5694, June 2000.

[85] Martin Dorner-Kirchner, Valentina Shumakova, Giulio Coccia, Edgar Kaksis, Bruno E. Schmidt, Vladimir Pervak, Audrius Pugzlys, Andrius Baltuška, Markus Kitzler-Zeiler, and Paolo Antonio Carpeggiani. HHG at the Carbon K-Edge Directly Driven by SRS Red-Shifted Pulses from an Ytterbium Amplifier. *ACS Photonics*, page acsphotonics.2c01021, December 2022.

[86] Florian Adler, Michael J. Thorpe, Kevin C. Cossel, and Jun Ye. Cavity-Enhanced Direct Frequency Comb Spectroscopy: Technology and Applications. *Annual Review of Analytical Chemistry*, 3(1):175–205, 2010.

[87] Ian Coddington, Nathan Newbury, and William Swann. Dual-comb spectroscopy. *Optica, OPTICA*, 3(4):414–426, April 2016.

[88] Norihiko Nishizawa and Masahito Yamanaka. Periodical spectral peaking on optical pulses. *Optica, OPTICA*, 7(9):1089–1092, September 2020.

[89] Thomas Hellerer, Annika M.K. Enejder, and Andreas Zumbusch. Spectral focusing: High spectral resolution spectroscopy with broad-bandwidth laser pulses. *Appl. Phys. Lett.*, 85(1):25–27, July 2004.

[90] Krzysztof P. Herdzik, Konstantinos N. Bourdakos, Peter B. Johnson, Adam P. Lister, Aleksandra P. Pitera, Chun yu Guo, Peter Horak, David J. Richardson, Jonathan H.V. Price, and Sumeet Mahajan. Multimodal spectral focusing CARS and SFG microscopy with a tailored coherent continuum from a microstructured fiber. *Applied Physics B: Lasers and Optics*, 126(84):1–13, 2020.

[91] Chien Sheng Liao, Kai Chih Huang, Weili Hong, Jing Chen, Karanja Caroline, Gregory Eakins, and Ji Xin Cheng. Stimulated Raman spectroscopic imaging by microsecond delay-line tuning. *Optica*, 3(12):1377–1380, 2016.

[92] Spencer W. Jolly, Nicholas H. Matlis, Frederike Ahr, Vincent Leroux, Timo Eichner, Anne Laure Calendron, Hideki Ishizuki, Takunori Taira, Franz X. Kärtner, and Andreas R. Maier. Spectral phase control of interfering chirped pulses for high-energy narrowband terahertz generation. *Nature Communications*, 10(1), 2019.

[93] M Marangoni, D Brida, M Quintavalle, G Cirmi, F M Pigozzo, C Manzoni, F Baronio, A D Capobianco, and G Cerullo. Narrow-bandwidth picosecond pulses by spectral compression of femtosecond pulses in a second- order nonlinear crystal. *Optics Express*, 15(14):8884–8891, 2007.

[94] M. Marangoni, D. Brida, C. Manzoni, R. Ramponi, G. Cerullo, M. Conforti, F. Baronio, and C. De Angelis. Synthesis and shaping of picosecond pulses by frequency conversion of femtosecond pulses in engineered quadratic media. In *Conference on Lasers and Electro-Optics/International Quantum Electronics Conference (2009), Paper CThZ2*, page CThZ2. Optica Publishing Group, May 2009.

[95] P. N. Malevich, R. Maurer, D. Kartashov, S. Ališauskas, A. A. Lanin, A. M. Zheltikov, M. Marangoni, G. Cerullo, A. Baltuška, and A. Pugžlys. Stimulated Raman gas sensing by backward UV lasing from a femtosecond filament. *Optics Letters*, 40(11):2469–2472, 2015.

[96] A. A. Lanin, I. V. Fedotov, A. B. Fedotov, D. A. Sidorov-Biryukov, and A. M. Zheltikov. The phase-controlled Raman effect. *Scientific Reports*, 3:1842–1842, 2013.

[97] Nirit Dudovich, Dan Oron, and Yaron Silberberg. Single-pulse coherently controlled nonlinear Raman spectroscopy and microscopy. *Nature*, 418(6897):512–514, 2002.

[98] Peter Hamm and Martin Zanni. *CONCEPTS AND METHODS OF 2D INFRARED SPECTROSCOPY*. Cambridge University Press, 2011.

[99] Richard C. Prince, Renee R. Frontiera, and Eric O. Potma. Stimulated Raman Scattering: From Bulk to Nano. *Chem. Rev.*, 117(7):5070–5094, April 2017.

[100] B. Wen, Y. Kim, H. Meyer, J. Kłos, and M. H. Alexander. IR-REMPI double resonance spectroscopy: The near-IR spectrum of NO-Ar revisited. *Journal of Physical Chemistry A*, 112(39):9483–9493, 2008.

[101] Marshall R. Ligare, Anouk M. Rijs, Giel Berden, Martin Kabeláč, Dana Nachtigallova, Jos Oomens, and Mattanjah S. de Vries. Resonant Infrared Multiple Photon Dissociation Spectroscopy of Anionic Nucleotide Monophosphate Clusters. *J. Phys. Chem. B*, 119(25):7894–7901, June 2015.

[102] Ch Wellers, A. Borodin, S. Vasilyev, D. Offenberg, and S. Schiller. Resonant IR multi-photon dissociation spectroscopy of a trapped and sympathetically cooled biomolecular ion species. *Phys. Chem. Chem. Phys.*, 13(42):18799–18809, October 2011.

[103] Robert J. Nieckarz, Jos Oomens, Giel Berden, Pavel Sagulenko, and Renato Zenobi. Infrared multiple photon dissociation (IRMPD) spectroscopy of oxazine dyes. *Phys. Chem. Chem. Phys.*, 15(14):5049–5056, March 2013.

[104] Uwe Kiencke and Holger Jäkel. *Signale Und Systeme*. Oldenburg Verlag München, 2008.

[105] B. E. A. Saleh and M. C. Teich. *Fundamentals of Photonics*. Wiley-Interscience, second edition edition, 2007.

[106] John B. Schneider. Understanding the Finite-Difference Time-Domain Method. https://eecs.wsu.edu/~schneidj/ufdtd/, 2010.

[107] Xi-Jin Cheng and Xiaoliang Xie. *Coherent Raman Scattering Microscopy*. CRC Press, 2013.

[108] Hervé Rigneault and Pascal Berto. Tutorial: Coherent Raman light matter interaction processes. *APL Photonics*, 3(9):091101, July 2018.

[109] Fanghao Hu, Lixue Shi, and Wei Min. Biological imaging of chemical bonds by stimulated Raman scattering microscopy. *Nat Methods*, 16(9):830–842, September 2019.

[110] Wei Min, Christian W. Freudiger, Sijia Lu, and X. Sunney Xie. Coherent Nonlinear Optical Imaging: Beyond Fluorescence Microscopy. *Annual Review of Physical Chemistry*, 62(1):507–530, 2011.

[111] Hervé Rigneault and Pascal Berto. Tutorial: Coherent Raman light matter interaction processes. *APL Photonics*, 3(9):091101, July 2018.

[112] Yanping Li, Binglin Shen, Shaowei Li, Yihua Zhao, Junle Qu, and Liwei Liu. Review of Stimulated Raman Scattering Microscopy Techniques and Applications in the Biosciences. *Advanced Biology*, 5(1):2000184, 2021.

[113] Jeffrey L. Suhalim, Chao-Yu Chung, Magnus B. Lilledahl, Ryan S. Lim, Moshe Levi, Bruce J. Tromberg, and Eric O. Potma. Characterization of Cholesterol Crystals in Atherosclerotic Plaques Using Stimulated Raman Scattering and Second-Harmonic Generation Microscopy. *Biophysical Journal*, 102(8):1988–1995, April 2012.

[114] Shuai Yan, Yiran Li, Zhiliang Huang, Xiaocong Yuan, and Ping Wang. High-Speed Stimulated Raman Scattering Microscopy Using Inertia-Free AOD Scanning. *J. Phys. Chem. B*, 127(19):4229–4234, May 2023.

[115] Dan Fu, Fa-Ke Lu, Xu Zhang, Christian Freudiger, Douglas R. Pernik, Gary Holtom, and Xiaoliang Sunney Xie. Quantitative Chemical Imaging with Multiplex Stimulated Raman Scattering Microscopy. *J. Am. Chem. Soc.*, 134(8):3623–3626, February 2012.

[116] Chien-Sheng Liao, Pu Wang, Ping Wang, Junjie Li, Hyeon Jeong Lee, Gregory Eakins, and Ji-Xin Cheng. Spectrometer-free vibrational imaging by retrieving stimulated Raman signal from highly scattered photons. *Sci. Adv.*, 1(9):e1500738, October 2015.

[117] Hongtao Hu, Tobias Flöry, Vinzenz Stummer, Audrius Pugzlys, Markus Kitzler-Zeiler, Xinhua Xie, Alexei Zheltikov, and Andrius Baltuška. Hyper Spectral Resolution Stimulated Raman Spectroscopy with Amplified fs Pulse Bursts, May 2023.

[118] Andrius Baltuška, Takao Fuji, and Takayoshi Kobayashi. Controlling the Carrier-Envelope Phase of Ultrashort Light Pulses with Optical Parametric Amplifiers. *Phys. Rev. Lett.*, 88(13):133901, March 2002.

[119] Absorption spectroscopy. *Wikipedia*, May 2023.

[120] Serge Haroche and Daniel Kleppner. Cavity Quantum Electrodynamics. *Physics Today*, 42(1):24–30, January 1989.

[121] Purcell effect. *Wikipedia*, August 2023.

[122] Daniele Romanini, Irène Ventrillard, Guillaume Méjean, Jérôme Morville, and Erik Kerstel. Introduction to Cavity Enhanced Absorption Spectroscopy. In Gianluca Gagliardi and Hans-Peter Loock, editors, *Cavity-Enhanced Spectroscopy and Sensing*, Springer Series in Optical Sciences, pages 1–60. Springer, Berlin, Heidelberg, 2014.

[123] Fabry-Perot Interferometer Tutorial. https://www.thorlabs.com.

[124] Xiaomei Shi and Zhanghua Han. Enhanced terahertz fingerprint detection with ultrahigh sensitivity using the cavity defect modes. *Sci Rep*, 7(1):13147, October 2017.

[125] Ran Damari, Omri Weinberg, Daniel Krotkov, Natalia Demina, Katherine Akulov, Adina Golombek, Tal Schwartz, and Sharly Fleischer. Strong coupling of collective intermolecular vibrations in organic materials at terahertz frequencies. *Nat Commun*, 10(1):3248, July 2019.

[126] I. Carusotto and G. C. La Rocca. Two-photon Rabi splitting and optical Stark effect in semiconductor microcavities. *Phys. Rev. B*, 60(7):4907–4919, August 1999.

[127] Vinzenz Stummer, Tobias Flöry, Matthias Schneller, Edgar Kaksis, Markus Zeiler, Audrius Pugžlys, and Andrius Baltuška. Spectral Peak Recovery in Parametrically Amplified THz-Repetition-Rate Bursts, May 2023.

[128] G. Andriukaitis. *Development and Applications of a Kilohertz High Energy Femtosecond Yb:CaF2 Laser Amplifier*. Doctoral Thesis, Technische Universität Wien, 2012.

[129] Douglas B. Leviton, Bradley J. Frey, and Timothy J. Madison. Temperature-dependent refractive index of CaF 2 and Infrasil 301. In James B. Heaney and Lawrence G. Burriesci, editors, *Optical Engineering + Applications*, page 669204, San Diego, CA, September 2007.

[130] E. Treacy. Optical pulse compression with diffraction gratings. *IEEE Journal of Quantum Electronics*, 5(9):454–458, September 1969.

[131] Ignas Astrauskas, Edgar Kaksis, Tobias Flöry, Giedrius Andriukaitis, Audrius Pugžlys, Andrius Baltuška, John Ruppe, Siyun Chen, Almantas Galvanauskas, and Tadas Balčiūnas. High-energy pulse stacking via regenerative pulse-burst amplification. *Optics Letters*, 42(11):2201–2204, 2017.

[132] Shian Zhou, Frank W. Wise, and Dimitre G. Ouzounov. Divided-pulse amplification of ultrashort pulses. *Opt. Lett., OL*, 32(7):871–873, April 2007.

[133] Marco Kienel, Arno Klenke, Tino Eidam, Martin Baumgartl, Cesar Jauregui, Jens Limpert, and Andreas Tünnermann. Analysis of passively combined divided-pulse amplification as an energy-scaling concept. *Optics Express*, 21(23):29031–29031, 2013.

[134] Yoann Zaouter, Florent Guichard, Louis Daniault, Marc Hanna, Franck Morin, Clemens Hönninger, Eric Mottay, Frédéric Druon, and Patrick Georges. Femtosecond fiber chirped- and divided-pulse amplification system. *Optics Letters*, 38(2):106–108, 2013.

[135] Richard Byrd, Peihuang Lu, Jorge Nocedal, and Ciyou Zhu. A Limited Memory Algorithm for Bound Constrained Optimization. *Journal of Scientific Computing*, 16(5):1190–1208, 1995.

[136] Rick Trebino. *Frequency-Resolved Optical Gating: The Measurement of Ultrashort Laser Pulses*. Springer US, Boston, MA, 2000.

[137] T.A.C.M. Claasen and W.F.G. Mecklenbräucker. The Wigner distribution - a tool for time-frequency signal analysis, Part I: Continuous signals. *Philips Journal of Research*, 35(4/5):276–300, 1980.

[138] Justin Ratner, Günter Steinmeyer, Tsz Chun Wong, Randy Bartels, and Rick Trebino. Coherent artifact in modern pulse measurements. *Opt. Lett., OL*, 37(14):2874–2876, July 2012.

[139] M. G. Raymer, M. Beck, and D. McAlister. Complex wave-field reconstruction using phase-space tomography. *Phys. Rev. Lett.*, 72(8):1137–1140, February 1994.

[140] Jonas Morgenweg, Itan Barmes, and Kjeld S. E. Eikema. Ramsey-comb spectroscopy with intense ultrashort laser pulses. *Nature Phys*, 10(1):30–33, January 2014.

[141] Jens Bredenbeck, Jan Helbing, Arne Sieg, Tobias Schrader, Wolfgang Zinth, Christian Renner, Raymond Behrendt, Luis Moroder, Josef Wachtveitl, and Peter Hamm. Picosecond conformational transition and equilibration of a cyclic peptide. *Proceedings of the National Academy of Sciences*, 100(11):6452–6457, May 2003.

[142] Zhi Guo, Yan Wan, Mengjin Yang, Jordan Snaider, Kai Zhu, and Libai Huang. Long-range hot-carrier transport in hybrid perovskites visualized by ultrafast microscopy. *Science*, 356(6333):59–62, April 2017.

[143] K. J. Weingarten, M. J. W. Rodwell, H. K. Heinrich, B. H. Kolner, and D. M. Bloom. Direct electro-optic sampling of GaAs integrated circuits. *Electronics Letters*, 21(17):765–766, August 1985.

[144] Paul A. Elzinga, Ronald J. Kneisler, Fred E. Lytle, Yanan Jiang, Galen B. King, and Normand M. Laurendeau. Pump/probe method for fast analysis of visible spectral signatures utilizing asynchronous optical sampling. *Appl. Opt., AO*, 26(19):4303–4309, October 1987.

[145] Jens Bredenbeck, Jan Helbing, and Peter Hamm. Continuous scanning from picoseconds to microseconds in time resolved linear and nonlinear spectroscopy. *Review of Scientific Instruments*, 75(11):4462–4466, November 2004.

[146] Laura Antonucci, Xavier Solinas, Adeline Bonvalet, and Manuel Joffre. Asynchronous optical sampling with arbitrary detuning between laser repetition rates. *Optics Express*, 20(16):17928–17928, 2012.

[147] Laura Antonucci, Xavier Solinas, Adeline Bonvalet, and Manuel Joffre. Electronic measurement of femtosecond time delays for arbitrary-detuning asynchronous optical sampling. *Optics Express*, 28(12):18251–18251, 2020.

[148] Laura Antonucci, Adeline Bonvalet, Xavier Solinas, Louis Daniault, and Manuel Joffre. Arbitrary-detuning asynchronous optical sampling with amplified laser systems. *Opt. Express, OE*, 23(21):27931–27940, October 2015.

[149] Justinas Pupeikis, Benjamin Willenberg, Francois Bruno, Mike Hettich, Alexander Nussbaum-Lapping, Matthias Golling, Carolin P. Bauer, Sandro L. Camenzind, Abdelmjid Benayad, Patrice Camy, Bertrand Audoin, Christopher R. Phillips, and Ursula Keller. Picosecond ultrasonics with a free-running dual-comb laser. *Opt. Express, OE*, 29(22):35735–35754, October 2021.

[150] Michael B. Price, Justinas Butkus, Tom C. Jellicoe, Aditya Sadhanala, Anouk Briane, Jonathan E. Halpert, Katharina Broch, Justin M. Hodgkiss, Richard H. Friend, and Felix Deschler. Hot-carrier cooling and photoinduced refractive index changes in organic–inorganic lead halide perovskites. *Nat Commun*, 6(1):8420, September 2015.

[151] Tufan Ghosh, Sigalit Aharon, Lioz Etgar, and Sanford Ruhman. Free Carrier Emergence and Onset of Electron–Phonon Coupling in Methylammonium Lead Halide Perovskite Films. *J. Am. Chem. Soc.*, 139(50):18262–18270, December 2017.

[152] Laura M. Herz. Charge-Carrier Dynamics in Organic-Inorganic Metal Halide Perovskites. *Annual Review of Physical Chemistry*, 67(1):65–89, 2016.

[153] Luis M. Pazos-Outón, T. Patrick Xiao, and Eli Yablonovitch. Fundamental Efficiency Limit of Lead Iodide Perovskite Solar Cells. *J. Phys. Chem. Lett.*, 9(7):1703–1711, April 2018.